Synthesis and Optoelectronic Properties of Two-dimensional Transition Metal Dichalcogenides

by Ismail Bilgin

B.Sc. in Physics Education, Black Sea Technical University
M.Sc. in Physics and Astronomy, Clemson University

A dissertation submitted to

The Faculty of
the College of Science of
Northeastern University
in partial fulfillment of the requirements
for the degree of Doctor of Philosophy

May 4, 2017

Dissertation directed by

Swastik Kar
Associate Professor of Physics

Acknowledgements

First and foremost, I would like to express my sincere gratitude to my advisor Prof. Swastik Kar for the continuous support on my Ph.D. study and research, and for his patience, kindness and immense knowledge. I appreciate all the effort he put into supporting me and into expanding my research with his valuable collaborations, and he also helped me to realize how to become a great scientist.

Some part of my thesis research conducted at Los Alamos National Laboratory (LANL) under the supervision of Prof. Aditya Mohite. I am grateful to him for providing me with an excellent and invaluable atmosphere while doing my research at LANL. He was very kind and caring supporter during my PhD.

I would like to thank our scientific collaborators for their contribution to my work: Humberto Terrones, Mauricio Terrones, Jinkyoung Yoo, Meni Wanunu, Saikat Talapatra, Keshav M. Dani, Moneesh Upmanyu, Andres de Luna Bugallo, Kazu Fujisawa, Aldo S. Raeliarijaona, Michael K. L. Man, Andrew Winchester, Yung-Chen Lin and Pradeep Waduge.

My sincere thanks also goes to my other committee members Prof. Arun Bansil and Prof. Donald Heiman for serving on my dissertation committee.

My sincere thanks also goes to members in Prof. Aditya Mohite Group at LANL: Dr. Gautam Gupta, Dr. Arun T. Mallajosyula, Dr. Hisato Yamaguchi, Dr. Wanyi Nie, Dr. Jean-Christophe Blancon, Dr. Akhilesh Signh, Rajesh Kappera, Kasun Fernando, and Kunttal Keyshar. Additionally, I would like to thank the administrative staff in MPA-11 at LANL for their support and dedication: Jeffrey O. Willis, Julie Garcia, Gerie Purdy.

I also would like to thank staff scientists at the Center of Integrated Nanotechnologies (CINT) in LANL for providing training on various tools: Jon “Kevin” Baldwin, Darrick Williams, and Peter Goodwin.

I would like to thank our group members at NEU: Fangze Liu, Anthony Vargas, Daniel, Rubin, Zachariah Hennighausen, Ji Hao, Sebastian Cooper Hodge, and Colin Casey.

My special thank goes to George J. Kostas Nano scale technology and manufacturing research center at Northeastern University. I would like to express my gratitude to the friendly staff members Sivasubramanian Somu, Scott McNamara, David McKee, Adnan Korkmaz, and Hobin Jeong

I would like to thank Wentao Liang from NEU and Jules Gardener from the Center for Nanoscale System at Harvard University for their TEM training.

I would like to express my great thanks to Turkish Ministry of Education for giving me this great opportunity with an award of a scholarship to continue my PHD career in Science in the United States.

Last but not the least, I would like to thank my family.

Abstract of Dissertation

Graphene, the first 2D layered material, has had an enormous impact on the field of nanomaterials. It has been demonstrated that graphene has remarkable mechanical, electronic and optical properties such as high electrical conductivity, broad band absorption of light etc. However, graphene does not fulfill all the scientific requirements. Due to its zero-band gap, there are limited applications in optoelectronics. To overcome graphene's shortcoming, researchers have recently started to explore other 2-dimensional materials such as metal oxides, transition metal dichalcogenides, and hexagonal boron nitrides.

Among the 2D materials, transition metal dichalcogenides (such as MoS_2, $MoSe_2$, WS_2, WSe_2) get more attention due to their tunable optical band gaps. It has been shown that these TMDs go from indirect to direct band gap as the layer count goes from bulk to monolayer, which is one of the requirements of optoelectronic device applications.

Since these materials are layered, it can be mechanically exfoliated easily. However, large area and highly crystalline structures are required to observe optical and electronic properties, as well as to make these viable for commercial applications. In my research, I have developed a new synthesis method, called vapor phase chalcogenization, by using MoO_2 or WO_2 as a precursor unlike conventionally use Mo, W and MoO_3, WO_3 powders. With this method, we eliminated the chemical reaction process to one step with less oxygen content in the reaction. The quality of the grown samples is clearly observed by Raman, Photoluminescence, and Photocurrent Spectroscopy., and further analyzed by Transmission Electron Microscopy (TEM). For example, we have reported, for the first time, two distinctly new phonon processes in 2D MoS_2 at 285 cm^{-1} and 487 cm^{-1}. The ultra-high, optoelectronic-grade crystalline

quality of MoS_2 sample could be also observed through photocurrent spectroscopy, which clearly reveal excitonic states at room temperature. I further studied temperature dependent binding energies of excitons and quasiparticle band gap of MoS_2.

In my second work, I have extended my research to another 2D material, molybdenum diselinide ($MoSe_2$), which is more favorable for solar cell applications due to its optical band gap range. We have observed detailed Raman processes of mono and few layer of $MoSe_2$. which some of them are previously not explained experimentally and theoretically. I further studied excitation energy dependence of the $MoSe_2$ Raman spectrum.

Finally, creating artificially-stacked and in-plane 2D heterostructures has also opened a new research field for designing new materials. Building these materials also requires clean interfaces, and creating atomically-controlled van der waals (vdW) heterostructure is still challenging. We have synthesized rotationally aligned vertical MoS_2-$MoSe_2$ heterostrucutres to investigates the unexplored physical properties of these materials.

Table of Contents

Acknowledgements ii

Abstract of Dissertation iv

Table of Contents vi

List of Figures x

List of Tables xix

Chapter 1: Introduction and Background 1

1.1 Atomically-Thin Transition Metal Dichalcogenides: Two Dimensional Crystals beyond Graphene 1

1.2 Optical and Electronic Properties of 2D Materials 6

1.3 Applications of Atomically Thin TMD materials 9

1.4 Heterostructures of 2D Materials 11

1.5 Thesis Outline and Published Work 13

Chapter 2: Experimental Methods 15

2.1 Vapor Phase Chalcogenization: A New Approach for Synthesis of High-Quality Transition Metal Dichalcogenides 15

2.1.1 Conventional CVD Approaches and Their Limitations: 15

2.1.2 Development of Vapor Phase Chalcogenization 17

2.1.3 Sample of Optical and Electron Microscope Images 20

2.2 Analysis of 2D materials using Transmission Electron Microscope (TEM) – based selected area diffraction patterns (SAED) 21

2.3 Atomic Force Microscopy 24

2.4 Raman and Photoluminescence Spectroscopy 26

2.5 Photoabsorption Spectroscopy 31

2.6 Fabrication of Field Effect Transistor Devices 36

2.6.1 Photolithography 36

2.6.2 Electron Beam Lithography 36

Chapter 3: Investigation of Optoelectronic Properties of MoS_2 39

3.1 Introduction 39

3.2 Results and Discussions 42

3.3 Conclusions 58

3.4 Supporting information 59

Chapter 4: Investigation of Raman Processes in High-Quality Vapor Phase Chalcogenization Grown Atomically Thin Molybdenum Diselenide 61

4.1 Introduction 61

4.2 Results and Discussion 65

4.3 Conclusions 80

Chapter 5: Heterostructures of 2D Materials-Synthesis and Properties 81

5.1 Semiconductor Heterostructures 81

5.2 Heterostructures in 2D materials 82

5.3 Heterostructures Atomically-Thin MoS_2 and $MoSe_2$ 84

5.4 Raman Spectroscopy of Vertically -Stacked Heterostructures. 91

5.5 Raman Spectroscopy of in-Plane Heterostructures 93

5.6 Photoluminescence of MoS_2-$MoSe_2$ Heterostructures 98

Chapter 6: Conclusion and Discussion 100

Dissemination 101

Journal Publications 101

PATENT 102

REFERENCES 103

List of Figures

Figure 1.1: (a) Electromagnetic spectrum for various 2D materials. Electronic band structure of monolayer hBN (b), MoS_2 (c), BP (d), and graphene (e). (Reproduced from Ref.[27]) 4

Figure 1.2: (a) Crystal structure of monolayer TMD in top view and unit cell. (b) Schematic of bulk and even-layers structure and bulk unit cell. Schematic model of two distinct symmetries of monolayer MoS_2 with 2H (trigonal prismatic) (c) and 1T (octahedral).(a-b from Ref.[34] ; c-d Ref.[33])..... 6

Figure 1.3: Electronic properties of atomically thin layered TMDs. Band structure of bulk (a) and monolayer MoS_2 (b). (c) Photoluminescence spectra of MoS_2 with various thicknesses. (a-b images adapted from Ref.[36] ; c from Ref. [39]) 7

Figure 1.4: Photocurrent spectra for suspended monolayer MoS_2 showing position of excitonic A-, B-, and C- peaks and band gap E_g (reproduced from Ref.[41]). b) Schematic diagram of optical transition at the K- point in monolayer TMDs (reproduced from Ref.[42]). 8

Figure 1.5: a) 2D hexagonal lattice of monolayer TMDs. Valley dependent optical selection rules in monolayers. (Image a is reproduced from Ref.[50,51]; image b is reproduced from Ref.[50])..... 9

Figure 1.6: Applications of TMDs on diverse fields. a) Schematic illustration and optical micrograph of a five-stage ring oscillator based on bilayer MoS_2. b) A photograph of MoS_2 transistors, integrated logic inventer and RF amplifier on flexible substrate. c) Excellent sunlight absorption in two-dimensional TMD monolayers. d) Schematic diagram of MoS_2-based FET biosensor. (Figure reproduced from: a, ref.[52]; b, ref.[54]; c, ref.[55]; d, ref.[58]) 11

Figure 1.7 Building artificial heterostrucutres with LEGO blocks.(Ref[9]) 13

Figure 2.1: Schematic of the vapor phase deposition (PVD) system for growing highly crystalline single layer TMDs and their heterostructures. 18

Figure 2.2: Top row represents SEM images of mono and few layer structures of MoS_2. Middle row: Typical optical images of various monolayer TMDs grown by vapor phase deposition. Bottom row: SEM and Optical images of MoS_2-$MoSe_2$ and MoS_2-$MoSe_2$-MoS_2 heterostructures..... 20

Figure 2.3: (a) Isolated single crystal monolayer samples. (b) With increasing growth duration, the crystals merge to form discontinuous polycrystalline samples. (c) and (d) Further increase of growth results in certain areas of the substrates being continuously covered with polycrystalline samples (bottom halves) while other parts (top halves) yet to complete the full-surface coverage. 21

Figure 2.4: a) Schematic diagram of transmission electron microscopy (TEM)(image from Ref.[89] b) two dimensional hexagonal coordinates in real space. Adapted from Ref.[90] c) typical optical images of transferred heterostructure sample to copper TEM grid. d) mono and bilayer $MoSe_2$ sample suspended over 2 micron holes. e) Electron diffraction pattern from selected monolayer $MoSe_2$ area. The dashed hexagons represent s two set of plane rings. 23

Figure 2.5: (a) Schematic illustration of an AFM (b) A photography of AFM used in our lab. (from Nano Magnetic Instruments). A typical AFM image (c) and line profile (d). 25

Figure 2.6: Energy level diagram with various possible types of optical scattering processes seen in solids. (Reproduced from Ref.[91]) 27

Figure 2.7: The vibrational patterns of the normal modes for single layer MoS_2(a-f), and bilayer (g-l). (Image reproduced from Ref.[92]) (m) A photograph of Raman spectrometer used in our lab (Renishaw Ramascope)..... 29

Figure 2.8: a) The major Raman peaks for VPC-grown monolayer WS_2, MoS_2, and $MoSe_2$. b) Monolayer PL spectra for various TMDs grown with our method..... 30

Figure 2.9: (a) Optical image of monolayer WS_2 (scale bar is 10 microns). Raman mapping of the E^1_{2g} (352 cm^{-1}) and A_{1g} (414 cm^{-1}) modes. (excitation wavelength 532 nm)..... 31

Figure 2.10: Absorption Spectrum for monolayer MoS_2 to calculate excitonic band gap and quasiparticle band gap. (This work is unpublished-Manuscript under review)[94]..... 35

Figure 2.11: Schematic illustration of PMMA transfer method for TMDs..... 37

Figure 2.12: a) Monolayer MoS_2 transferred on SiO_2/Si substrate including large electrodes with markers. b) Magnified image of selected rectangular area in red. c) An optical image of FET device after lithography and Ti/Au deposition. 38

Figure 3.1: Typical example of monolayer MoS_2 samples grown using MoO_2 precursor, on different substrates. Colored images are optical, and B/W ones are SEM images. (b) Typical optical and SEM images of bi-layer MoS_2 samples fabricated on SiO_2. Various states of initiation and growth of the second layer have been represented by these images. The final image in (b) is an SEM image showing intricate details of the bilayer structure. (c) Optical and SEM images of a range of multi-layer samples at various stages of growth and with various shapes and morphologies. 43

Figure 3.2: (a) AFM image of a few-layered sample, with incomplete top-layer, such that the top-layer thickness can be measured using the cross-section step height, as shown on the side. (b) Raman spectra from regions of various layer-thickness from a multilayer sample (Inset: optical image), showing the evolution of the dominant E^1_{2g} and A_{1g} peaks for different layer-thicknesses. (c) Variation of the peak position separation, $\Delta = \omega[A_{1g}]-\omega[E^1_{2g}]$, as a function of layer-thickness in samples grown on SiO_2/Si and quartz substrates. The spread in data point for each layer corresponds to 4-6 data points that were collected from different samples. (d) Typical Photoluminescence (PL) spectrum obtained from a monolayer MoS_2 sample, showing the A and B excitonic peaks. (e) Optical image of a monolayer sample, which was used to perform Raman and PL mapping, as shown in (f) Raman map of $\omega[E^1_{2g}]$, (g) Raman map of $\omega[A_{1g}]$ (h) Raman map of $\omega[A_{1g}]-\omega[E^1_{2g}]$ and (i) PL map of the Excitonic A-peak. 46

Figure 3.3: (a) Typical survey scan of several first-order and multi-phonon processes identified in monolayer and few-layered 2D-MoS_2 samples synthesized on SiO_2/Si. The intensities of most of these processes are much weaker than the two dominant processes E^1_{2g} and A_{1g}, and have been labeled as shown. The two labels in red are previously unreported peaks (see text). (b) The few-layered CVD-grown sample synthesized on SiO_2/Si (same as figure 2b Inset), and (c) representative few-layered CVD-grown samples synthesized on quartz that were used to investigate the layer-thickness-dependence of the two new peaks, details of which are shown in (d)-(g). (d), (e) Absence of Raman peak at ~285 cm-1 and ~487 cm-1 in monolayer samples that appear in samples with more layers, as seen in 2D-MoS_2 grown on 300 nm of SiO_2 on silicon. (f)-(g) Averaged layer-thickness variation of the same peaks when measured on 2D-MoS_2 grown on quartz (see text). 49

Figure 3.4: (a) Schematic illustration of the single layer MoS_2 field effect transistor platform for electrical and photocurrent measurements. (b) Optical image of the FET device. (c) I_d-V_d curves measured for different gate voltages in the dark. Inset: Ti/Au is used for drain- source electrodes. (d) I_d-V_g curve measured for a bias voltage ranging from 2 V to 8 V. (Data is taken in LANL under supervision of Dr. Mohite). 52

Figure 3.5: Excitonic states in monolayer MoS_2 investigated by photocurrent spectroscopy at room temperature. (a) Excitonic states A, B, and C characterized by the corresponding peaks in the photocurrent spectrum (V_{ds}= 4 V). (b) Bias dependence of photocurrent spectra showing evolution of excitonic peaks (V_g = -42 V). Inset: First derivative of the photocurrent spectra with respect to energy, from which the continuum band gap energy of single layer MoS_2 is ≈ 2.4 eV. (c) Bias dependence of the photocurrent amplitude ratios of the A-, B-, and C- excitonic peaks at room temperature. (Data is taken in LANL under supervision of Dr. Mohite). 54

Figure 3.6: Photocurrent spectra of Single layer MoS_2 at low temperature (5 K): (a) PC spectra measured for different bias voltages at Vg=-30 V, 5 K. The inset: Band gap calculation of single layer MoS_2 at low temperature. (b) Relative photocurrent amplitudes of A-, B-, & C- peaks. (c) Binding and spin orbit coupling energies for single layer MoS_2 at different temperatures. (Data is taken in LANL under supervision of Dr. Mohite) 57

Figure 3.7: The E^1_{2g} and A_{1g} modes have both helicity and linear polarization dependence. In our Raman spectrometer, the incident laser partially linear polarized. Therefore, A_{1g} scattered light has the same polarization as the incident laser. The Raman has an optional $\lambda/2$ waveplate in front the spectrometer. We tested the Raman spectra for both with and without waveplate. The A_{1g} peak shows strong

polarization dependence compared to the E^1_{2g} peak which shows weak dependence. This polarization dependence is not related to the sample quality. 59

Figure 3.8: Transfer characteristic of the device in dark and under 510 nm light illumination at 8V bias voltage 60

Figure 4.1: Optical images of typical VPD-grown single-layer $MoSe_2$ on (a-b) Si/SiO_2 and (c) quartz substrates, highlighting various sizes and morphologies. (d) Typical SEM image of single layer $MoSe_2$ on Si/SiO_2 substrates. (e) Typical AFM topographical image (scale bar = 5 microns) of a monolayer $MoSe_2$ sample, its thickness ≈0.8 nm determined from the step-height as shown in the the height profile (inset) along the white line in AFM image. (f) Typical Photoluminescence spectrum of single-, few-layered and thick $MoSe_2$ samples. The direct-gap single-layered sample demonstrates the characteristic strong peak at 1.51 eV originating from the A-exciton, and a second shallow feature near 1.71 eV originating from the B-excitons. 66

Figure 4.2: Raman spectra of VPD-grown monolayer $MoSe_2$ at different excitation energies: 1.95 eV, 2.33 eV, 2.54 eV and 2.71 eV. The peaks were normalized with respect to the intensity of the Si Peak at 520 cm^{-1}. The various peaks were labelled in terms of the nearest vibrational modes obtained in our theory calculations and matched with previous reports (see text). The peak features are observed to appear or grow more prominent as the excitation energy changes. The most noticeable ones being around 250 cm^{-1}, which we label as the 2ZA peak as discussed in the main text, and the $A2''(\Gamma)$ peak around 350 cm^{-1}, which is expected to remain absent in monolayer samples. (b) Evolution of the peak intensity ratio of the A' and E' peaks (at ~240 cm^{-1} and ~285 cm^{-1}, respectively), which demonstrates a sharp resonance around energies close to the C-exciton of monolayer $MoSe_2$. (c) A similar resonant feature is observed in

the excitation-energy dependence of the peak intensity ratio of the 2ZA and E' peaks (at ~250 cm^{-1} and ~285 cm^{-1}, respectively). 69

Figure 4.3: Phonon dispersion of monolayer $MoSe_2$ showing the various vibrational bands as labeled. The left inset shows Schematic representation of the principle vibrational modes (b) Calculated vibrational density of states (VDOS) for monolayer $MoSe_2$. (Data provided by Prof. Humberto Terrones/manuscript under preparation) 72

Figure 4.4: (a)Electronic band structure of monolayer calculated using ab-initio density functional theory. (b) Contour plot of the energy levels of the first excited band. The contour lines correspond to a region with the same energy in the first Brillouin zone (delimited by the dashed line). The black lines correspond to electron energy level of ~2.54 eV and the black arrow represent a wave-vectors of phonon that can scatter the electron to another isoenergy. ~2.54 eV (resp. 2.33 eV) contour line. (Data provided by Prof. Humberto Terrones/manuscript under preparation) 74

Figure 4.5: (a) Magnified Raman spectra of monolayer $MoSe_2$ to showing the evolution of the 2ZA and E' peaks with different excitation energies. Insets: highlight the variation of their positions as a function of excitation energies. (b) Raman spectrum of a sample measure after six months of synthesis, where the 2ZA peak seems to weaken or disappear completely. 75

Figure 4.6: (a)Optical image of a typical $MoSe_2$ sample with multiple layers, in which layer-thickness dependent Raman (and photoluminescence, Figure 4.1f) spectra were investigated (scale bar = 10 µm). (b) Typical layer-thickness-dependendent Raman spectra of $MoSe_2$, shown here for an excitation energy of 2.71 eV. The spectra were normalized with respect to the silicon 520 cm^{-1} peak, and then shifted vertically for clarity. The relative intensity of the A' and E' peaks change with layer thickness, as does the

position of the E' peak. (c) Variation of the intensity ratio between the $A1'/A_{1g}$ and the E'/E^1_{2g} peaks as a function of layer-thickness, shown for four different excitation energy values. (d) Variation of the E'/E^1_{2g} peak position as a function of layer thickness, shown for four different excitation energy values. 77

Figure 5.1: Schematic representation of (a) Vertically stacked and (b) In-plane architectures of 2D materials. (c) Schematic representation of a vertical stack of multiple 2D materials, constituting of what is known as a "van der Waals heterostructure".(Image a-b reproduced from ref.[199]; image c reproduced from ref.[200], Image credit: Gabriel Constantinescu) 82

Figure 5.2: Synthesis of lateral hetero structure of $MoSe_2$-MoS_2. Optical (a) and SEM (b) images of CVD grown $MoSe_2/MoS_2$ heterostructure on Si/SiO_2 substrate. (Inset) schematic illustration of heterojunction between two different atomically thin materials ($MoSe_2$-MoS_2). (c) Low-resolution transmission electron microscope (TEM) image of a heterojunctions on a typical copper TEM grid with 2 microns holes. The brightness/contrast of this image has been significantly modified to enhance visibility of the crystals and the junction area. The inner triangular region is MoS_2, whereas the outer region is $MoSe_2$..... 85

Figure 5.3: Comparative TEM SAED pattern of monolayer and bilayer $MoSe_2$. 87

Figure 5.4: Comparative TEM SAED pattern of monolayer MoS_2 and $MoS_2/MoSe_2$ heterostructure regions..... 90

Figure 5.5: a) AFM image and height profile of CVD-grown $MoSe_2/MoS_2$ heterostructure. (b) Schematic representation of cross lines on afm image (red, blue and green lines). (Data is taken by Dr. Andres de Luna Bugallo)..... 91

Figure 5.6 a) Optical image of a sample which has different sample morphologies in different locations. Such samples are used to elucidate the role of Raman spectroscopy in distinguishing the presence of pure crystalline regions from heterostructure regions. b) Raman spectra on suspended MoS_2-$MoSe_2$ heterostructure including individual and stacked layers. 92

Figure 5.7: Raman characterization of $MoSe_2$-MoS_2 lateral heterostructures. (a)Waterfall Raman spectra of CVD grown $MoSe_2$- MoS_2 in plane hetero structure from the selected region shown in (b) optical image. Separation of each scan is 2 microns and spectra is taken with 532 nm laser. (c) The enlarged region in the blue dotted frame. 93

Figure 5.8: a) Optical image of in-plane MoS_2-$MoSe_2$ heterostructure. b) Single Raman spectrum taking the region of MoS_2, $MoSe_2$ and interfaces. c) Raman mapping of $MoSe_2$ peaks (A_{1g} at 236 cm^{-1} and 250 cm^{-1}) and MoS_2 A_{1g} peak at 400 cm^{-1}. 95

Figure 5.9: Raman mapping for CVD synthesized $MoSe_2$-MoS_2 heterostructures. Raman mapping is analyzed by using wiTECH software four project. Raman Frequencies(1/cm) are filtered and averaged to see peak intensities and positions on the flake. $MoSe_2$ Raman peaks are labeled with white color, and MoS_2 peaks are labeled yellow color. 97

Figure 5.10: TEM images of typical suspended MoS_2-$MoSe_2$ heterostructure (a) and mono and bi layer $MoSe_2$ on samples on TEM grids. Photoluminescence spectra of suspended individual layers and stacked MoS_2 -$MoSe_2$ layer. 99

List of Tables

Table 1.1: Various 2D materials currently available. The colors represents stability of 2D materials under ambient conditions: Blue:Stable; Green: Probably Stable; Pink: Unstable in air, and may be stable in inert atmosphere; Gray:3D compounds that can be exfoliated to monolayer. (Reproduced from Ref.[9]) 2

Chapter 1: Introduction and Background

1.1 Atomically-Thin Transition Metal Dichalcogenides: Two Dimensional Crystals beyond Graphene

In the early 20th century, it was widely believed that strictly 2D crystals will be thermodynamically unstable and hence cannot exist.[1,2] As a result, even though the electronic properties of monolayer graphite (graphene) was theoretically predicted in 1946,[3] there was little or no experimental progress in this field for almost another six decades. All of this changed in the most historically remarkable manner by the experimental demonstration of single- and few-layered graphene in 2004 using a micro-mechanical exfoliation technique.[4] This work and the subsequent demonstration of atomically-thin crystals[5] of other layered materials such as $NbSe_2$, $Bi_2Sr_2CaCu_2O_x$ and MoS_2 have opened up the new and exciting field of two-dimensional materials. Graphene, a single layer of carbon atoms, has been extensively studied in last decade. Confined in a 2D plane, graphene demonstrates extraordinary electronic and optical properties such as high electrical conductivity[4], unconventional quantum hall effect[6], minimum conductivity at the dirac point[7], and broadband absorption of 2.3 % visible light[8]. The exciting advancement in graphene has led to tremendous interest in other layered materials, especially in the few- to single layer limit, including hexagonal boron nitride(h-BN), transition metal dichalcogenides(TMDs), and 2D oxides.[9] To appreciate how quickly this field is progressing – a review article published in 2013 – less than a decade after the first isolation of monolayer graphene - listed approximately 40 different layered materials which could be extracted or synthesized in 2D forms.[9] This list keeps growing continuously. Depending on chemical constituents, crystal structure, and a range of electronic interactions, these 2D layered materials appear to have unique insulating, semiconducting or metallic properties. Table 1.1 outlines some of the recently reported 2D materials with various

categories of electronic properties. For example, monolayer hBN (an insulator with band gap E_g=5.9 eV) is a promising dielectric material for electronic applications.[10-12] TMDs field effect transistors (FETs) exhibit n and p-type device characteristics with relatively high carrier mobility and high on/off ratio larger than 10^6 , thus TMDs FETs become potential candidates for modern electronics.[13-16] Another group of 2D materials, monolayer 2D oxides have large band gap between 3-5 eV and higher dielectric constant than SiO_2, which enable them potential use in nanoelectronics as wide band-gap dielectrics, as well as their potential use in UV optics.[17-19]

<table>
<tr><td rowspan="1">Graphene family</td><td>Graphene</td><td colspan="2">hBN
'white graphene'</td><td>BCN</td><td>Fluorographene</td><td>Graphene oxide</td></tr>
<tr><td rowspan="2">2D chalcogenides</td><td colspan="2" rowspan="2">MoS_2, WS_2, $MoSe_2$, WSe_2</td><td colspan="2" rowspan="2">Semiconducting dichalcogenides:
$MoTe_2$, WTe_2,
ZrS_2, $ZrSe_2$ and so on</td><td colspan="2">Metallic dichalcogenides:
$NbSe_2$, NbS_2, TaS_2, TiS_2, $NiSe_2$ and so on</td></tr>
<tr><td colspan="2">Layered semiconductors:
GaSe, GaTe, InSe, Bi_2Se_3 and so on</td></tr>
<tr><td rowspan="2">2D oxides</td><td>Micas, BSCCO</td><td colspan="2">MoO_3, WO_3</td><td colspan="2" rowspan="2">Perovskite-type:
$LaNb_2O_7$, $(Ca,Sr)_2Nb_3O_{10}$,
$Bi_4Ti_3O_{12}$, $Ca_2Ta_2TiO_{10}$ and so on</td><td>Hydroxides:
$Ni(OH)_2$, $Eu(OH)_2$ and so on</td></tr>
<tr><td>Layered Cu oxides</td><td>TiO_2, MnO_2, V_2O_5,
TaO_3, RuO_2 and so on</td><td>Others</td></tr>
</table>

Table 1.1: Various 2D materials currently available. The colors represents stability of 2D materials under ambient conditions: Blue:Stable; Green: Probably Stable; Pink: Unstable in air, and may be stable in inert atmosphere; Gray:3D compounds that can be exfoliated to monolayer. (Reproduced from Ref.[9])

Besides the above mentioned electronic properties, these 2D materials can cover a broad range of optical properties as shown in Figure 1.1a. Such a wide range of band gap allows observation of new types of optics and optoelectronics involving excitons, phonons, and other complex condensed matter phenomena.[20] The variety and versatility of these 2D materials are made even more attractive by the fact that their electronic properties are often layer-thickness-dependent. For example, TMDs are

indirect band-gap materials that emergently increase their band gap values in the optically visible region to near infrared (IR) range of energies. In addition, at the monolayer limit TMDs become direct band-gap materials, making them immensely attractive for diverse optoelectronic applications, such as photovoltaics, photodetection, light-emitting systems, and junction devices. Another exciting material system is Black phosphorus (BP), which is a direct band gap material in its bulk layer, and its band gap can be tuned from 0.3 to 2 eV by reducing the number of layers Black phosphorus (BP) is a direct band gap material in its bulk layer, and its band gap can be tuned from 0.3 to 2 eV by reducing the number of layers. As seen in Figure 1.1a, the band gap energy of BP bridges between zero band gap graphene and TMDs.[21] As discussed later, some of these systems often have surprisingly high exciton binding energy values (of the order of ~500 millielectronvolts), and these are coupled to strong spin-orbit splitting effects, that provide a rich platform for examining photophysics.[22-26]

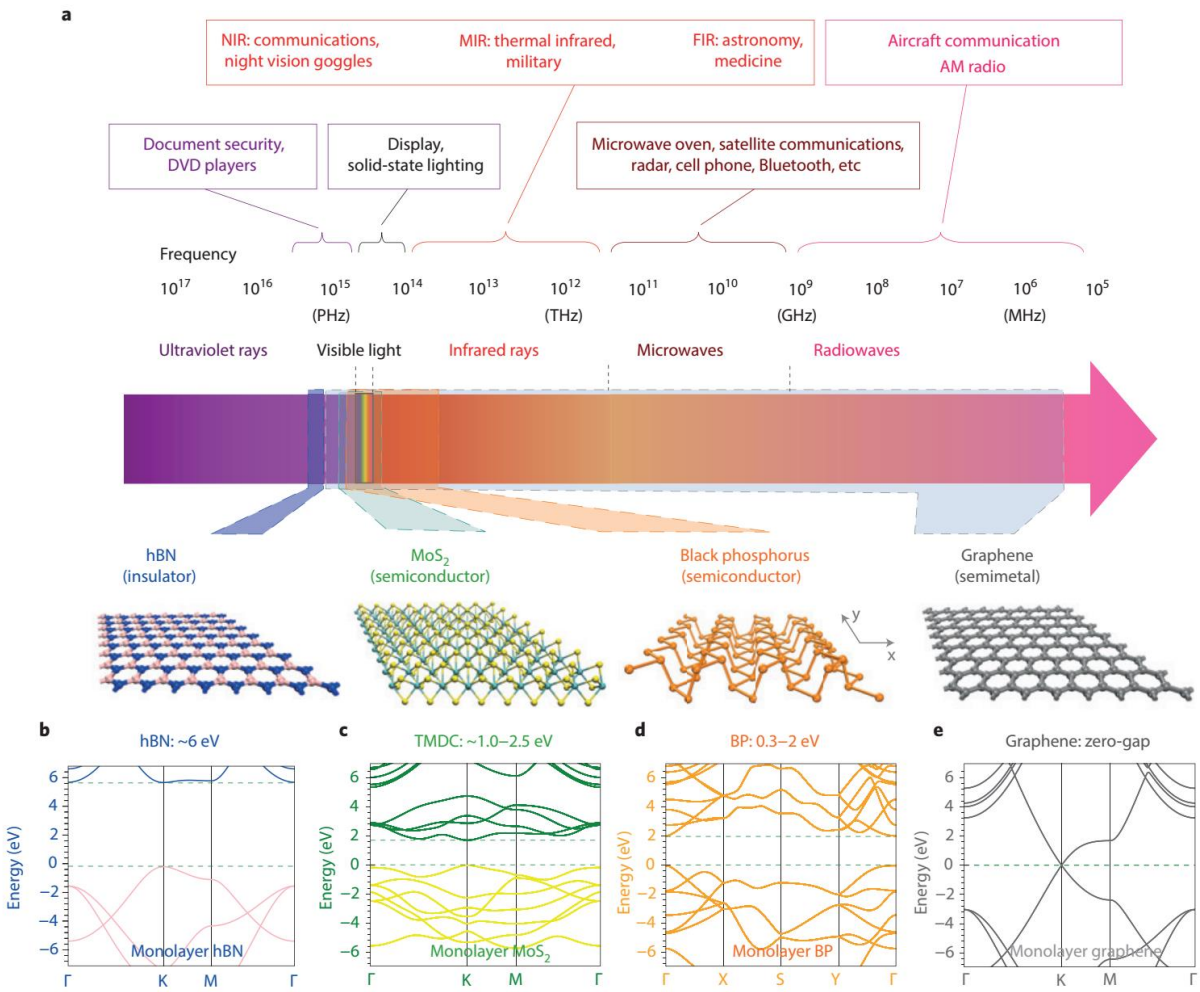

Figure 1.1: (a) Electromagnetic spectrum for various 2D materials. Electronic band structure of monolayer hBN (b), MoS_2 (c), BP (d), and graphene (e). (Reproduced from Ref.[27])

Among the various layered materials, transition metal dichalcogenides or TMDs (for example MoS2, $MoSe_2$, WS_2, WSe_2) have gained attention due to their tunable band gap and optical properties. TMDs are composed of MX2 (where M is a transition metal, M:Mo, W; and X is a chalcogenide material X:S, Se, or Te) sheets stacked on the top of one another. Within each monolayer, there are three layers of atoms, arranged as X-M-X (and hence, to distinguish from single-atom-thick 2D materials such as

graphene, a single X-M-X sheet of TMDs is often referred to as being trilayered (TL)). Atoms within the TL are covalently bonded, while stacked TLs are formed by weak van der Waals (vdW) forces. Additionally, 2H-Bulk MoS2 belongs to the D^4_{6h} space group, whereas 2H-monolayer belongs to the D^1_{3h} space group. The inversion symmetry is broken when bulk layer thinned down to monolayer since the unit cell of monolayer becomes half of the second layer of unit cell as shown in Figure 1.2a-b. Further, the difference in stacking order with in a single TL gives rise to different polytypes or polymorphs such as 2H, 1T (Figure 1.2c-d). In the case of MoS_2, depending on the arrangement of S and Mo atoms, 2H-MoS_2 is semiconducting and 1T phase is metallic. 2H-MoS_2 phase is thermodynamically more stable and and can be convert to 1T phase by alkali metal (Li, K , Na etc.) intercalations[28-32] and electron-beam irradiation[33]. It is not difficult to see that a single material system which can give rise to such a rich range of structural, electronic, and optical properties, will be attractive for new research directions. When this diversity is extended to other materials, it reflects the huge potential for fundamental research as well as applications developments. In order to do so, it is important to be able to synthesize high-quality samples, have access to various structural and functional characterization techniques, as well as access to powerful theory/modeling and simulation techniques that can help us understand the physics of these novel systems.

The following sections outlines some of the most important properties of TMDs, which forms a basis for our current understanding of these materials. It also summarizes some of the key application areas, which are enabled by their electronic and optical properties.

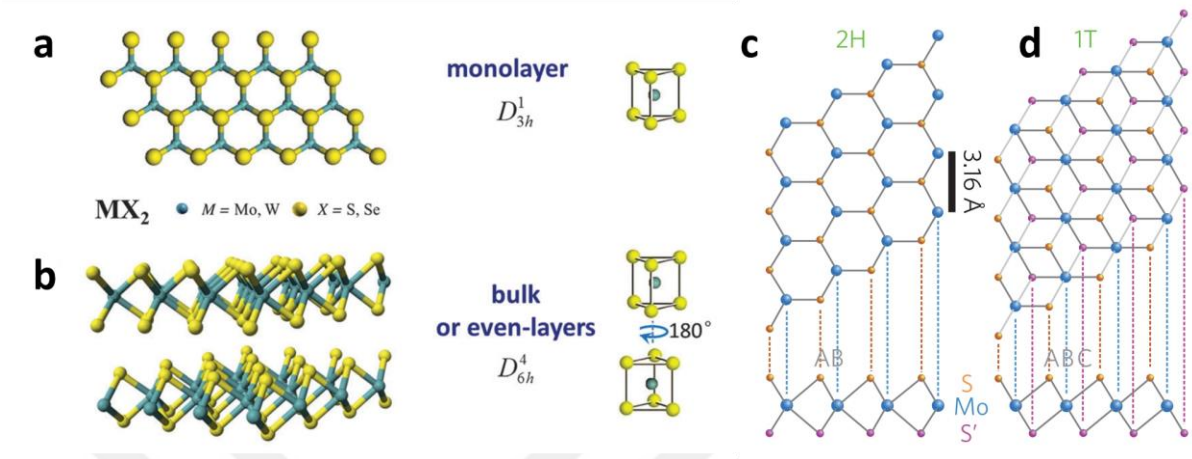

Figure 1.2: (a) Crystal structure of monolayer TMD in top view and unit cell. (b) Schematic of bulk and even-layers structure and bulk unit cell. Schematic model of two distinct symmetries of monolayer MoS_2 with 2H (trigonal prismatic) (c) and 1T (octahedral).(a-b from Ref.[34] ; c-d Ref.[33])

1.2 Optical and Electronic Properties of 2D Materials

The optical and electronic properties of 2D materials are very sensitive to layer thicknesses due to quantum confinement and inter-layer interaction effects.[35] The theoretically calculated electronic band structures (Figure 1.3a-b, adapted from ref.[36]) show that bulk MoS_2 has an indirect band gap of 1.2 eV with bottom of the conduction band and top of the valence band are located between the K and -Γ points and at the Γ point in the Brillion zone, respectively. When it becomes monolayer, both conduction and valence band extrama are located at the K point, which establishes a direct electronic transition a gap. Similarly, decreasing the number of layers on $MoSe_2$, WS_2 and WSe_2 results in indirect to direct transition.[37,38]

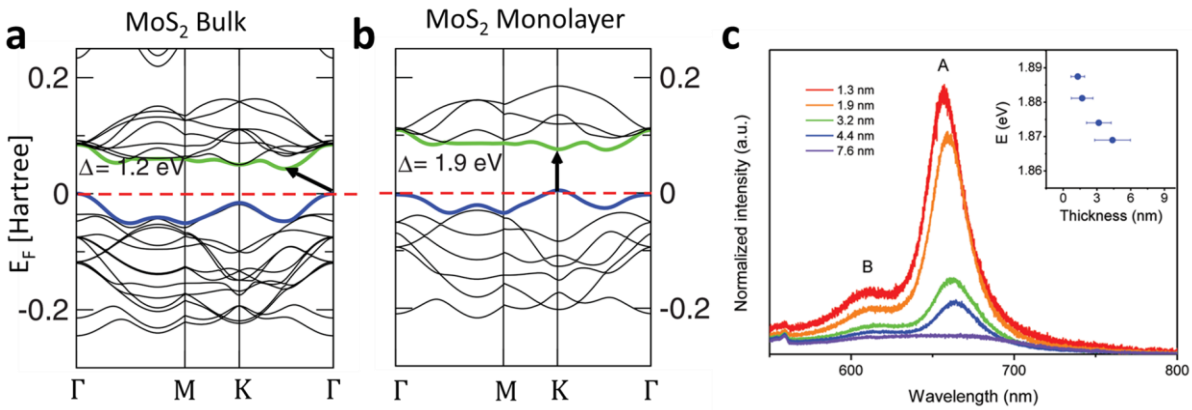

Figure 1.3: Electronic properties of atomically thin layered TMDs. Band structure of bulk (a) and monolayer MoS_2 (b). (c) Photoluminescence spectra of MoS_2 with various thicknesses. (a-b images adapted from Ref.[36] ; c from Ref. [39])

As predicted by this theory work along with other similar ones,[35,40] this single-particle gap was initially thought to be about 1.9 eV as it matched extremely well with the position of the first photoluminescence peak seen in experiments, as shown in Figure 1.3c. This peak, which appears at at 1.85 eV in monolayer MoS_2, was attributed to the A-exciton, the ground state of the first electron-hole pair to form between the highest point of the valence band and the lowest point of the conduction band, near the K points. However, various experimental works as shown in Figure 1.4a have now established beyond reasonable doubt that the binding energy of these excitons can be substantial, being of hundreds of meVs in size, and hence the electronic band gap is much larger than the ground state of the A excitons, as schematically shown in Figure 1.4b.

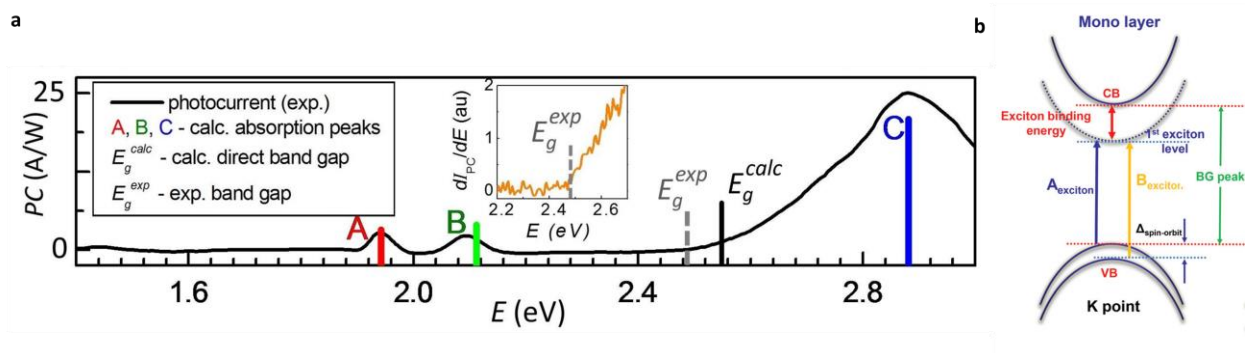

Figure 1.4: Photocurrent spectra for suspended monolayer MoS_2 showing position of excitonic A-, B-, and C- peaks and band gap E_g (reproduced from Ref.[41]). b) Schematic diagram of optical transition at the K-point in monolayer TMDs (reproduced from Ref.[42]).

This indirect to direct transition from bulk to monolayer TMDs leads to a strong absorption and more importantly, a radiative recombination of excitons, as evident from photoluminesce (PL) spectroscopy. The PL spectra of monolayer MoS_2 exhibits two exciton peaks around 670 nm (1.85 eV) and 627 nm (1.98 eV), corresponding to A and B direct exciton transition.[35,39,40] (Figure 1.3c). These direct excitonic transitions are associated with the energy split in the valance band due to strong spin orbit coupling, as mentioned before. With increasing layer thickness, MoS_2 becomes an indirect bandgap material with as seen in figure 1.3c, the intensity of PL decreases. This behavior arises from d-orbital related interaction in multi-layer in MoS_2.[35] These properties offers many attractive applications in optoelectronic devices.

Another interesting feature of atomically thin TMDs is valley degree of freedom due to broken inversion symmetry and spin orbit coupling.[43,44] In monolayers, the conduction band minimum and valence bad maximum are both located at the corners of the the hexagonal Brillion zone. The six corners belong to two inequivalent valleys denoted by +K and -K points (also described as K and K' points in some literature), as outlined in Figure 1.5a-b. Due to spin-orbit coupling, the bands at the +K points split into

spin up and spin down states, with their arrangements inverted at the –K points (*i.e.* spin down and spin up). The valley-dependent quantum states of the carriers at the K-points are treated like an additional degree of freedom beyond charge and spin, and can be probed experimentally using circularly polarized light, as shown by Mak et al.[45] and Zeng et al.[44] who demonstrated that valley polarization can be obtained with circularly polarized light. Similarly, Ye et al. experimentally demonstrated the electrical excitation and control of valley electrons.[46] Indeed, it is becoming progressively clear that in addition to the effects of doping, substrate, strain and other environmental parameters,[47-49] strong electron-electron interactions, electron-hole effects, phonons, as well as spin-orbit coupling play important roles in determining the electronic and optical properties of TMDs

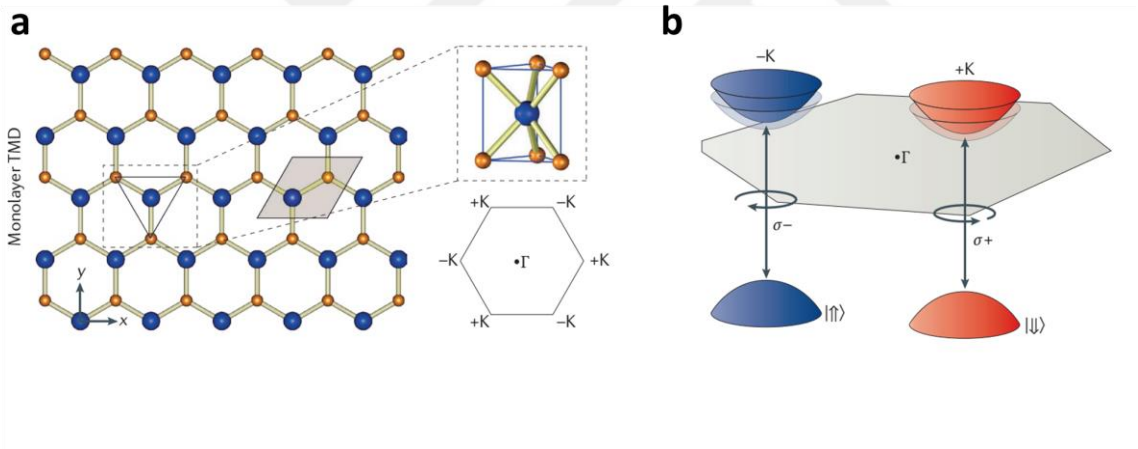

Figure 1.5: a) 2D hexagonal lattice of monolayer TMDs. Valley dependent optical selection rules in monolayers. (Image a is reproduced from Ref.[50,51]; image b is reproduced from Ref.[50])

1.3 Applications of Atomically Thin TMD materials

Owing to their favorable band gap values, one of the most important applications of TMDs is as field-effect transistors (FETs) in modern electronic devices. Graphene, a zero band gap 2D material, has been

used to make electronic devices. However, transistors made of graphene can not be switched off due to their lack of band gap. Recently, the research on FET devices has shifted to band gap material of TMDs. Radisavljevic et al[13]. demonstrated the first single layer MoS_2 transistor using hafnium oxide (HfO_2) gate dielectric with mobility up to 200 cm^2/Vs at room temperature current on/off ratio exceeding 10^8. Later, Fang et al. reported high performance p type FET transistors on single layer WSe_2 using heavily doped contacts. These initial results showed promising applications for future electronics devices. Wang et al.[52] shown integrated logic circuits based on bilayer MoS_2 including inverter , a NAND gate, a static random access memory , 5 stage ring oscillator as shown in Figure 1.6a. In addition to electrical performance, TMDs exhibit exceptional mechanical properties[53]. Bertolazzi et al. measured the breaking strength of suspended monolayer MoS_2 using atomic force microscopy (AFM). The young modulus of MoS_2 was determined $\sim$270 GPa, which is comparable to that of steel.[53] These results suggest that MoS_2 could be a potential candidate for flexible or wearable electronics. Recently, Cheng et al.[54] also showed logic inverter or radio frequency amplifier (RF) on flexible substrate as shown in Figure 1.6b. Furthermore, monolayer TMDs can absorb up to 5-10 % incident sunlight with nanometer thickness[55], which implies a remarkable potential for photovoltaic solar cells.[56,57] Other advantage of these 2D material could be biomedical applications such as biosensor, bioimaging, and drug delivery.[58-61]

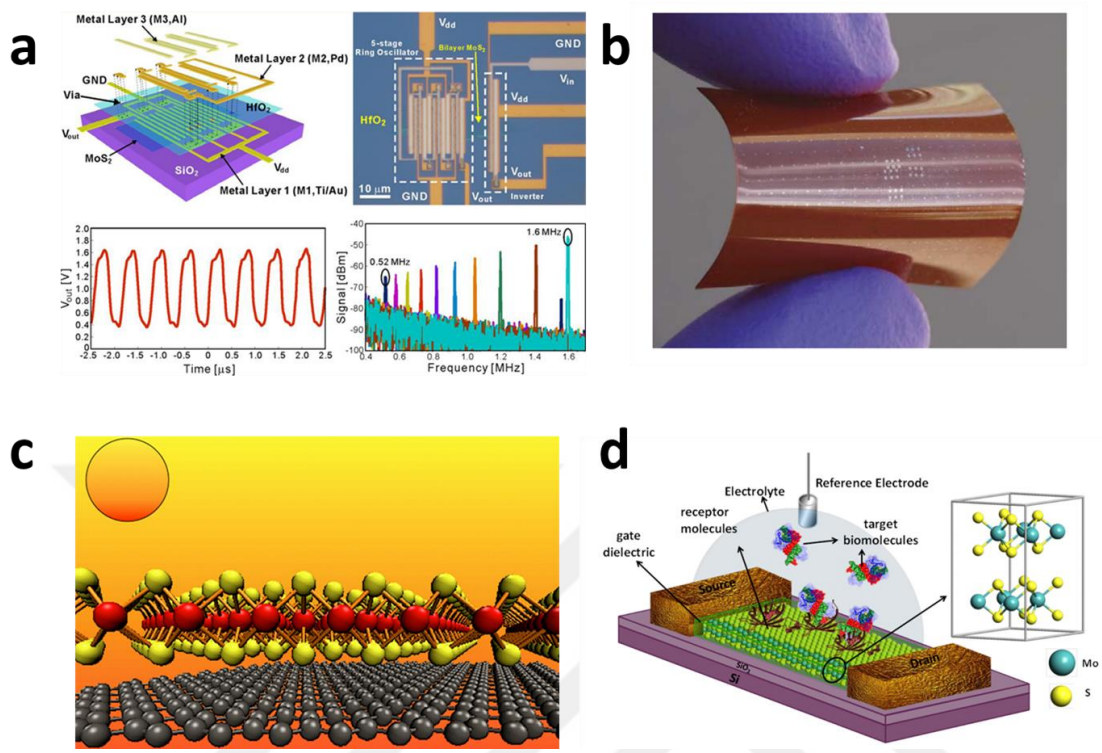

Figure 1.6: Applications of TMDs on diverse fields. a) Schematic illustration and optical micrograph of a five-stage ring oscillator based on bilayer MoS_2. b) A photograph of MoS_2 transistors, integrated logic inventer and RF amplifier on flexible substrate. c) Excellent sunlight absorption in two-dimensional TMD monolayers. d) Schematic diagram of MoS_2-based FET biosensor. (Figure reproduced from: a, ref.[52]; b, ref.[54]; c, ref.[55]; d, ref.[58])

1.4 Heterostructures of 2D Materials

Owing to their atomically-thin dimensions, the advanced functionalities from different 2D materials can be simultaneously harnessed by fabricating "club-sandwich"-like stacks of these materials,[9,62,63] resulting in the so-called van der Waals solids. In addition to this, these arrangements can also dramatically enhance device performances enabled by atomically-clean interfaces, atomically-flat substrates, and

atomically-thin electrodes. Hence, the controlled synthesis and characterization of artificially-stacked 2D solids provide attractive opportunities for impactful discoveries in 2D science and technology.

The inclusion of 2D semiconductors beyond graphene into these stacks results in a greater degree of multi-functionality, which has been utilized in a variety of logic, memory, optoelectronic, and energy devices.[63-65] A breakthrough was realized in this area of research via direct synthesis of vertically stacked layers [66] using low-cost and scalable approaches such as CVD growth, largely facilitated via a variety of rotationally aligned[67-69] and quasi-aligned[70] van der Waals epitaxial growth. A majority of work has so far focused on using hetero-layers of lattice-commensurate crystals (graphene/h-BN, MoS2/GaN, WS2/MoS2) with very small lattice mismatch. Hetero-epitaxy of the incommensurate crystal-pairs MoS2/Graphene has been shown recently,[67]though these materials largely retain their individual properties. In addition to the applications that can be potentially developed using individual 2D materials, various works have suggested that in-plane and vertically-stacked dissimilar 2D materials can harness and/or synergize the properties of the parent crystals that lead to rich new physics and applications.Integrated lateral or multilayer stack 2D materials is a new exciting field to engineer electronic and optical properties for next generation nanoelectronics. Desired artificial materials can be obtained by stacking different 2D layered materials on top of each other. This can be visualized to similar to lego blocks as seen in Figure 1.7a. For example, Graphene used as electrodes for semiconducting 2D materials (MoS_2, $MoSe_2$, WS_2, WSe_2) to improve the performance of the photodetector devices.[71,72] In addition, it has been recently demonstrated that atomically thin p-n junction between WSe_2(p doped)- MoS_2(n doped) can be created for potential applications including photodiodes, light emitting diodes and laser diodes.[73-75]

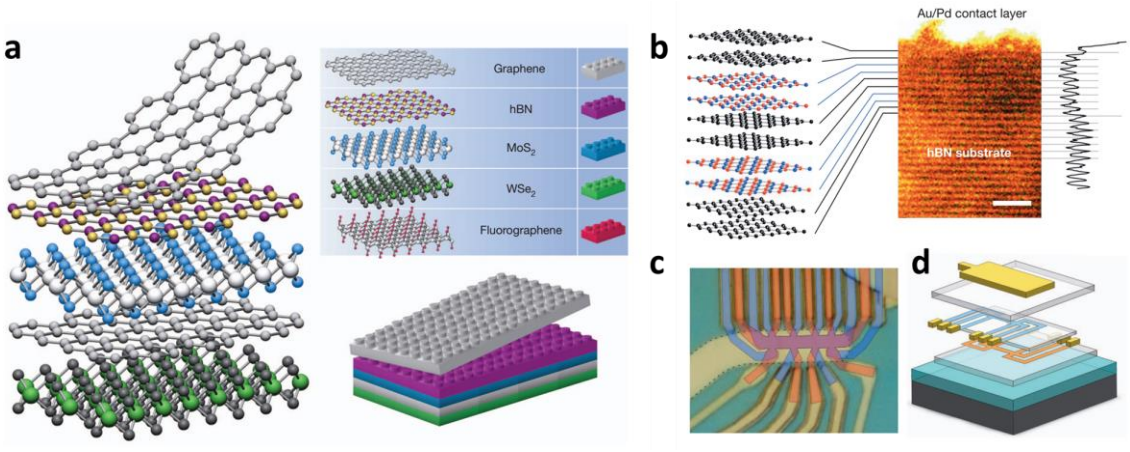

Figure 1.7 Building artificial heterostrucutres with LEGO blocks.(Ref[9])

1.5 Thesis Outline and Published Work

My thesis includes experimental results on optoelectronic properties of atomically thin layered CVD grown MoS_2, $MoSe_2$ and their vertical and lateral heterostructures. Chapter 1 covers the review of the literature related to 2-dimensional semiconducting materials. In Chapter 2, I will introduce the experimental methods used to synthesize, characterize and the process of optoelectronic device fabrications. In chapter 3, I will present my first-author published work on optoelectronic-grade crystalline quality of MoS_2 samples. We have shown that large-area highly-crystalline monolayer and few layered MoS_2 structures can be grown on variable substrate via Vapor Phase Chalcogenization method using MoO_2 as a source. This growth method enables us to observe two new layer thickness dependent Raman modes have previously never been reported. Additionally, for the first time, we have demonstrated excitonic states in monolayer of MoS_2 in photocurrent spectra at room temperature. Further, we have measured binding and spin-orbit coupling energies for single layer MoS_2. In chapter 4,

We have extended our growth method to obtained the other TMD materials. In chapter 5, I have reported detailed investigation on vertical and in-plane heterostrucutres of two dimensional MoS_2 and $MoSe_2$ grown by VPC method. In the last chapter, I will mention the future work involving exciton dissociations on MoS_2 and WS_2 FET devices.

Chapter 2: Experimental Methods

A significant portion of this research required development of methods for sample preparation, their characterizations, and setting up, measurement and analysis of the various electronic and optical experiments. In some cases, new methods were developed for performing the experiments, and in this chapter, the most important experimental aspects of this research are outlined.

2.1 Vapor Phase Chalcogenization: A New Approach for Synthesis of High-Quality Transition Metal Dichalcogenides

2.1.1 Conventional CVD Approaches and Their Limitations:

While mechanically exfoliated samples have helped elucidate the diverse potentials of 2D-MoS_2 and other TMDs, their poor yield, as well as uncontrolled and irregular sample shape, size, and morphology make them unsuitable for any practical applications. In contrast, chemical vapor deposition (CVD) has the potential for large-scale, low-cost synthesis of 2D-MoS_2 of uniform layer-thicknesses over macroscopic sizes-scales, and such samples are widely viewed as ideal for integration with current CMOS platform. For example, the CVD growth of monolayer MoS_2 has been obtained by sulfurization of Mo[76] and MoO_3[77-79] powders as a precursor. The latter recipe has become a standard for the CVD growth of monolayer MoS_2. These samples also possess field-effect mobilities between 1-10 $cm^2V^{-1}s^{-1}$. While most reports focus on electronic mobility as a parameter to quantify sample quality, the demonstration of sensitive optoelectronic processes where electron-photon and electron-phonon coupling processes are not destroyed by defects, disorder, or impurities, remains largely unexplored. The observation of rare optoelectronic processes can be thought of as a necessary and perhaps more stringent measure of the high crystalline quality of these samples, especially for optoelectronic applications.

Detailed study of the sulfurization of MoO_3 has shown that the conversion of MoO_3 to MoS_2 involves an intermediate step, during which MoO_3 is first partially reduced to MoO_2,[80,81] which then sulfurizes under appropriate conditions to produce MoS_2. Wang *et al.* have reported a method to separate these two steps whereby MoO_3 powder was first thermally evaporated, reduced using sulfur, and re-condensed to obtain MoO_2 micro-crystals, which in the second step were sulfurized layer-by-layer to obtain 2D-MoS_2 crystals.[82] Finally, a PMMA-assisted cleavage step was needed to separate MoS_2 from the underlying MoO_2 crystal and transfer onto other substrates. In this context, the question arises whether there is any need or benefit of using MoO_3 as the initial precursor, instead of MoO_2, which is a more stable oxide[81]. The relevance of this question increases when one scrutinizes the reaction pathway of MoS_2 synthesis. Li *et al.*[81] postulated that the reduction of MoO_3 follows the step:

$$MoO_3 + (x/2)\ S \rightarrow MoO_{3-x} + (x/2)\ SO_2, \qquad 2.1$$

followed by a sulfurization of MoO_{3-x}, *i.e.*

$$MoO_{3-x} + (7-x)/2\ S \rightarrow MoS_2 + (3-x)/2\ SO_2. \qquad 2.2$$

In the ideal scenario, x=1 results in intermediate compound being MoO_2, and each removed oxygen atom participates in forming SO_2. In the relatively less-ideal conditions within a CVD chamber, however, incomplete reaction may result in uncontrolled amounts of $MoS_{2-y}O_y$ phase in the atomically thin MoS_2 crystal.[83] Further, as the MoO_3 is sulfurized to produce MoS_2 crystals, these crystals provide additional binding sites for the oxygen to chemisorb on. [84] Oxygen, especially at high temperatures is also a well-known etchant for 2D materials[85,86] which suggests that at the very least, any nascent oxygen could

potentially create defects/vacancies during growth. Beyond structural and chemical effects, the presence of oxygen can also have important impacts on the electronic properties of atomically thin MoS_2. For example, adsorbed oxygen has been shown to significantly reduce sheet conductivity as well as mobility of atomically thin MoS_2.[87,88] It appears that avoiding a two-step reaction process that could at least partially decrease the possibility of incomplete reactions, as well as reduce the possible deleterious effects of oxygen may provide atomically thin MoS_2 samples with improved structural, chemical and electronic properties.

2.1.2 Development of Vapor Phase Chalcogenization

One way to overcome all of these challenges simultaneously is to use MoO_2 as a precursor instead of MoO_3, since this eliminates the need for the formation of the intermediate step shown in equation2.2, and forms the TMDs directly in vapor phase, through the following reaction:

$$MoO_2 + 3X \rightarrow MoX_2 + XO_2 \qquad 2.3$$

Using this new method, not only is it possible to reduce the oxygen content during reactions by over 30%, but also a direct synthesis of the TMD in vapor phase, that eliminates the incomplete chalcogenization, and therefore greatly improving the possibility of high quality crystalline growth of the samples. The high quality of these samples is established in chapter 3-5 through the observation optical and optoelectronic processes that are extremely difficult to observe otherwise, sometime even with samples that have been mechanically exfoliated.

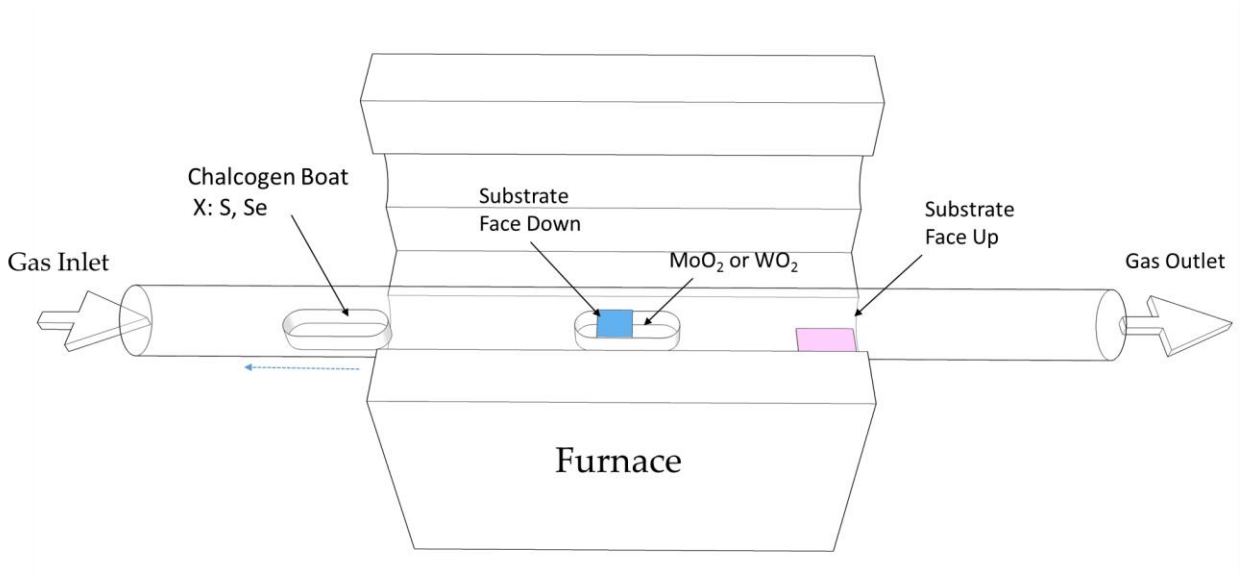

Figure 2.1: Schematic of the vapor phase deposition (PVD) system for growing highly crystalline single layer TMDs and their heterostructures.

Figure 2.1 illustrates the schematic of vapor phase deposition. Large area monolayer MoS_2 was synthesized for the first time using MoO_2 as a source by PVD method. Monolayers are synthesized low temperature at 750 °C in quartz tube 1 inch diameter by atmospheric pressure CVD. A 300 nm SiO_2/Si substrate is cleaned in acetone, isopropyl alcohol and deionized water and is placed face down alumina boat containing 10 mg MoO_2 powder (99% Sigma Aldrich) at the center of the furnace. 20 mg Sulfur powder (99.5% Alfa Aesar) is placed to upstream at the edge of the furnace. The tube is flushed 3 times with Ar carrier gas at room temperature before starting growth. The furnace temperature is first increased to 300 °C and sits there one hour with 100 sccm Argon. Then the temperature ramps up slowly to growth temperature of 750 °C at 3 °C /min with 200 sccm Argon and held there 15 minutes before cool down the room temperature. Bi –Tri layer MoS_2 structures are obtained high temperature at

950 °C. The sulfur powder is placed far from the furnace edge (2.5 inch). The furnace was heated to 650 °C at 30 °C /min with 150 sccm Ar then increased to 950 °C at 5 °C /min with 200 sccm Ar carrier gas and stay there 10 minutes. The sulfur is started to melt around 900 ℃.

In case of $MoSe_2$, with same position except sulfur replaced with selenium, the temperature ramp up to 650 C rapidly with 30 °C / min with argon flow, then the temperature is increased to 750 °C with 15 °C /min and wait 15 minutes with argon and hydrogen mixture (H_2/ Argon 2%). For WS_2 growth, since melting point is high for WO_2, Sulfur boat is located higher upstream to introduce it later time in growth. Earlier sulfurization prevents the WS_2 growth. The substrate also located at downstream of the tube for monolayer WS_2. The substrate at the top of the powder includes mostly a few and bulk layers. With these induvial growths of TMDs, heterostructure be can be obtained via two separate growth.

2.1.3 Sample of Optical and Electron Microscope Images

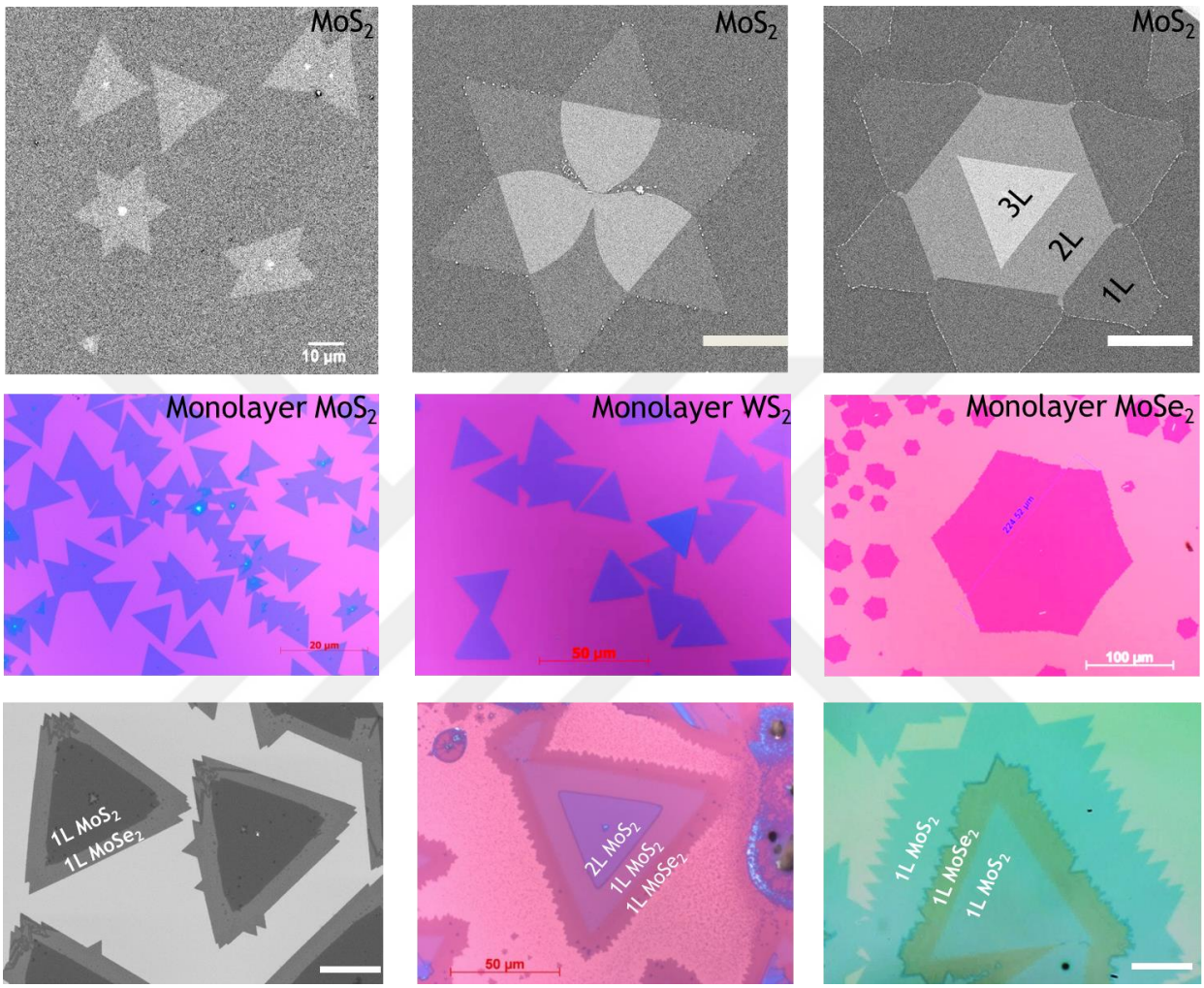

Figure 2.2: Top row represents SEM images of mono and few layer structures of MoS_2. Middle row: Typical optical images of various monolayer TMDs grown by vapor phase deposition. Bottom row: SEM and Optical images of MoS_2-$MoSe_2$ and MoS_2-$MoSe_2$-MoS_2 heterostructures.

The typical size of TMDs range from 10 – 150 microns. it is not extremely difficult to obtain large-area coverage by reducing the nucleation density (lowered flow-rate) and increasing the growth

duration. The Figure 2.3 below shows how, by controlling these parameters, polycrystalline samples of large-area coverage can be obtained.

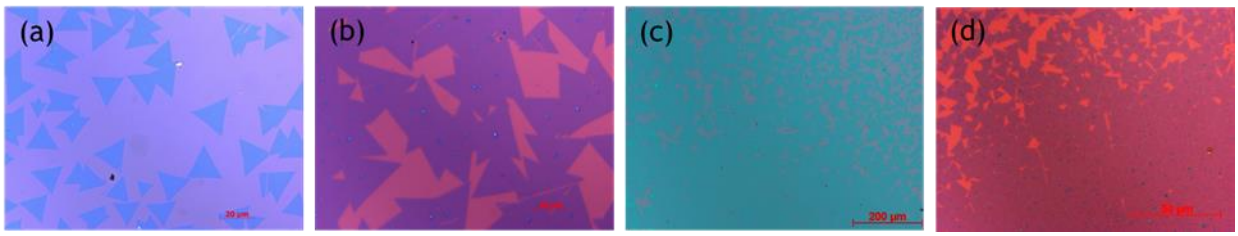

Figure 2.3: (a) Isolated single crystal monolayer samples. (b) With increasing growth duration, the crystals merge to form discontinuous polycrystalline samples. (c) and (d) Further increase of growth results in certain areas of the substrates being continuously covered with polycrystalline samples (bottom halves) while other parts (top halves) yet to complete the full-surface coverage.

2.2 Analysis of 2D materials using Transmission Electron Microscope (TEM) – based selected area diffraction patterns (SAED)

One of the most powerful methods for characterizing the type and quality of our synthesized 2D samples is by using a transmission electron microscope (TEM). The instrument used was a JEOL 2010F. Typically, a TEM operates using a beam of monochromatic and well-focused electron beam of energies ranging up to 80-200 keV. The higher energy electron beams provide better image clarity (higher resolution), but samples are also prone to get damaged due to knock-off momentum transfer from these electrons. Hence each sample was tested for different keV levels till the best possible images could be obtained. Figure 2.4a shows a typical TEM column where the sample is kept at the lower end of an electron beam acceleration and focusing hardware. Samples are usually loaded on a holey copper

grid (Figure 2.4c-d) where the exposed regions of the sample on the hole are used to analyzed the crystal image and lattice properties. The passing beam can be utilized to obtain a contrast image, as shown in Figure 2.4d which shows a region of a sample that contains both monolayer and bilayer 2D $MoSe_2$ crystals. For our research, an even more powerful tool was the selected area diffraction pattern feature of the TEM, which uses diffraction patterns obtained from the electron beam to resolve the crystal structure of our 2D materials. Figure 2.4e shows a typical diffraction pattern that reflects the reciprocal space representation of the $MoSe_2$ lattice structure. The reciprocal lattice points of $MoSe_2$ have two set of six-folds spots each representing family of planes (green and red hexagons in Figure 2.4e), which correspond to the (100) and (110) lattice planes. The scale bar is in nm^{-1}, and we first measured reciprocal lattice spacing d^* by averaging equivalent planes in the same hexagon. This measured reciprocal spacing is equal to inverse of the interplaner spacing in real space. The calculated lattice spacing is following:

$d_{(100)} = \frac{1}{d^*_{(100)}}$, $\quad d_{(100)} = 0.290\ \mathrm{nm}$ and $d_{(110)} = 0.168\ nm.$

The relationship between lattice spacing and lattice constant can be obtained using the geometry in Figure 2.4b:

$$d_{(100)} = \frac{a\sqrt{3}}{2}$$

$$d_{(110)} = \frac{a}{2}$$

The lattice constant is calculated 0.335 nm for monolayer $MoSe_2$.

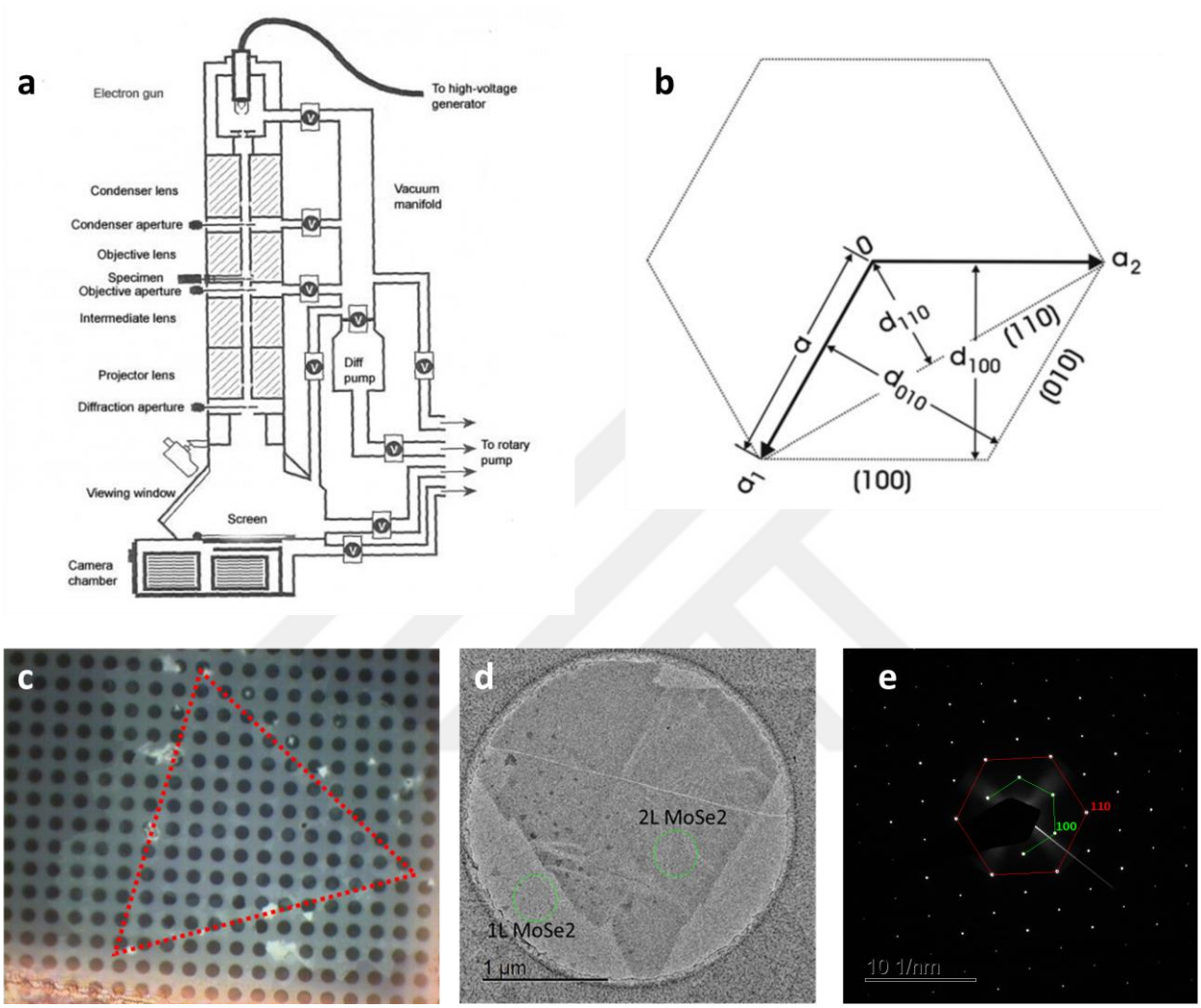

Figure 2.4: a) Schematic diagram of transmission electron microscopy (TEM)(image from Ref.[89] b) two dimensional hexagonal coordinates in real space. Adapted from Ref.[90] c) typical optical images of transferred heterostructure sample to copper TEM grid. d) mono and bilayer $MoSe_2$ sample suspended over 2 micron holes. e) Electron diffraction pattern from selected monolayer $MoSe_2$ area. The dashed hexagons represent s two set of plane rings.

2.3 Atomic Force Microscopy

Atomic Force microscopy (AFM) images nanoscale resolution on surfaces by measuring forces between a sharp probe (tip) and the sample surface. The schematic and photograph of AFM are shown in Figure 2.5a-b. The AFM in our lab includes various operational modes depending on interaction between sample and tip. We use the dynamic mode, also called tapping mode, in which the AFM tip is oscillated near its resonance frequency at very close to sample surface. The forces between the tip and sample changes the resonance frequency and oscillation amplitude while tip moves across the surface (tip is scanned over the surface). The feedback loop is used to keep RMS amplitude constant. A digital Phase locked Loop (PLL) measures the frequency shift and RMS amplitude. This provides information about the surface topography. Number of layers of in 2D materials are defined by measuring the thickness in the topography image. A representative image from AFM is shown in Figure 2.5. The thickness of $MoSe_2$ is measured around 1 nm.

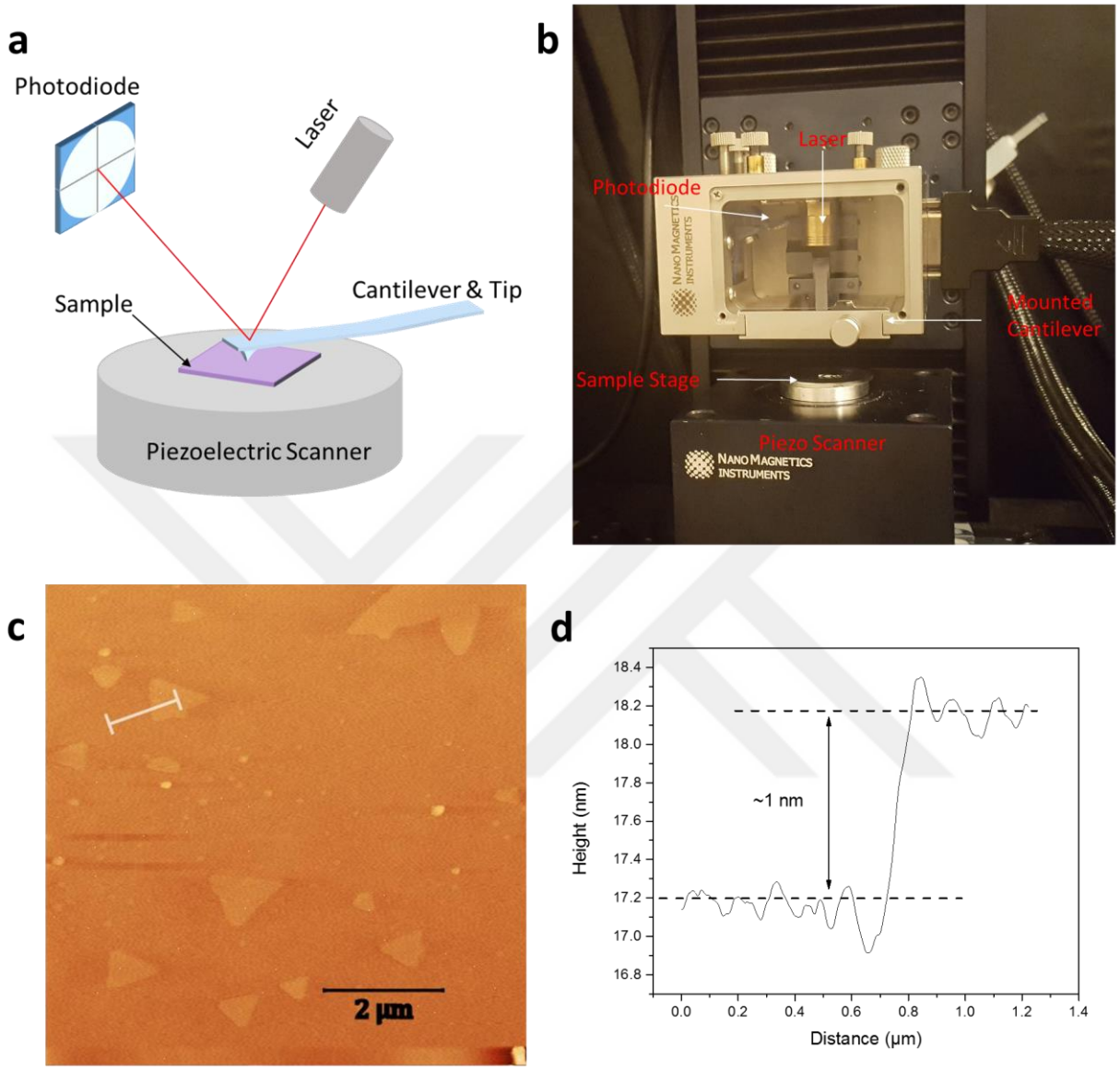

Figure 2.5: (a) Schematic illustration of an AFM (b) A photography of AFM used in our lab. (from Nano Magnetic Instruments). A typical AFM image (c) and line profile (d).

2.4 Raman and Photoluminescence Spectroscopy

Raman spectroscopy is one of the widely-used tools in the field of two dimensional nanomaterials. It can be used to characterize the defect, strain, number of layer etc. in 2D materials. Raman spectroscopy set up used in our lab is Renishaw Ramascope model shown in Figure 2.7(m). The basic working principle of Raman relies on inelastic scattering from the lattice, and involve absorption of photons by band electrons, transitions across the band due to inelastic scattering with phonons of appropriate energy and momentum values, and subsequent deexcitation mediated at band gaps, or through other phonons or defects in the crystal. In case of purely elastic scattering, the de-excited electron-hole pair radiates energy at the same value as the incident light. This commonly-occurring process in very strong in crystals, and is called Rayleigh scattering, which is the incoming frequency is the same with the scattering frequency. Raman spectra is observed when scattering light frequency is lower or higher than incoming light, i.e. the scattering process is inelastic. Since Raman is weaker than predominant elastic Rayleigh scattering, a notch filter and line filters are used detect the inelastically scattered Raman light. The Figure 2.6 below shows the typical transitions in a solid that give rise to optical signals with frequencies that are shifted from the incident frequency. The shift in the peaks with respect to the original incident frequency is called Raman shift, and is directly related to the energy of a certain phonon mode at various symmetry points of the first Brillouin zone. The phonon band structure of $MoSe_2$, for example, calculated using first principles density functional theory by our collaborators [Prof. Humberto Terrones, Renssealaer Polytechnic Insitute] is presented in chapter 4.

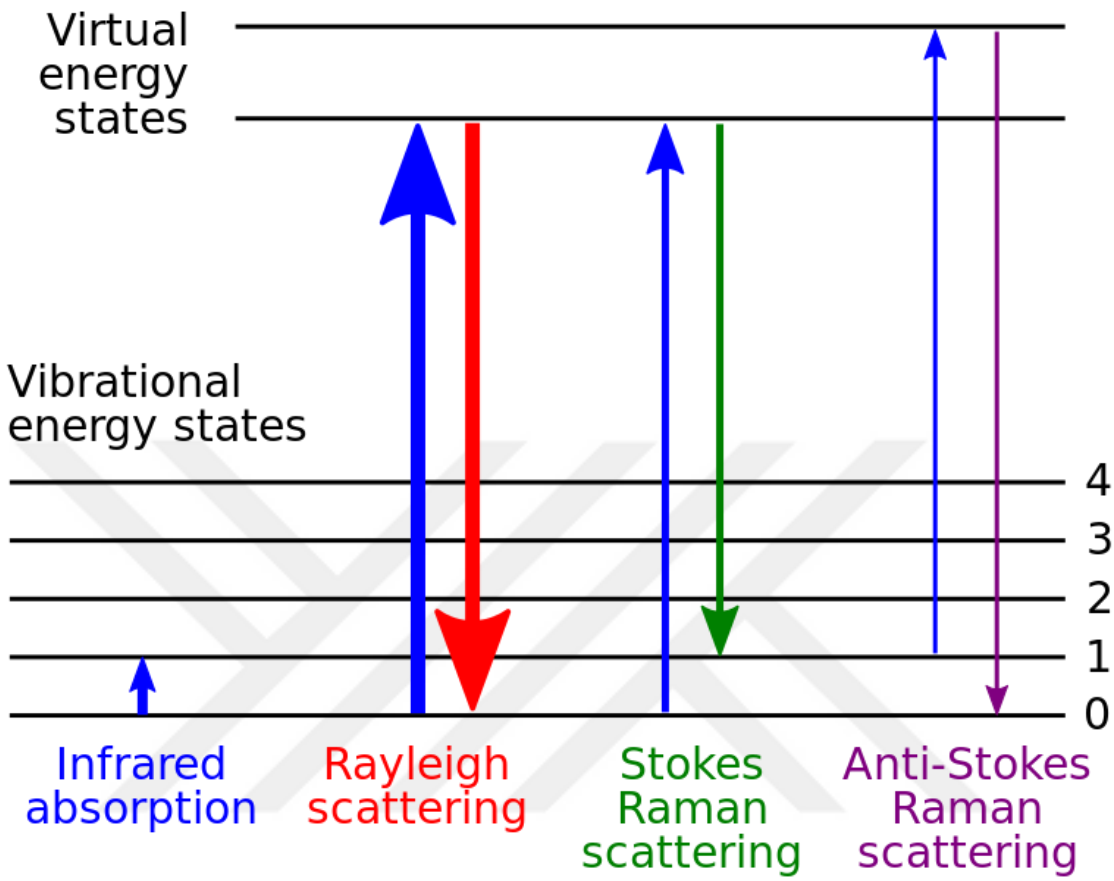

Figure 2.6: Energy level diagram with various possible types of optical scattering processes seen in solids. (Reproduced from Ref.[91])

While Raman spectra probes into processes that require interactions between photons, electrons and phonons, pure electronic transitions also give rise to peaks which are independent of the carrier frequency, and depend on transition between band to band. When these transitions are purely vertical, *i.e.* they only reflect changes in energy of the electron without any change of momentum, then the recombination process is usually radiative as it does not require the inclusion of inelastic processes. Such

peaks are usually described as photoluminescence peaks, and are related to direct-gap deexcitations of electron-hole pairs. Photoluminescence (PL) is observed in higher frequencies (energies) in the Raman spectrum. When lights are absorbed, electrons are excited to higher electronic states, then, after short time, it releases back to ground state by emission a photon. Conventionally, a PL peak will be observed at a value close to the electronic band gap of a semiconductor, and hence is often considered to be a measure of the band gap. However, as it so happens, the electron-hole pairs are strongly bound in the form of excitons in TMDs, with large binding energy values that exceed few hundreds of millielecton volts. Excitons have ground state energies that are lower than the electronic gaps, and hence the PL peaks positions in TMDs are measures of these ground state energies, and not the energy gap between the valence band maxima and conduction band minima. These electronic (or quasiparticle) band gap values can be ascertained using STM tunneling spectroscopy (which we do not have possess in our lab), as well as photoabsorption spectroscopy (shown later in Section 2.5) and photocurrent spectroscopy, which will be presented in chapter 3.

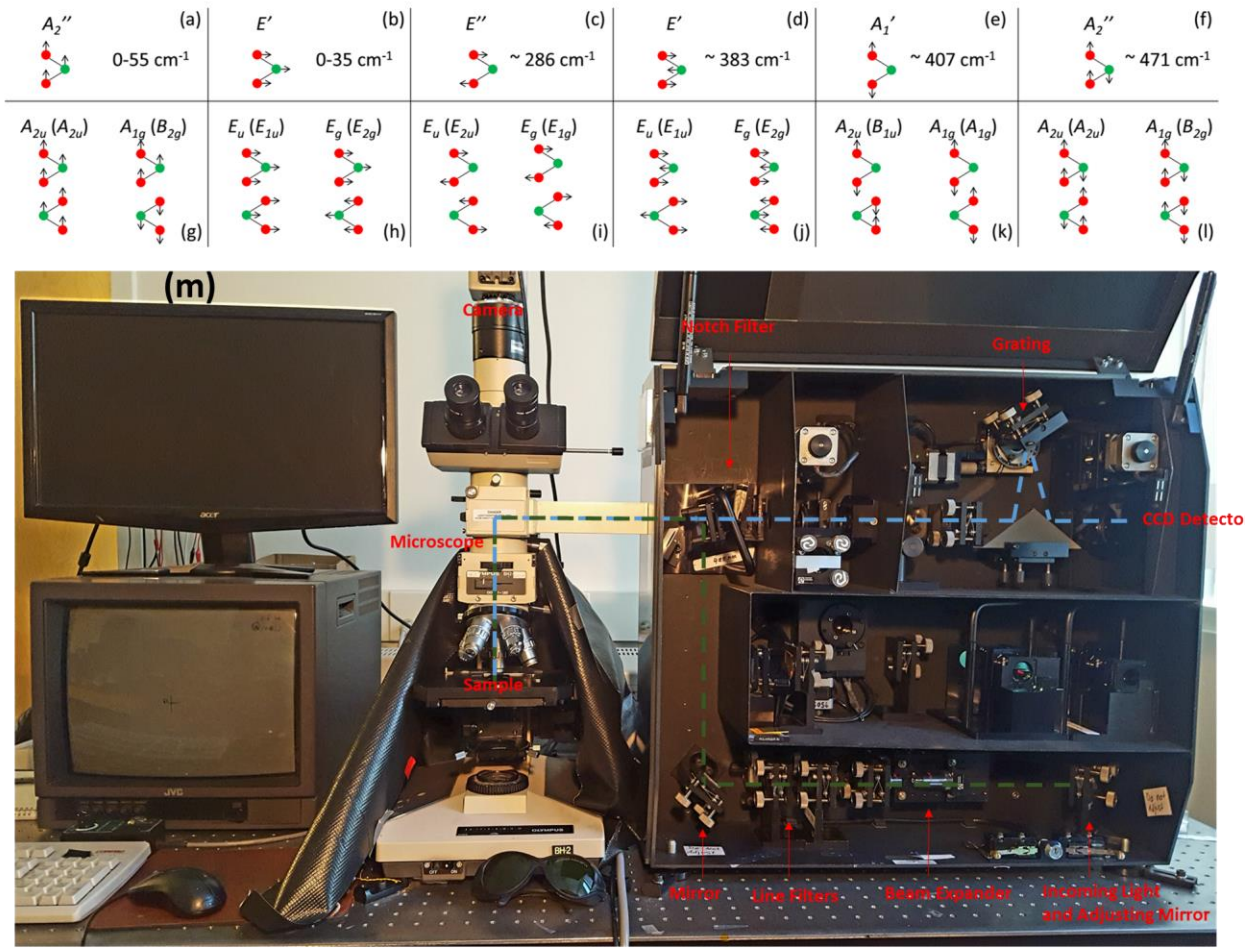

Figure 2.7: The vibrational patterns of the normal modes for single layer MoS_2(a-f), and bilayer (g-l). (Image reproduced from Ref.[92]) (m) A photograph of Raman spectrometer used in our lab (Renishaw Ramascope).

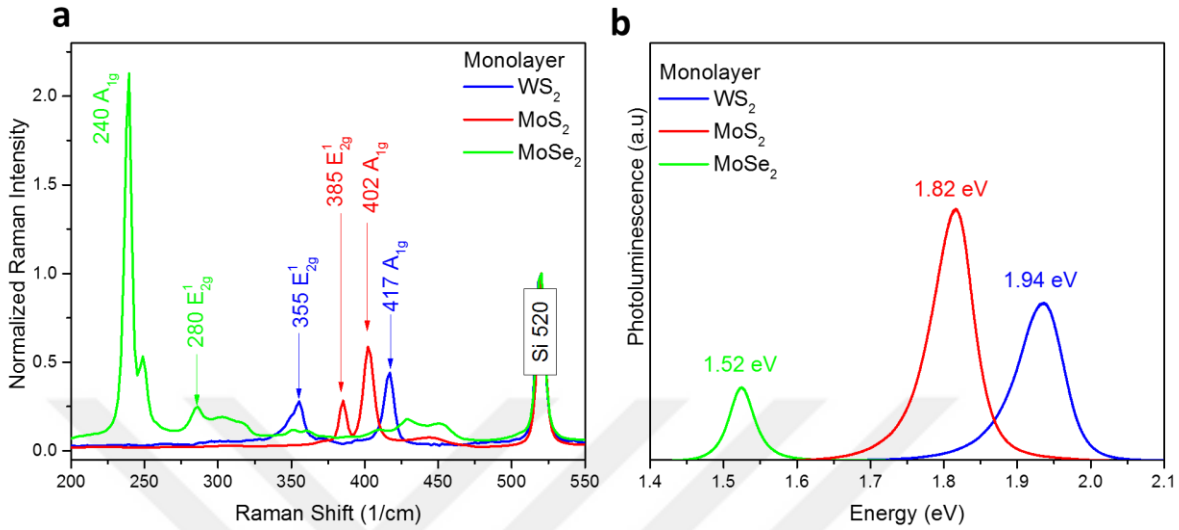

Figure 2.8: a) The major Raman peaks for VPC-grown monolayer WS_2, MoS_2, and $MoSe_2$. b) Monolayer PL spectra for various TMDs grown with our method.

Raman Spectroscopy is one of the fastest tools to define the materials we synthesis in the lab. The Figure 2.8 shows an example of experimentally obtained Raman and photoluminescence spectra of vapor phase chalcogenization(VPC) grown monolayer TMDs. In Figure 2.8a, the Raman spectra includes two major peaks from in plane (E^1_{2g}) and out of plane (A_{1g}) vibrational modes for various TMDs. By looking energy difference between these two major peaks, we can define the number of layers for WS_2 and MoS_2 from spectra. The frequency difference corresponds to monolayer if it is less than 20 cm^{-1} and 64 cm^{-1} for MoS_2 and WS_2 respectively. This feature may not be used to define number of layers for $MoSe_2$. In Chapter 4, we explained in a better way to define monolayer of $MoSe_2$. The Figure 2.8 b shows the PL spectra taken with 488 nm excitation. Strong PL emission is observed at 1.52, 1.82, and 1.94 eV for $MoSe_2$, MoS_2, and WS_2 respectively. We also performed Raman mapping on our samples to see the

uniformity of the flakes over large area. The Figure 2.9 shows the optical image of monolayer WS_2 and the intensity of the major A_{1g} and E^1_{2g} peaks.

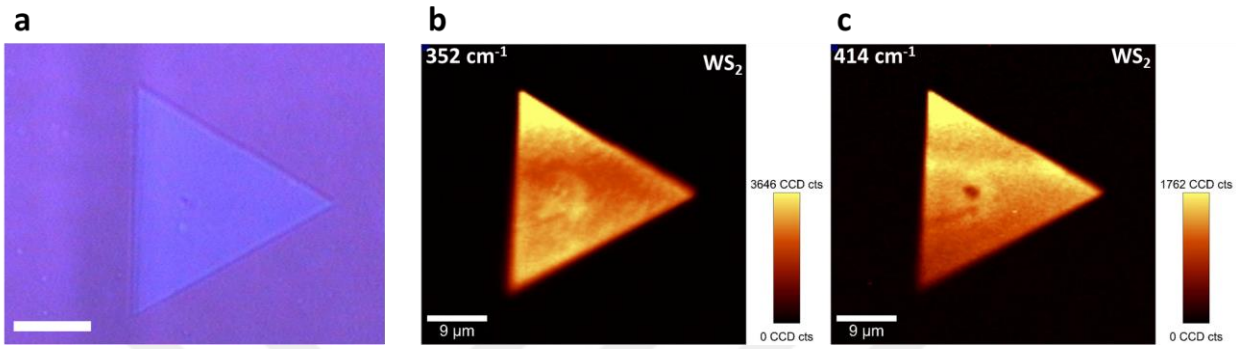

Figure 2.9: (a) Optical image of monolayer WS_2 (scale bar is 10 microns). Raman mapping of the E^1_{2g} (352 cm^{-1}) and A_{1g} (414 cm^{-1}) modes. (excitation wavelength 532 nm)

2.5 Photoabsorption Spectroscopy

The electronic band gap and excitonic peaks of 2D materials can also be investigated using photoabsorptions spectroscopy. Our spectrophotometer does not directly measure photoabsorption, and hence we used an approximate method to obtain photo absorption from transmittance measurements, and converted them into Tauc plots to obtain the necessary band gap information. Transmittance curves of 2D crystals were measured by a custom-built UV/Vis absorption microspectrometer. Monochromatic light from a monochromator (200 nm-1000 nm) was focused by a 50X objective and chopped at 200 Hz to reduce the noise. The power was attenuated below 10 µW to avoid the effect of high-power light. Below we show how this can be used to approximately estimate the band gaps of our samples.

Let us assume that light of intensity I_e is entering a 2D crystal of thickness *x*, and is partially absorbed and the rest is transmitted. Applying Beer-Lambert law, the transmitted light intensity I_T is given by:

$$I_T = I_e e^{-\alpha x},$$

where the absorption coefficient $\alpha = -\frac{1}{x}\ln(T)$, with $T = \frac{I_T}{I_e}$ = transmittance of the 2DHC when reflectance is negligible.

However, in our experiment, I_e is unknown since the reflectance is unknown. Hence, we calculated the transmittance in terms of the known incidence intensity I_i,

$$I_T = (I_i - I_r)e^{-\alpha x},$$

where, I_r is the intensity of the reflected light. Hence, the experimentally measured transmittance,

$$T = \frac{I_T}{I_i} = (1 - \frac{I_r}{I_i})e^{-\alpha x} = (1 - R)e^{-\alpha x},$$

where, $R = \frac{I_r}{I_i}$ =reflectance of the sample.

As before, we calculate

$$-\left(\frac{1}{x}\right)\ln(T) = -\left(\frac{1}{x}\right)\ln(1 - R) + \alpha.$$

Using Taylor expansion,

$$\ln(1-R) = -R - \frac{(-R)^2}{2} + \frac{(-R)^3}{3} \ldots,$$

and stopping at the leading order as R<<1 as T>90% near the transmittance edge for all samples, we obtain

$$-\left(\frac{1}{x}\right)\ln(T) = \left(\frac{1}{x}\right)R + \alpha$$

According to the work by Dhakal *et al.*[42], who have performed detailed investigation of absorbance on 2D-MoS_2 samples using reflectance spectroscopy, the measured reflectance of atomically-thin materials on a transparent substrate (similar to our case) can be directly related to the absorption coefficient through the relationship:

$$R_N = \frac{4n}{(n_s^{\ 2} - 1)}\alpha\,,$$

where n and n_s are the refractive indices of the 2D layer and the substrate, respectively. Dhakal *et al.* demonstrate that the refractive indices can be assumed to be approximately constant over the range of energies under consideration. Hence,

$$-\left(\frac{1}{x}\right)\ln(T) = C_1\alpha + \alpha = C_2\alpha\,,$$

where, C_1, C_2 and *x* are constants. Since the RHS is still proportional to α, we can use the quantity $-\ln(T)$ to substitute for α in estimating the transmittance edge using a Tauc plot[93] . The quantity { $-\ln(T)$hν}$^{1/\eta}$ was plotted as a function of photon energy hν where h is Planck constant, ν is the photon

frequency and η=1/2, 3/2, 2, or 3 for direct allowed transitions, direct forbidden transitions, indirect allowed transitions, and indirect forbidden transitions, respectively. Depending on whether the samples were monolayered (direct gap) or multilayered (indirect gap), appropriate values of η=1/2 and 2 were used to fit the plots of $-\ln(T)$hν *vs*. Hν (Tauc plot). The Figure 2.10 below shows the Tauc plot for monolayer MoS_2, in which the quasiparticle band gap of 2.61 eV could be obtained using an extrapolation of the linear, band-like region of the Tauc spectrum.

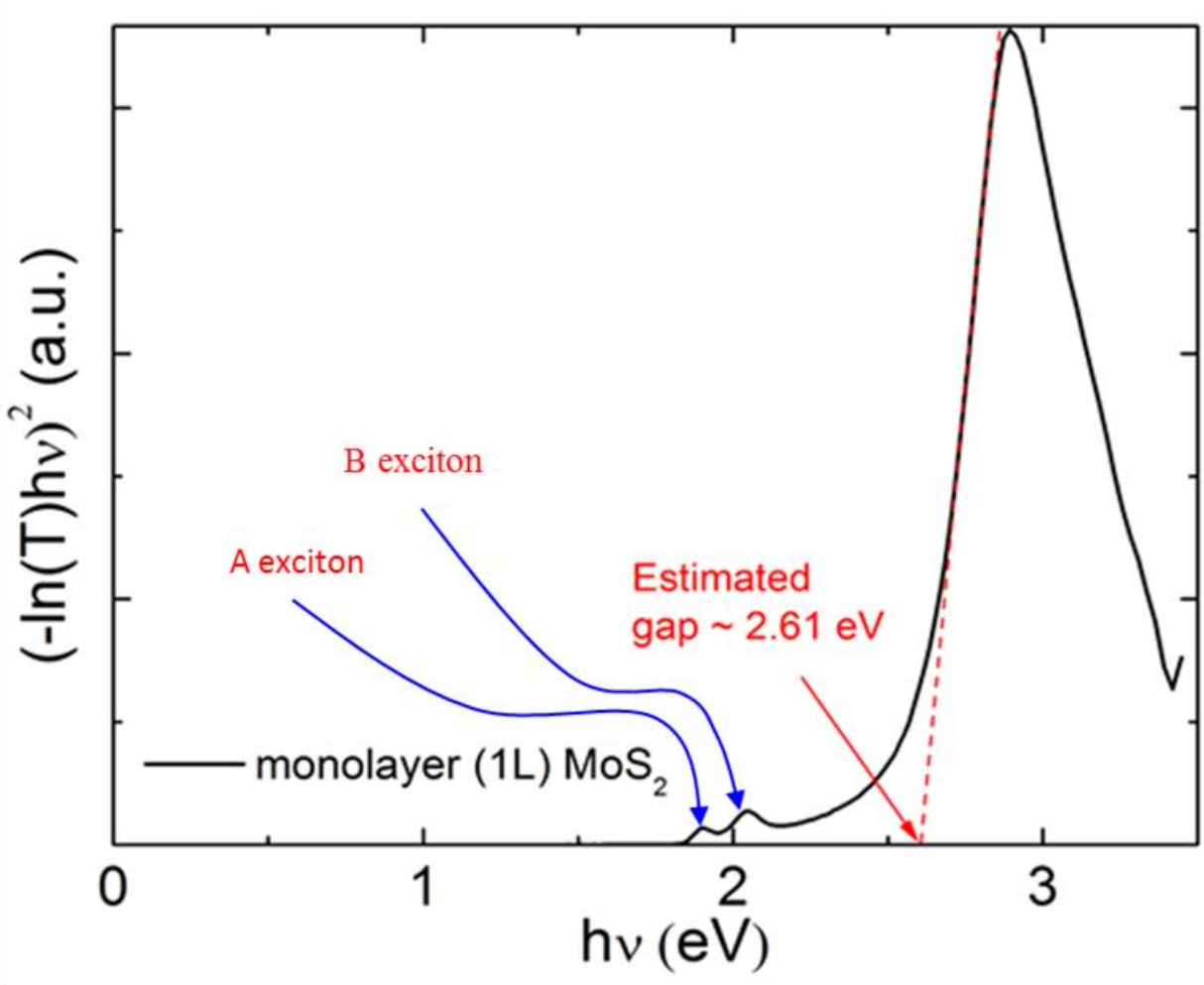

Figure 2.10: Absorption Spectrum for monolayer MoS_2 to calculate excitonic band gap and quasiparticle band gap. (This work is unpublished-Manuscript under review)[94]

2.6 Fabrication of Field Effect Transistor Devices

2.6.1 Photolithography

Photolithography is used for making pattern (large electrode and markers, see Figure 2.12a) on wafer scale 300 nm SiO_2/Si. These patterns are then used for fabrication of FET devices. Procedures:

1. S1813 positive photoresist was spin coated with 4000 rpm 60 second. This enables us to obtain 300 microns of film.
2. Bake the photoresist coated wafer on a hot plate for 1 minutes at 115 °C.
3. Place the wafer and mask to Quintel mask aligner. Detailed information about operating Quintel mask aligner can be find on Kostas website (https://kostas.aeroweb.net/). UV light exposure time for S1813 is 2.5 seconds under vacuum contact mode.
4. Exposed photoresist, develop wafer for 45 seconds in AZ 726 MIF developer.
5. Rinse in deionized water to remove completely developer, and blow dry with nitrogen.
6. Deposite thin film layer of Ti/Au, and lift off in acetone 30 minutes

2.6.2 Electron Beam Lithography

Electron beam lithography (EBL) provides high resolution patterning. Fabrication processes of FET devices are explained step by step as following:

1. Monolayer TMDs samples (MoS_2, $MoSe_2$ and WS_2) grown on 300 nm Si/SiO_2 is spin coated with PMMA C4 or A4 at 4000 rpm for 60 seconds and baked 135 °C for 2:30 min. Then the sample was immersed in 1M KOH solution for an hour to remove SiO_2. Once a PMMA/TMD film is

separated from silicon, it is rinsed three times in deionized water to wash KOH residues. The PMMA/TMD film is then transferred to new prepattern substrate, which includes marker for accurate writing EBL. Once the PMMA/TMD is well dried on new substrate, the substrate is soaked in acetone to remove PMMA, then followed by IPA cleaning. This etching process may take long time and may leave same KOH residues on samples. Low concentrated 1-5 % HF solution can be used to etch SiO_2 layer in less than 5 minutes. Another transfer method without using chemical etchants is hot water treatment. PMMA coated sample is placed to water beaker at 90 °C for one hour. Edge of the sample is scratched to enable water to penetrate between the layers. This method is previously shown on clean transfer of graphene[95]. The summary of the transfer process is shown in Figure 2.11.

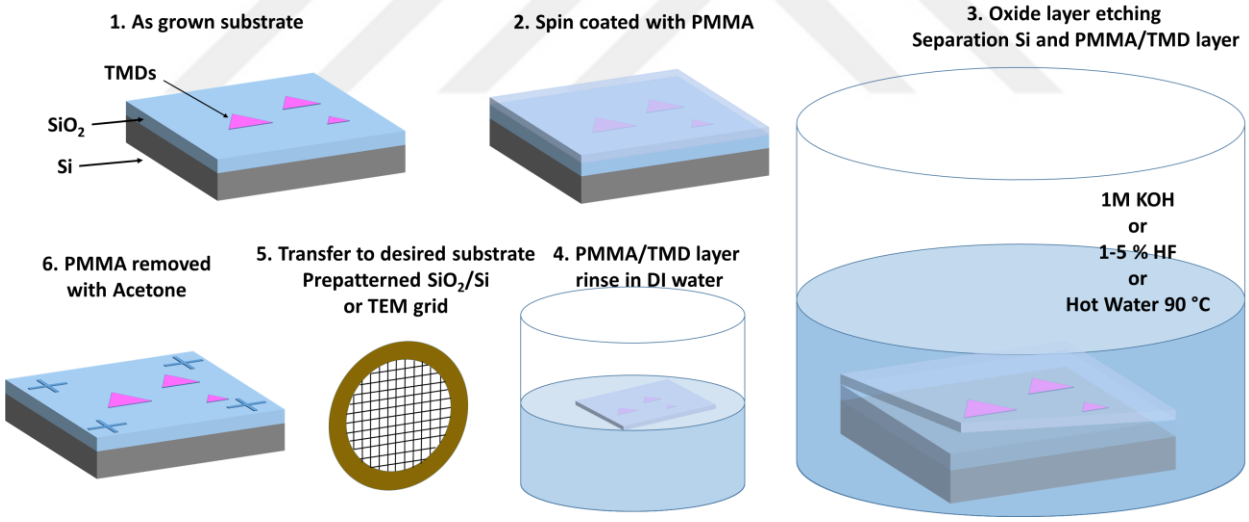

Figure 2.11: Schematic illustration of PMMA transfer method for TMDs.

2. The transferred TMDs on prepattern substrate is spin coated with PMMA A4 at 4000 rpm for 60 sec and baked at 185 °C for 90 seconds for e beam lithography.
3. The FET electrodes are drawn using AutoCAD or DesignCAD program. The files are saved on dc2 file that can be recognized Nanometer Pattern Generation System(NPGS). The area dose depends on the used PMMA resist. Area dose is used 250 $\mu C/cm^2$. The beam current for small feature is 200 nA with aperture size 30 µm, while it is 1.5 nA with aperture size 120 µm for large shape.
4. After EBL writing, the substrate or sample is immersed into (Methyl Isobutyl Ketone) MIBK: IPA (isopropyl alcohol) solution for 90 seconds to remove the exposed patterns. The substrate is then rinsed with IPA.
5. The electrodes (5 nm Ti/50 nm Au) were deposited by e –beam evaporator with rate deposition 1 A°/s and 3 A°/s respectively. Lift off process is performed with acetone followed by IPA cleaning.

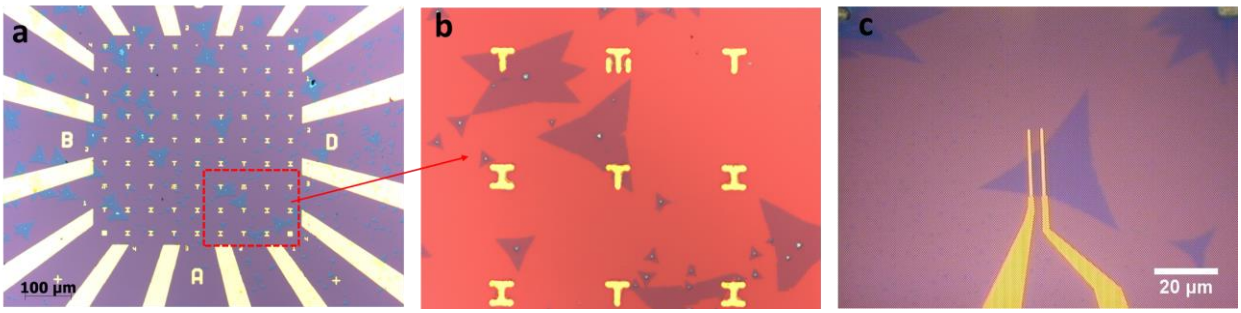

Figure 2.12: a) Monolayer MoS_2 transferred on SiO_2/Si substrate including large electrodes with markers. b) Magnified image of selected rectangular area in red. c) An optical image of FET device after lithography and Ti/Au deposition.

Chapter 3: Investigation of Optoelectronic Properties of MoS_2

3.1 Introduction

In recent times, there has been a rapidly growing interest in atomically thin, layered, or 2D materials beyond graphene.[96] Confined in a 2D-plane, these materials demonstrate a range of exciting properties such as emergent photoluminescence,[97] anomalous lattice vibrations,[98] control of valley polarization using optical helicity,[44,99] excitonic dark states,[23] and strong light-matter interactions at heterojunctions,[100] and have immense potential for next-generation transistors with extremely high on-off ratios,[13] photodetectors,[101] catalysis[102] and other applications. Among the variety of materials being investigated, atomically thin molybdenum disulfide (2D-MoS_2) has emerged as one of the most promising candidates for low cost, flexible and highly sensitive next-generation nanoelectronic [13,101,103,104] and optoelectronic devices such as photodetectors, photovoltaics, and light emitting diodes.[105-109] Unlike graphene, 2D-MoS_2 is a true semiconductor with layer-thickness-dependent band gap that becomes direct at the monolayer limit (E_g ~1.85 eV).[97,110] The direct band gap in monolayer MoS_2 is extremely attractive both for light-emission applications, as well as for photocurrent-based applications since it is possible to obtain valley polarization of excitons using circularly polarized light.[44,99] Moreover, the sheet resistance of atomically thin MoS_2 can be modulated significantly by either applying a gate voltage or by incident light, making it valuable for diverse electronic and optoelectronic applications. These properties overcome the fundamental drawbacks of graphene-based electronic devices that are limited by a lack of band-gap, wavelength-independent weak optical absorption of about 2.3%,[111] and extremely fast non-radiative recombination of photogenetated electron-hole pairs,[112] and hence enable a wide range of applications in nanoelectronic and

optoelectronic devices such as photoemitters, phototransistor and photodetectors. To successfully utilize these attractive attributes of 2D-MoS_2, and to integrate them into existing optoelectronic platforms require scalable synthesis of large-area, high quality single-crystal (possibly monolayer) samples with uniform electronic/optoelectronic responses. At this point, simultaneously accomplishing these conditions for 2D-MoS_2 still appears to be an open quest, especially for optoelectronics. Conventionally, the highest quality samples are usually those obtained by mechanical exfoliation of bulk MoS_2. Field-effect transistors (FETs) using exfoliated MoS_2 exhibit high saturation currents >100 µA/µm with a factor of difference $>10^6$ between the ON state and OFF state, and the field effect mobilities between 0.1 and 10 $cm^2V^{-1}s^{-1}$.[13,14,105] Mechanically exfoliated MoS_2 is also sensitive to a certain range of the visible spectrum, making it appealing for photodetection.[113] However, certain low-intensity optoelectronic processes are difficult to observe even in exfoliated samples. For example, it has been recently shown that demonstration of excitonic states in photocurrent spectra of 2D-MoS_2 using photocurrent spectroscopy in exfoliated samples require utmost care in device fabrication, including suspending the layer to remove deleterious effects of the substrate, *in-situ* annealing, and performance of measurements in low temperatures.[41] Moreover, although first order-Raman spectra of 2D-MoS_2 has been studied in extreme detail in this system, low-intensity multi-phonon processes and higher-order Raman peaks have been reportedly observed, in a very limited manner, only in exfoliated samples.[114-116]

In this work, we present the synthesis and characterization of highly crystalline single- and few-layered samples of 2D-MoS_2 with large-area single domains, by direct sulfurization of MoO_2 in the vapor phase. We believe that the direct vapor-phase sulfurization of MoO_2, represented by the single-step chemical reaction $MoO_2 + 3S \rightarrow MoS_2 + SO_2$, circumvents the need for any intermediate chemistry, and leads to samples of higher quality. We show that controllable mono-, and few-layer MoS_2 can be grown on a

variety of substrates using MoO_2 as a precursor. The high degree of uniformity of these samples could be verified by direct and differential Raman mapping, as well as through PL mapping. Multi-layer samples that have well-defined geometric shapes enable us to observed layer-thickness-dependent evolution of a range of multi-phonon and higher-order Raman processes that have previously never been observed in CVD-grown MoS_2 samples. More importantly, we have been able to observe two new *layer-thickness-dependent* Raman modes that have previously never been reported in *any* MoS_2 samples. Back-gated measurements in FET configuration shows high saturation current and an ON/OFF ratio ≈ 10^6. Finally, a direct reflection of the high crystalline quality of our samples is the observation of the clear peaks (even at room temperature) in energy-resolved photocurrent measurements that correspond to excitonic states in single-layer MoS_2. Exciton-generated peaks in photocurrent spectroscopy has never been observed before in CVD-grown 2D-MoS_2, and has been recently reported to occur only in artificially-suspended, mechanically exfoliated 2D-MoS_2 samples. This spectroscopic tool allows us to clearly resolve the two primary excitonic peaks in 2D-MoS_2, unlike photoluminescence peaks that strongly overlap. This provides a powerful method to investigate the independent and comparative evolution of each peak as a function of carrier energy (tuned using voltage and temperature). These investigations provide a fundamental platform for understanding the optoelectronic properties of large-area, CVD-grown 2D-MoS_2.

3.2 Results and Discussions

Single and few-layered MoS_2 samples were fabricated by direct sulfurization of MoO_2 (see chapter 2.1 for details) as a precursor instead of commonly used MoO_3 and Mo, and without any treatment to the precursor[79,82] or substrate[77]. This latter feature is quite useful, since pretreatment of substrates has been shown to be detrimental to the intrinsic properties of 2D materials.[117] Figure 3.1 outlines a range of different types of samples that can be readily obtained by our method, and on a range of substrates. In a separate work, we have now also developed a method for substrate-free direct synthesis of MoS_2 across micron-size apertures using the same precursor, which has been reported elsewhere.[118] Figure 3.1(a) shows optical and SEM images of single-layer MoS_2 grown on a variety of substrates including amorphous, crystalline, transparent, and conductive substrates, with typical sample edge-sizes ranging from 10-50 µm. It is indeed quite remarkable that despite their variety, this single-step synthesis method requires no pre-treatment of either the precursor or the substrates. The ability to readily synthesize these samples on a range of substrates makes it convenient to utilize these as-prepared samples to be directly implemented in a variety of nanoelectronic, optoelectronic, and catalytic (including photo/electro-catalytic) applications. Moreover, these as-grown samples (free of transfer-induced contamination) on such a variety of substrates are also potentially attractive for a range of advanced metrology tools such as STM, TEM, ARPES, and various optical spectroscopies, to name a few.

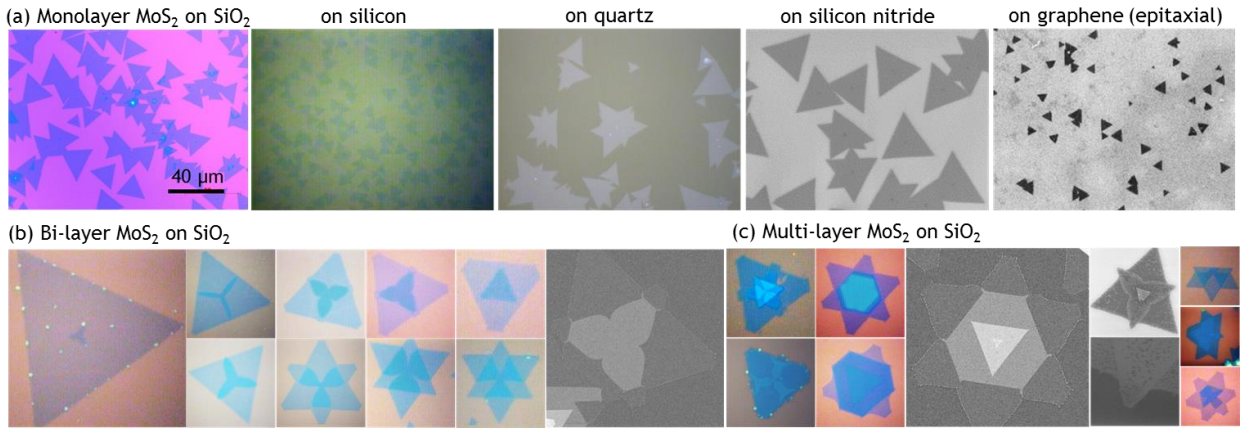

Figure 3.1: Typical example of monolayer MoS_2 samples grown using MoO_2 precursor, on different substrates. Colored images are optical, and B/W ones are SEM images. (b) Typical optical and SEM images of bi-layer MoS_2 samples fabricated on SiO_2. Various states of initiation and growth of the second layer have been represented by these images. The final image in (b) is an SEM image showing intricate details of the bilayer structure. (c) Optical and SEM images of a range of multi-layer samples at various stages of growth and with various shapes and morphologies.

Changing the synthesis conditions triggers second layer growth vertically on top of the first layer. Figure 3.1b outlines a typical array of samples at various stages of second-layer growth on SiO_2 (see chapter 2.1 for additional details). In several cases, we also see growth of third and higher layers (Figure 3.1c). Growth of multiple layers is unsurprising as MoS_2 exhibits a natural tendency to grow as a 3D crystal[119]. Of interest is the growth morphology of the second and higher layers which are varied and in stark contrast to the growth of the first layer. The substrate-independent morphology of the first layer suggests that it is likely a Wulff shape composed of either low energy edges (near-equilibrium shape), or kinetically-limited edges (far-from-equilibrium kinetic shape). The three-fold symmetric shape is consistent with past reports on MoS_2 growth using oxygen-rich precursors[78], indicating that the

thermodynamic and kinetic conditions at the growing edges in our direct sulfurization process are not dramatically altered.

The concurrent growth of the second layer indicates that its rate of areal increase is fast relative to the first layer. As confirmation, the second layer coverage always increases over time. The fast growth rate suggests that the accumulation of precursor molecules is mediated by the underlying first layer. As discussed earlier, in contrast to sulfurization of MoO_3, which involves the intermediate formation of MoO_{3-x}, the ability to grow these samples using a direct vapor-phase sulfurization of MoO_2 may imply a faster growth kinetics. This may at least be partially responsible for the rapid formation of the second layers. The shape is again three-fold symmetric but dendritic, and the primary arms usually grow towards center of the edges triangular first layer, *i.e*. the second layer is rotated by ($\pi/3+\theta$) with respect to the first layer, where θ is the relative stacking-based lattice rotation between the two layers that lowers the energy of the two layers[120]. The morphology of an early stage seed is shown in Figure 3.1 b. The presence of the first layer also modifies the anisotropy in the shape. To see this, note that as the areal coverage of the second layer increases, the growth morphology becomes progressively less dendritic (right, Figure 3.1b) The primary arm pinches off and the shape asymptotes towards a rotated triangular (top right row, Figure 3.1b) and in other cases the dendritic tip flattens out in a ``wine glass" fashion as it approaches the edge of the underlying first layer (bottom right row, Figure 3.1). The SEM images in Figure 3.1 b and c which appear to provide evidence of grain boundaries, suggests that it may be the presence of such grain boundaries that initiate the formation of the dendrite structures, although detailed further studies will be required to arrive at a firm conclusion.

Taken in toto, the dendritic growth is reminiscent of diffusion-limited growth (DLG)[121], likely due to slow diffusion of precursor molecules to the growing edges. The accelerated growth can lead to a transition in the growth dynamics, and this has been observed in oxygen-controlled growth of single layer graphene domains[121]. In the case of bilayer growth as is the case here, our results indicate the morphological relation between the two layers, suggesting a strong influence of crystal symmetry of the first layer on the kinetic shape. The anisotropy can be a combined effect of first-layer mediated diffusion of precursor adaptors and/or attachment-detachment kinetics at the growing edge (aggregation limited growth, ALG)[121]. Similar kinetic effects shape the growth of the third and higher layers.

Interestingly, as the edges of the two layers begin to interact and compete for the attachment of precursor molecules, we see growth of another dendrite from the first layer. This is quite common in the first two layers, and results in an overall star-shaped morphology of the first layer. The dendrites appear to have a different lattice orientation and are therefore separated by the grain boundaries; localized contamination at these boundaries is visible in the SEM images in Figure 3.1b and c. These new domains can result from overgrowth of the second layer mediated by the edge of the first layer, or a net effect of inter-edge interaction that starves the growth of the second layer by facilitating nucleation and edge-by-edge growth of new domains at the edges of the first layer. We conclude that the system provides an interesting platform for controlling the shape and morphology of atomically thin crystals.

Since 2D materials are known to show strong layer-thickness dependent properties, the ability to controllably synthesize these samples with various layer-thicknesses, that too on a variety of substrates (not shown) opens up several significant layer-thickness-dependent nanoelectronic and optoelectronic investigative directions as well as applications. Next, we establish the quality of these samples using

Raman and Photoluminescence Spectroscopy and mapping, and present results of these Raman spectroscopy as a function of layer thickness and on different substrates.

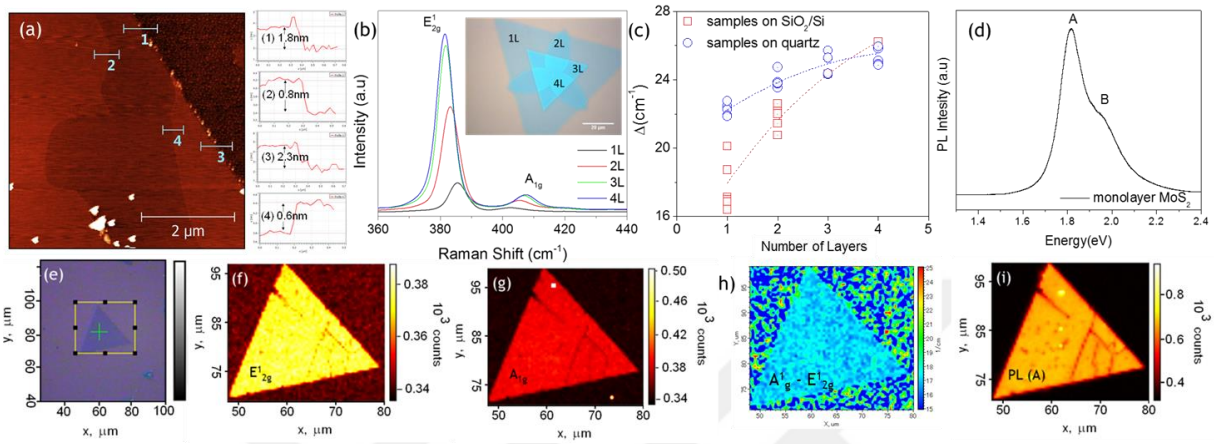

Figure 3.2: (a) AFM image of a few-layered sample, with incomplete top-layer, such that the top-layer thickness can be measured using the cross-section step height, as shown on the side. (b) Raman spectra from regions of various layer-thickness from a multilayer sample (Inset: optical image), showing the evolution of the dominant E^1_{2g} and A_{1g} peaks for different layer-thicknesses. (c) Variation of the peak position separation, $\Delta = \omega[A_{1g}]-\omega[E^1_{2g}]$, as a function of layer-thickness in samples grown on SiO_2/Si and quartz substrates. The spread in data point for each layer corresponds to 4-6 data points that were collected from different samples. (d) Typical Photoluminescence (PL) spectrum obtained from a monolayer MoS_2 sample, showing the A and B excitonic peaks. (e) Optical image of a monolayer sample, which was used to perform Raman and PL mapping, as shown in (f) Raman map of $\omega[E^1_{2g}]$, (g) Raman map of $\omega[A_{1g}]$ (h) Raman map of $\omega[A_{1g}]-\omega[E^1_{2g}]$ and (i) PL map of the Excitonic A-peak.

Figure 3.2 shows the AFM topographical image at the edge of a multi-layer sample. Cross-sectional step-height measurement from various regions of a partially unfinished top-layer, as shown on the right, establishes that the single-layer thickness of MoS_2 ranges from 0.5-0.8 nm, the variation could be attributed to the roughness of the underlying SiO_2 substrate. Figure 3.2b shows the dominant Raman

peaks measured from a sample with very well-defined and characterized 1,2,3, and 4-layer regions, shown in the inset, measured with an incident laser of wavelength = 488 nm (2.54 eV). The two most dominant peaks seen correspond to the first-order E^1_{2g} and A_{1g} modes at the Γ-point of the hexagonal Brillouin zone of 2D-MoS_2, for different layer thickness values. We note that the low intensity of the A_{1g} peak is due to the polarized configuration of the Raman system.[122] The A_{1g} peak can be fully recovered by adding a half waveplate (see Figure 3.7 in Supporting Information). As reported earlier[77,79,123], the E^1_{2g} peak position ($\omega[E^1_{2g}]$) red-shifts, while the A_{1g} peak position ($\omega[A_{1g}]$) blue-shifts with increasing layer thickness, resulting from the growing influence of inter-layer coupling on the electron-phonon processes in 2D-MoS_2. Figure 3.2c shows the variation of $\Delta = \omega[A_{1g}]-\omega[E^1_{2g}]$, the difference in peak-position between the E^1_{2g} and A_{1g} modes, as function of layer thickness, measured from multilayered samples grown on SiO_2/Si and quartz substrates. In samples grown on SiO_2 substrates, we see ~20% variation in the value of Δ in monolayers, ~10% in bilayer samples, and almost negligible variations in 3 and 4 layered samples. In contrast, there is about 3-5% variation in Δ for all samples grown on quartz, independent of their layer-thickness. This leads us to believe that substrate-induced effects (*e.g.* doping due to impurities and trapped charges, substrate-sample interactions, strain and even sample background noise as seen in Figure 3.2h) may play a measurable role in the measured optoelectronic properties of 2D-MoS_2, and these effects vary substantially from substrate to substrate. Indeed, these interactions could also be responsible for the differences in the behavior of other Raman spectroscopic features, as discussed later.

Monolayer MoS_2 is a direct band-gap semiconductor,[97,110] and when e-h pairs in monolayer MoS_2 are excited with photons of energy larger than this gap size of E_g~1.85 eV, they recombine radiatively, giving rise to a photoluminescence (PL) spectrum that contains two distinct peaks. These corresponds to

transitions from the lowest energy point of the spin-orbit-split lowest conduction bands to the highest point of the valence bands, commonly designated as A and B peaks in monolayer MoS_2. Figure 3.2 shows the PL spectrum of a typical monolayer MoS_2 sample, where the A and B peaks are found to be centered around 1.82 eV and 1.94 eV, respectively. The Raman and PL peaks obtained in these samples have been used to demonstrate the optoelectronic homogeneity of these samples. Figure 3.2e shows a typical monolayer MoS_2 sample on which extensive Raman and PL mapping were performed. Figure 3.2f-h show pseudo-colored maps, where the colors represent the values of the direct ($\omega[E^1_{2g}]$ and $\omega[A_{1g}]$) and differential ($\Delta=\omega[A_{1g}]-\omega[E^1_{2g}]$) peak positions for the E^1_{2g} and A_{1g} peaks. The excellent uniformity of the direct peak position maps (other than the few streaks corresponding to wrinkles in these 2D materials) reflects the high degree of uniformity within each monolayer crystal. The differential peak position map shows a uniformly distributed background noise which can at least be partially responsible for the variation of Δ seen in c Although the uniformity could not be clearly established in the differential map owing to these large background fluctuations, similar degree of uniformity could also be found from the PL map of the A peak, as seen in Figure 3.2c. With the help of these measurements, we establish the uniform nature of the quality of these samples. We next present more evidence of the extremely high quality of these CVD-grown samples with the help of previously unreported, multi-phonon processes in the Raman spectra as a function of layer-thickness.

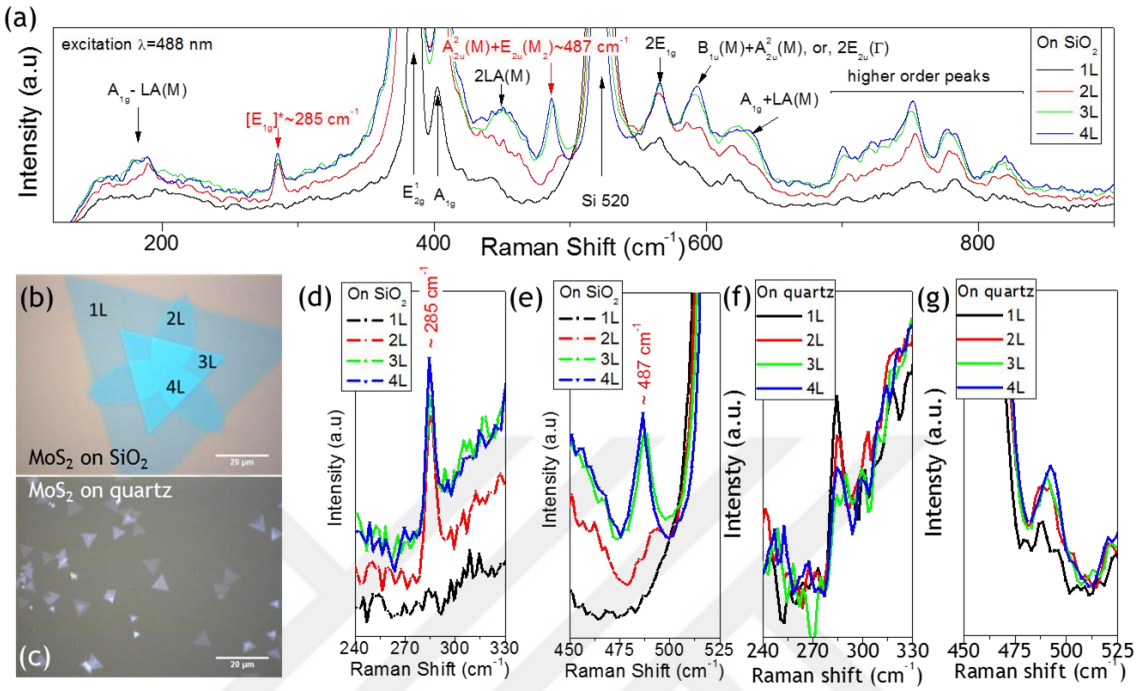

Figure 3.3: (a) Typical survey scan of several first-order and multi-phonon processes identified in monolayer and few-layered 2D-MoS_2 samples synthesized on SiO_2/Si. The intensities of most of these processes are much weaker than the two dominant processes E^1_{2g} and A_{1g}, and have been labeled as shown. The two labels in red are previously unreported peaks (see text). (b) The few-layered CVD-grown sample synthesized on SiO_2/Si (same as figure 2b Inset), and (c) representative few-layered CVD-grown samples synthesized on quartz that were used to investigate the layer-thickness-dependence of the two new peaks, details of which are shown in (d)-(g). (d), (e) Absence of Raman peak at ~285 cm-1 and ~487 cm-1 in monolayer samples that appear in samples with more layers, as seen in 2D-MoS_2 grown on 300 nm of SiO_2 on silicon. (f)-(g) Averaged layer-thickness variation of the same peaks when measured on 2D-MoS_2 grown on quartz (see text).

Figure 3.3a shows the low-intensity region of the same curves plotted in Figure 3.2b revealing a rich range of first order and multi-phonon processes. Such large number of Raman peaks have previously not

been reported in CVD-grown samples, and were confirmed to be present in all our samples tested, including samples grown on different substrates. A number of peaks could be labelled with the help of past reports on bulk or exfoliated MoS_2 samples, and are labeled in black.[114-116,124] A broad peak is observed around ~454 cm^{-1}, which is attributed to second order longitudinal acoustic phonons near the M-point of the Brilluoin zone (2LA(M)) of MoS_2, although the first-order LA(M) phonon[116] was absent when measured using λ=488 nm (E_{ph} = 2.54 eV) in our samples. The broadness of this peak is consistent with past reports that it is a combination of three[115] to five[124] closely placed peaks. The LA(M) phonons also combine with A_{1g} phonons to give sum (A_{1g}+LA(M) at ~635 cm^{-1}) and difference (A_{1g}-LA(M) at ~184 cm^{-1}) peaks. A peak at ~595 cm^{-1} could be either due to a combination of B_{1u}(M)+A^2_{2u}(M) phonons, or a second-order $2E_{2u}$(Γ) peak; most likely a combination of the two. A range of higher-order peaks were also clearly observed between the range of 700-850 cm^{-1}.[124]

The most interesting features observed in our samples are two previously unreported peaks at ~285 cm^{-1} and ~487 cm^{-1} (during the review process, we became aware of another work that independently observed the ~285 cm^{-1} peak)[92]. Figure 3.3b and c shows optical images of multi-layered samples on SiO_2 (300 nm)-on-silicon and quartz substrates, respectively, and Figure 3.3d–g show Raman spectra from layers of different thicknesses near these two new peaks from these and similar samples. In samples grown on SiO_2/Si substrates the peak at ~285 cm^{-1} was found to be absent in all monolayer samples, but appeared strongly in samples with more layers (as seen in Figure 3.3d). The origin of this peak can be traced to a the E_{1g} phonons near the Γ-point,[124] and has been previously reported in few-layered WSe_2 samples.[125] According to Scheuschner *et al.*[92] single-layer, few-layer and bulk MoS_2 belong to different point groups, with the E_{1g}, E_g and E' modes in bulk, even layers and odd layers, respectively, all originating from the E'' mode in single-layer MoS_2. The E'' mode requires a scattering geometry with a z-

component to be observable which is difficult to realize in backscattering in the single layer,[116] which is consistent with its absence in 1L sample on SiO_2/Si. When measured on samples grown on quartz, these peaks were difficult to discern from the background level, and required significantly higher data-averaging. Figure 3.3f show the variation of this peak as a function of layer-thickness, where each spectrum shown is an average of 5 spectra measured on different samples. We find, surprisingly, that the peak at ~285 cm^{-1} shows up for *all* layer-thicknesses, including in monolayer samples. Moreover, within our experimental limits, it appears that the averaged peak-height was strongest in monolayer samples. These observations are in stark contrast to the spectral behavior in samples grown on SiO_2. Our data appears to imply that the mono- and few-layer samples interact with quartz in a manner which is different from that with SiO_2, and which enables the realization of the E" mode in the backscattering geometry. Detailed future studies will be required to understand the underlying physics that causes the differences between the layer-thickness-dependence of Raman spectra obtained on samples on these two and possibly other substrates. Interestingly, the position of $E_g^{/}$E'/E" phonon modes in 2D-MoS_2 were found to be resilient against layer-thickening in samples on both substrates, within our experimental resolution of 1 cm^{-1}.

The second newly-observed peak at ~487 cm^{-1} appears to be a combination of transverse acoustic phonons A^2_{2u}(M) near the M-point and the $E_{2u}(M_2)$ phonon near the M point with A_u symmetry. The layer- e (sample on SiO_2 substrate) and Figure 3.3g (sample on quartz substrate). In samples grown on SiO_2/Si, this mode was also found to be absent in monolayer samples. While a very weak peak appears in only some bi-layer samples, it appears strongly in samples of higher number of layers. In contrast, evidence of this mode could be found in even monolayer samples of MoS_2 grown on quartz, with growing peak intensity as the layers thickened. In this case, we were able observe a a blue shift in the

peak position from ~488 cm^{-1} to ~493 cm^{-1} as the layer thickness grew from 1-4. The presence of this new Raman peak in our samples is surprising since it has been predicted[124] to arise only at low temperatures. We note that at this point, the reasons leading to the differences in the layer-thickness variation of this peak in samples grown on different substrates is not clear to us. Nevertheless, at the very least, we believe that our ability to observe these very subtle differences is testament to the high optoelectronic quality of our 2D-MoS_2 crystals.

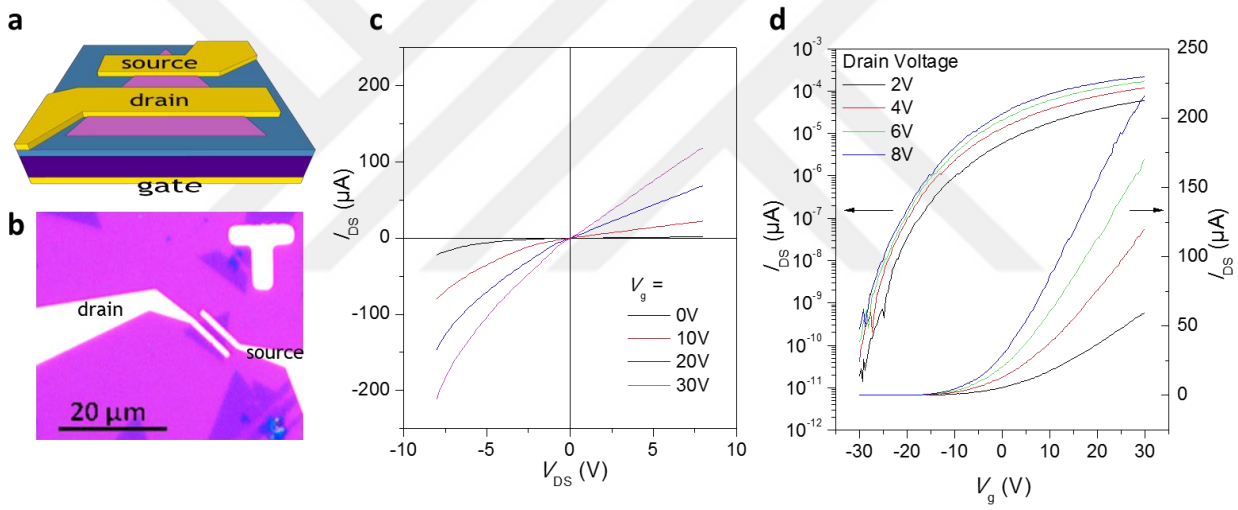

Figure 3.4: (a) Schematic illustration of the single layer MoS_2 field effect transistor platform for electrical and photocurrent measurements. (b) Optical image of the FET device. (c) I_d-V_d curves measured for different gate voltages in the dark. Inset: Ti/Au is used for drain- source electrodes. (d) I_d-V_g curve measured for a bias voltage ranging from 2 V to 8 V. (Data is taken in LANL under supervision of Dr. Mohite).

To measure the gate-modulated electrical and optoelectronic properties of single-layer MoS_2, as-grown samples were transferred onto d=100 nm thick SiO_2/Si substrates (pre-marked to assist lithography) by

using a polymer-assisted transfer method. The schematic of a field-effect transistor device structure is shown Figure 3.4a. Electrical contacts were fabricated with electron-beam lithography followed by the deposition of 5 nm Ti and 50 nm Au using an e-beam evaporator. Figure 3.4b shows the optical image of the actual device on which measurements were performed. In Figure 3.4c I_d-V_d curves are shown for different gate voltages which appear to exhibit low schottky-barrier characteristics. In Figure 3.4d shows the transfer characteristics (I_d-V_g) of the same device measured at different source-drain voltages. Single layer MoS_2 FET devices exhibit a typical n type characteristic with a threshold voltage -10 V, in good agreement with previous reports.[13,109,126] The field-effect mobility of this device was ≈ 35 cm^2/Vs at room temperature for our devices calculated using the equation $\mu=[dI_d/dV_g]\times[L/WC_iV_d]$,[13] where the channel length L=2.4 µm, channel with W=1.4 µm, back gate capacitance per unit area $C_i = \varepsilon_r\varepsilon_0/d$ (ε_r=3.9, d=100 nm) and V_d=10 V. The mobility of our devices are about 2 times higher than those reported for monolayer CVD grown MoS_2 using other precursors[76-79], and comparable to the values of mobilities that are obtained by post annealing the samples.[127,128] The I_{on}/I_{off} ratio obtained for V_d=8 V is ~10^6 for gate voltages in the range of -30 to + 30 V. At the same voltage, the subthreshold swing ($S=dV_g/d(\log I_d)$) ~ 5 V/dec in good agreement with previous results.[129,130] Our preliminary electronic characterizations of these devices demonstrate significant improvement over past reports both for CVD-grown as well as mechanically exfoliated monolayer MoS_2.

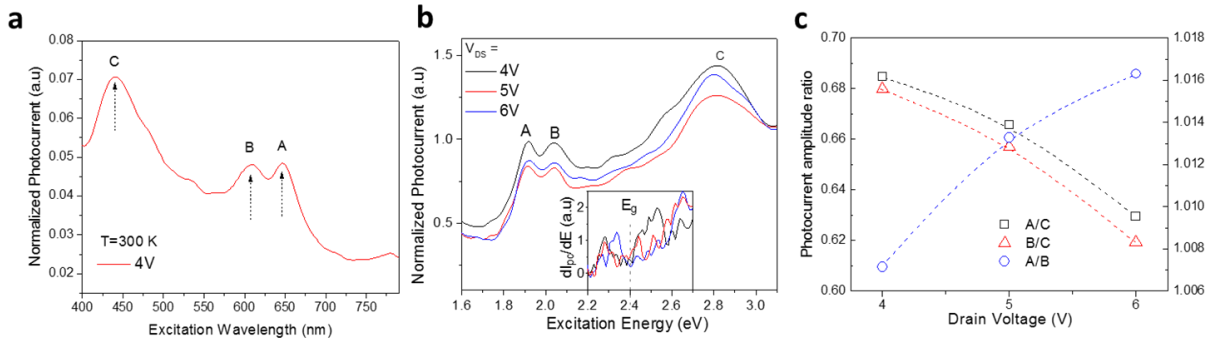

Figure 3.5: Excitonic states in monolayer MoS_2 investigated by photocurrent spectroscopy at room temperature. (a) Excitonic states A, B, and C characterized by the corresponding peaks in the photocurrent spectrum (V_{ds}= 4 V). (b) Bias dependence of photocurrent spectra showing evolution of excitonic peaks (V_g = -42 V). Inset: First derivative of the photocurrent spectra with respect to energy, from which the continuum band gap energy of single layer MoS_2 is ≈ 2.4 eV. (c) Bias dependence of the photocurrent amplitude ratios of the A-, B-, and C- excitonic peaks at room temperature. (Data is taken in LANL under supervision of Dr. Mohite).

Photocurrent spectroscopy was performed on these devices using a broadband white light source coupled to a monochromator allowing us to tune the wavelength of the incident light from 400 nm to 1200 nm continuously. The output from the spectrometer was coupled to a Vis-NIR multimode fiber and focused onto the device, which was mounted in a Janis cryo probe station. The net photocurrent was calculated by taking the difference between the dark current the total output current with illumination. A measurable photocurrent was only observed when a finite bias was applied between the source and the drain electrodes and its value was found to be strongly bias dependent. This observation helps us eliminate the possibility of any photovoltaic contribution from the electrode-MoS_2 junctions. Moreover, the photocurrent is significantly larger (see Figure 3.8) than the dark current at gate voltage less than -

10V, where the channel is undoped and results in a sharp decrease of the latter. Below V_g = -30 V, the channel was assumed to be "intrinsic", and the photocurrent spectra were measured under these intrinsic conditions by scanning the wavelength of incident light and recording DC photocurrent as a function of applied source drain bias and temperature. Figure 3.5a shows the room-temperature photocurrent measured as a function of excitation wavelength for a single layer MoS_2 FET device. The measured photocurrent from the MoS_2 devices was normalized with the incident power at the end of the fiber optic used for photo excitation. The incident power for each wavelength was calibrated using the spectral response (Amp/Watt) of a standard Si photodiode placed at the same distance from the fiber optic as the device. A series of peaks are clearly seen at wavelengths λ=646 nm, =608 nm, and =440 nm (corresponding to photon energy values of 1.92 eV, 2.04 eV and 2.82 eV, respectively) that are labelled as A, B and C respectively. The position of the peaks are in a good agreement with previous experimental reports on absorption spectroscopy[22,97,110], photocurrent spectra on measured on mechanically exfoliated and suspended samples,[41] and light scattering experiments on MoS_2 samples on gold substrate[131]. We attribute the peaks at 1.92 eV and 2.04 eV to the A-and B- excitons as a result of valence band splitting at the K point due to spin-orbit (SO) splitting and the absence of inversion symmetry.[97,132,133] Because of the clear splitting of the two excitonic peaks, it was possible to accurately determine the energy difference of ~120 meV between the position of A and B peaks, which corresponds to the energy due to SO coupling and compares well with absorption measurements reported previously.[97,133] Since A and B are excitonic states, it is expected that the observed excitonic peaks would be electric field dependent. The presence of an external field would aid the dissociation and separation of bound electron-hole pairs thereby increasing the photocurrent efficiency. Indeed, as illustrated in Figure 3.5b there is an overall increase in the magnitude of the photocurrent peaks

corresponding to the A and B excitons. The peak labeled C is associated with van-Hove singularities in the DoS where arises between K and Γ points at the Brilloin Zone[41,110,134] consistent with measurements performed by Klots *et al*. By taking first derivativities of the photocurrent spectra with respect to energy, we could extract the continuum band gap energy value at room temperature $E_g \approx 2.4$ eV, as illustrated in Figure 3.5b inset. This value is consisted with the experimentally calculated single layer MoS_2 devices.[41,135] We further obtain an exciton binding energy of 480 meV by subtracting the band-edge from the position of the excitonic peak A at room temperature ($E_b=E_g-E_A$). Analysis of the photocurrent amplitudes of excitonic states at room temperature indicates an increase in the amplitude ratio of A/B (see Figure 3.5c), which appear to imply that at least at room temperature, the A exciton can dissociate more efficiently than the B exciton and contributes more to the net photocurrent. To our knowledge, such clear and detailed information regarding the excitonic properties using photocurrent spectroscopy has previously not been reported on CVD-grown MoS_2, which we believe is an indication of the high optoelectronic-grade quality of our samples.

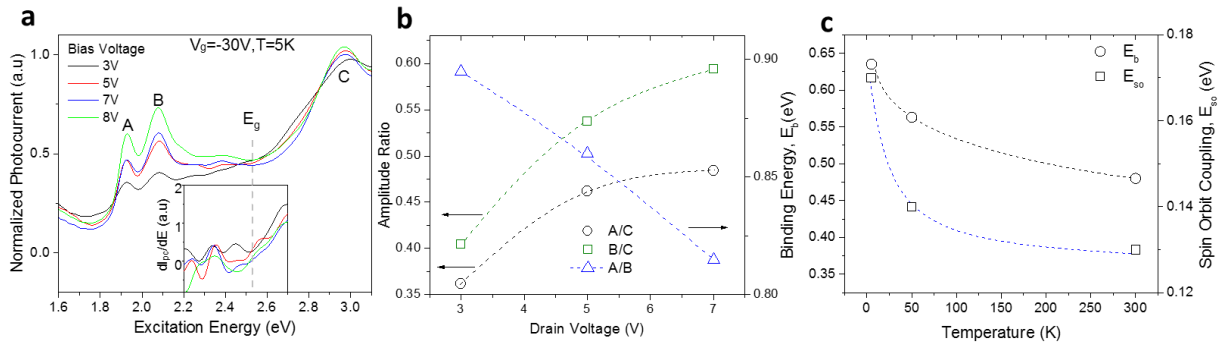

Figure 3.6: Photocurrent spectra of Single layer MoS_2 at low temperature (5 K): (a) PC spectra measured for different bias voltages at Vg=-30 V, 5 K. The inset: Band gap calculation of single layer MoS_2 at low temperature. (b) Relative photocurrent amplitudes of A-, B-, & C- peaks. (c) Binding and spin orbit coupling energies for single layer MoS_2 at different temperatures. (Data is taken in LANL under supervision of Dr. Mohite)

Further information regarding the optoelectronic energetics could be obtained by performing photocurrent spectroscopy at low temperatures. Figure 3.6 shows the photocurrent spectra of the same device measured at 5 K with increasing V_{sd}. It can be clearly inferred that the photocurrent peaks are sharp and much more well-defined as compared to room temperature. The photocurrent of B exciton becomes slightly larger with respect to A state and we also find that the ratio of A/C and B/C increase with increasing drain-source voltage as illustrated in Figure 3.6b. The position of the peaks remains unchanged with bias voltages at 5 K. Figure 3.6c shows the variation in the exciton binding energy and the SO coupling energy spacing with temperature. We observe a decrease in both of these values as we approach RT. These observations are consistent with observations on devices fabricated with exfoliated MoS_2 flakes suspended across a trench.[41] To the best of our knowledge this is the first observation of the

excitonic states in the photocurrent spectrum of CVD grown MoS_2 devices and attribute this to the high optoelectronic quality of our single-crystalline MoS_2 flakes.

3.3 Conclusions

In conclusion, a range of highly crystalline monolayer and few-layered MoS_2 structures can be controllably grown *via* CVD method by using MoO_2 as a source. Using this method, MoS_2 structures can be obtained on a broad variety of substrates that makes it suitable both for fundamental investigations as well as applications development, without the need for any pre-treatment on precursors. While mostly monolayer samples can grow at CVD temperatures ranging from 650 – 850 °C, we did not find any direct correlation between the samples of relatively better quality and synthesis temperature. For the purpose of standardizing, we have selected the middle of this range, *i.e.* 750 °C, at which temperature, adequate surface coverage of single crystal flakes within a reasonable growth duration was obtained. High-resolution TEM resolved images of our samples, when grown substrate-free[118] show extremely high crystalline quality in our samples in comparison to those reported earlier[77,80,82]. In addition to the commonly observed Raman and PL peaks, sensitive information regarding multi-phonon processes could be clearly observed on these samples, including two previously unreported Raman peaks. The field-effect mobility of these samples is notably higher than those measured in samples synthesized using Mo and MoO_3 based precursors. For the first time, we have demonstrated excitonic states in photocurrent spectra at room temperature in CVD-grown samples of MoS_2, which was previously thought to be impossible to demonstrate even in exfoliated samples without suspension. We believe that our observations establish that using MoO_2 as a source leads to high-quality atomically-thin

crystals of MoS_2 samples which is a big step towards fundamental research and application development of the optoelectronic devices.

3.4 Supporting information

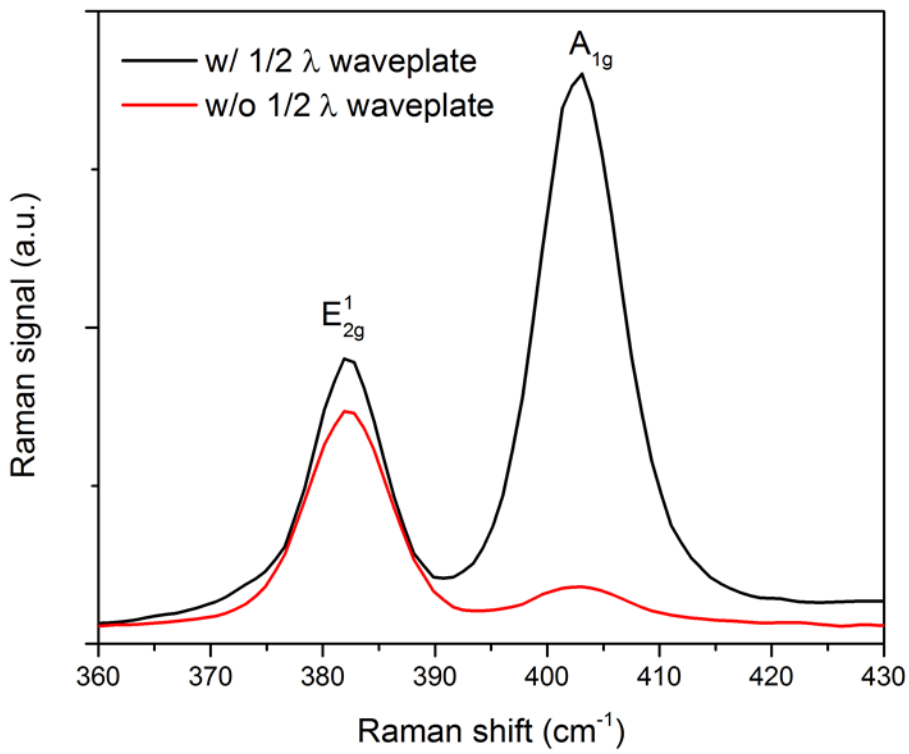

Figure 3.7: The E^1_{2g} and A_{1g} modes have both helicity and linear polarization dependence. In our Raman spectrometer, the incident laser partially linear polarized. Therefore, A_{1g} scattered light has the same polarization as the incident laser. The Raman has an optional $\lambda/2$ waveplate in front the spectrometer. We tested the Raman spectra for both with and without waveplate. The A_{1g} peak shows strong polarization dependence compared to the E^1_{2g} peak which shows weak dependence. This polarization dependence is not related to the sample quality.

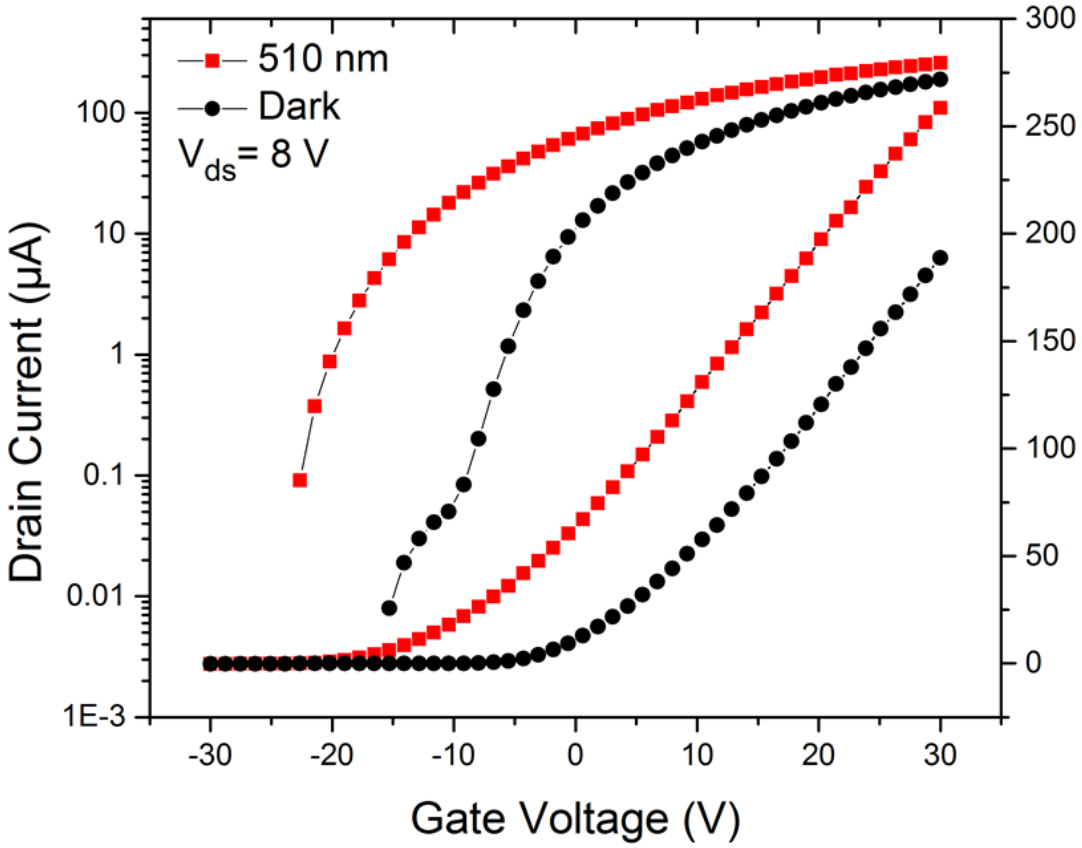

Figure 3.8: Transfer characteristic of the device in dark and under 510 nm light illumination at 8V bias voltage.

Chapter 4: Investigation of Raman Processes in High-Quality Vapor Phase Chalcogenization Grown Atomically Thin Molybdenum Diselenide

4.1 Introduction

Atomically-thin layered (2D) materials such as graphene, transition metal dichalcogenides, and a range of other layered compounds[136] remain one of the most interesting systems for exploring a wide range of novel electronic,[137] excitonic,[138] valley,[43] and correlated[139] physics in two-dimensional (2D) confinement. Since the discovery of monolayer graphene, it has become well-known that charge carriers in 2D materials demonstrate unexpected behavior, including not limited to massless Dirac Fermionic behavior,[4,7] unusual half-integer quantum Hall effect,[6] field-tunable electron-phonon coupling[140] and field-tunable plasmons[141,142] in graphene, and to tuning of valley magnetic moments,[143,144] control of excitons,[145,146] appearance of gate-tunable superconductivity,[139] spin-Hall effects,[147] valley-Hall effects,[148] and tunable many-body physics[149] in 2D materials beyond graphene.[5,150-152] In addition to their fundamental properties, these materials show enormous potentials for transistors[153] and photonic devices,[154] nanoelectronics,[155] optoelectronics,[20] photodetection,[57,156] memory,[157] and energy technologies[158].

Both from fundamental as well as applications perspectives, a key issue of primary importance is the development of high-quality, reproducibly-synthesizable 2D materials. In the past, several approaches have been used to ascertain the quality of 2D materials. At the very limit of the atom, both TEM[159-161] and STM[135,162] have been used as a high-fidelity tool to investigate the defect, impurities, and grain

boundary properties of these materials, as these are expected to have a significant impact on transport and mechanical properties of 2D materials.[163,164] However, such probes are extremely localized to a few-hundred-atoms scale, and it is laborious and experimentally untenable to scan the overall impact of these disorders on the properties of larger-area, microns-scale samples. As a result, carrier mobility measurements have been used as a probe for characterizing the device-level performance of 2D materials,[127,165] since mobility is a direct measure of the impact of various scattering mechanisms within the material. Another technique – *i.e.* Raman spectroscopy, has remained an alternate and highly sensitive probe to investigate both novel physics as well as sample-quality of 2D materials.[166-168]

It has been long established, well before the onset of 2D materials, that Raman spectroscopy is one of the most powerful techniques for characterizing nanomaterials.[169] This technique probes the three major contributors to their electronic properties, *i.e.* carriers, photons, and phonons.[168] In addition, Raman spectroscopy is also highly sensitive to various other aspects that have a strong impact on the electronic and optical properties of 2D materials, such as layer-thickness, substrate-dependence, strain, and defects, to name a few.[167,170,171]

In this work, we report on the development and characterization of high quality 2D-$MoSe_2$, using a vapor-phase deposition (VPD) process. Unlike 2D-MoS_2, which has been extensively investigated for its fundamental properties as well as application potentials, 2D-$MoSe_2$ has received far less attention. In this work, we present a detailed investigation of various Raman active modes in our samples. A range of recent works have revealed a great deal about the vibrational modes that lead to Raman spectroscopic peaks in bulk and 2D-$MoSe_2$. To a large extent, the most detailed structure of Raman spectrum has been reported in either bulk or mechanically-exfoliated samples of $MoSe_2$, since it is widely accepted that

such samples have higher electronic quality. Nam *et al.*, performed detailed Raman spectroscopic investigation bulk commercial $MoSe_2$, documenting and investigating the evolution of the most prominent peaks as a function of excitation energy.[172] Soubelet *et al.* extended this work by investigating layer-thickness dependent and excitation-energy dependent Raman on 2D-$MoSe_2$ obtained from mechanically-exfoliated samples.[173] Similar mechanically-exfoliated samples were used by Chen *et al.* to reveal the effect of optical helicity-dependent Raman scattering in 2D-$MoSe_2$,[174] and by Kioseoglou *et al.*, who investigated intervalley scattering through Raman studies.[175]

In addition, detailed studies of low-energy modes have been performed on chemical vapor deposition (CVD)-grown $MoSe_2$ samples, for example, by O'Brien *et al.*, who measured and mapped these modes[166,176] and by Lu *et al*. who investigated the effect of stacking sequence and polymorphism on Raman spectra[177]. However, their data do not appear to reveal several intermediate- and high-energy fine structures present in the 2D-$MoSe_2$ Raman spectrum. Other reports utilize Raman spectroscopy as a tool to identify/characterize $MoSe_2$ in a number of CVD-synthesis works, including pure phase 2D-$MoSe_2$, and its alloy and heterostructures with 2D-MoS_2,[178-183] by identifying their signature A^1g and E^1_{2g} modes. A survey of these works appears to indicate that some of the detailed fine structures in Raman spectra has so far remained challenging to observe in CVD-grown $MoSe_2$, very likely due to their lower quality compared to the mechanically-exfoliated counterparts. In the field of 2D materials, this reflects an important issue, since development of applications will require low-cost, scalable methods such as CVD to match sample quality that is comparable to that of mechanical exfoliation.

In an earlier work, we had addressed this issue for another 2D material, *i.e.* 2D-MoS_2. Using Raman spectroscopy as a characterization tool, we had demonstrated how high-quality 2D-MoS_2 samples can

be synthesized using an oxygen-reduced vapor-phase deposition (VPD) method. This process, which uses MoO_2 instead of the conventionally-used MoO_3 source, reduces an intermediate growth-step during conventional CVD, and appears to produce samples that have mobility values comparable to that of "mechanically-exfoliated" samples, demonstrate a host of Raman peaks that were previously unreported in CVD-grown samples. We had conjectured that since Raman spectroscopic peaks involve complex *electron-photon-phonon* (including resonance, second-order, and defect-induced) processes, they are far more susceptible to poor sample quality than, for example, mobility measurements (which are mostly confined to near-Fermi level processes, and do not involve photons and higher-order interactions). Hence, we believe that obtaining high-quality fine-structure Raman spectra is perhaps a more powerful tool for ascertaining quality of 2D materials. We had substantiated our claim by showing that our 2D-MoS_2 samples which provided rich vibrational mode information, not only demonstrated high carrier mobility values, but also showed high-quality photocurrent spectra with bias-dependent excitonic features that was previously obtainable only in suspended, annealed mechanically-exfoliated samples.[184]

In this work, we have extended the efficacy of our MoO_2 – based VPD method, to synthesize high-quality 2D-$MoSe_2$ samples. We also present extensive excitation-energy and layer-thickness dependent Raman spectroscopy of these samples that establishes their high quality. In particular, we demonstrate a peak at ~250 cm^{-1} which usually seen in high-quality exfoliated samples, and also show how this peak disappears when our sample ages over time. Raman spectra measured on these samples, in conjunction with first-principles DFT calculations leads us to believe that this peak, whose origin has not been previously discussed, arises from a double resonant Raman process. In addition, we present several

other previously unreported energy- and layer-thickness-dependent features of the 2D-$MoSe_2$ Raman spectra, which provide new insights into their spectral behavior.

4.2 Results and Discussion

Large area high quality single- and few-layer $MoSe_2$ flakes were synthesized using MoO_2 (molybdenum dioxide) and selenium powder in a quartz-tube-in-a-furnace vapor-phased deposition system similar to the one described in our earlier work.[184] Samples were grown in Si/SiO_2 and quartz substrates which were placed face down on an alumina boat that included dry MoO_2 powder at center of the furnace. A second container with selenium powder was placed upstream of the 1-inch quartz tube. Predominantly monolayer samples could be obtained by ramping-up the furnace to 750 °C at a rate of 15 °C/min and maintaining the setup at this temperature there for 20 minutes. During this time, selenium vapor was carried into the chamber using a continuous flow of Argon (200 sccm) mixed with H_2 (around 3 sccm) while maintaining the chamber at ambient atmospheric pressure, which resulted in the sample growth on the substrates. The chamber was then allowed to cool down naturally. During the growth process, samples of various shape/symmetry were obtained depending on the relative concentration of hydrogen gas used. To obtained multilayer $MoSe_2$ samples, the growth temperature was ramped up to 950 °C while maintaining all other conditions identical as those for monolayer growth.

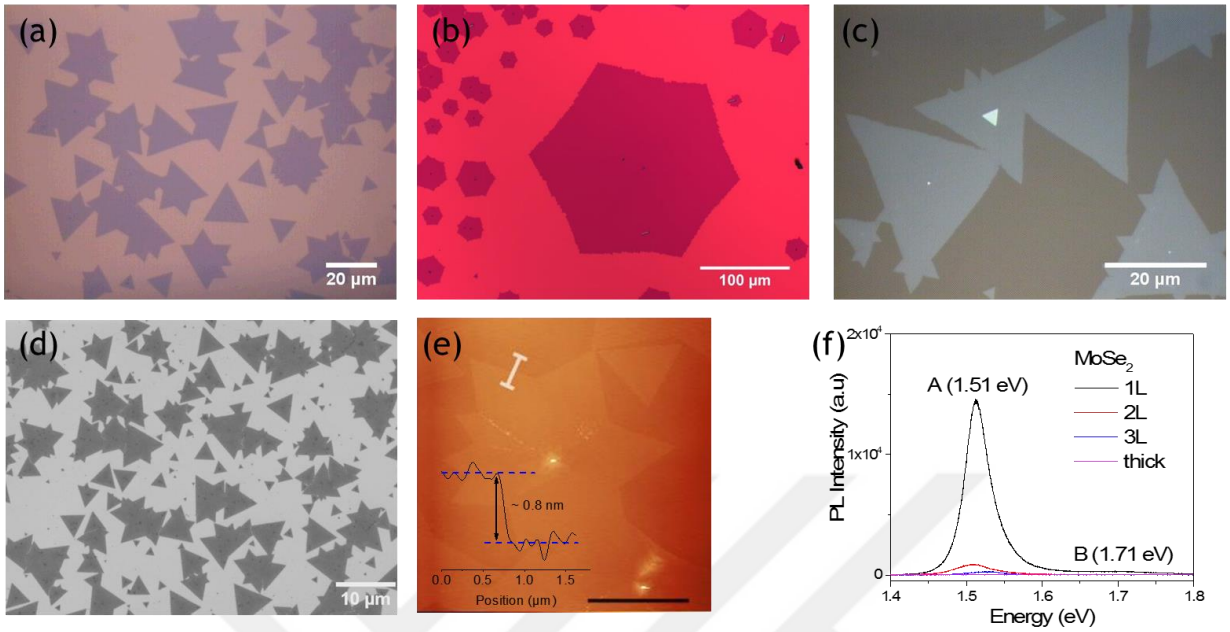

Figure 4.1: Optical images of typical VPD-grown single-layer $MoSe_2$ on (a-b) Si/SiO_2 and (c) quartz substrates, highlighting various sizes and morphologies. (d) Typical SEM image of single layer $MoSe_2$ on Si/SiO_2 substrates. (e) Typical AFM topographical image (scale bar = 5 microns) of a monolayer $MoSe_2$ sample, its thickness ≈0.8 nm determined from the step-height as shown in the the height profile (inset) along the white line in AFM image. (f) Typical Photoluminescence spectrum of single-, few-layered and thick $MoSe_2$ samples. The direct-gap single-layered sample demonstrates the characteristic strong peak at 1.51 eV originating from the A-exciton, and a second shallow feature near 1.71 eV originating from the B-excitons.

Figure 4.1a-b and d show optical and SEM images, respectively, of typical CVD-grown monolayer flakes of $MoSe_2$, a large number of whose edge-lengths varied approximately between 10 microns to 100 microns. Similar samples could also be grown in quartz substrates, as shown in the optical image of Figure 4.1c. The samples mostly had clear geometrical symmetry, indicating their single-crystal nature, although in some cases, polycrystalline samples with merged geometry or with grain boundaries were

also found. The shapes of the flakes were found to be sensitive to the hydrogen concentration during growth, and could be tuned from triangular to hexagonal shapes by increasing hydrogen concentration in Argon (from 1%-4%)) in a manner reported previously for CVD synthesis of 2D-WSe_2.[185] Figure 4.1e depicts an AFM image of Monolayer $MoSe_2$ grown on SiO_2/Si substrate, the measured step height obtained from the (step-height line section shown in white) is about 0.8 nm (Figure 4.1e), which compares well with the previously-reported sample thickness of single-layer $MoSe_2$ [180,181].

Raman spectra of $MoSe_2$ monolayers were measured using a range of different excitation energies (E_{ex} = 1.95 eV, 2.54 eV, and 2.71 eV using a Renishaw (Ramascope), and E_{ex}=2.33 eV using Horiba (Jobin Yvon HR800), in each case, the incident laser was focused to a spot size of ~1 µm using a 100× objective, with the laser power used ~0.4 mW. Monolayer $MoSe_2$ is a direct band-gap semiconductor.[186] Past experiment of ARPES measurements on MBE-grown samples suggest that the band gap of $MoSe_2$ (defined as the energy gap between the conductance band minimum and the valence band maximum, E_{CBM}–E_{VBM}) = 1.58 eV.[37] However, simultaneous measurements of STM tunneling spectrum and optical measurements (Photoluminescence measurements)[187] suggest that the quasiparticle band gap is much higher, between 2.1 – 2.2 eV, while the optical band gap is around 1.6 eV (corresponding to the excitonic A peak), their difference accounted for by its unusually high excitonic binding energy (~0.5 eV) in 2D-$MoSe_2$.[188,189] Hence our excitation energy range covers a range of values from below to above the quasiparticle band gap, near the C-exciton around 2.5 eV[190,191], and beyond.

A number of past works have reported the Raman spectrum of monolayer $MoSe_2$ within 100 cm^{-1} – 700 cm^{-1} range of vibrational frequency (Raman shift) values. A survey of these previous works reveal rich vibrational spectroscopic information in monolayer $MoSe_2$ when measured in mechanically exfoliated

samples.[172,173,192] However, reports of Raman spectra in CVD-grown samples (which are conventionally thought to have poorer electronic and optoelectronic properties) usually reveal the two principle peaks, *i.e.* at A'_1 (Γ) peak approximately 240 cm^{-1}, and the E'_{TO} peak approximately at 285 cm^{-1},[178,180,181] with the other principle, resonant or multi-phonon peaks being either too weak to be detected, or are untraceable in the background luminescence arising from disorder and impurities in the sample. [We note that CVD-grown 2D $MoSe_2$ show clear low-wavenumber (sub – 30 cm-1) peak features which was beyond our instrument limit][176]

Figure 4.2a shows the Raman shift spectra for wavenumbers (ω) ranging from 100 cm^{-1} – 650 cm^{-1} for all four excitation energies, measured in our VPD-grown samples, which clearly demonstrate a range of vibrational peaks that were previously shown to occur in high-quality mechanically-exfoliated samples. As such, the intensity of any peak feature seen here is dependent on a number of parameters, and hence we will refrain from comparing the absolute peak-heights. The data presented has been normalized to the intensity of the silicon ~520 cm^{-1} peak in order to improve visual clarity. In this manner, we are able to compare relative peak-height ratios and spectral positions. We note that even though we use the same incident laser power values, when the silicon peak is normalized, there is an overall increase in the spectral weight at the higher excitation energies, which is consistent with the overall growth of absorption of these samples with increasing photon energies.[173]

There are several important features noticeable in our Raman spectra. Firstly, at all laser excitation values, the well-known A_1' mode for monolayer $MoSe_2$ are observed around ω=240 cm^{-1}. The second signature peak, E'_{TO} was found to vary between ω=282 cm^{-1} – 288 cm^{-1} as the excitation energy was varied, very likely due to a switching from the lower-energy TO mode to the higher energy LO modes

near the Γ-point of the Brillouin zone with changing excitation energy.[172,173] Both the A_1' and E' peaks become more prominent with increasing excitation energy values. This growing spectral prominence with increasing excitation energy can be partially attributed to the growing optical absorbance of $MoSe_2$[190] as the excitation energy increases from 1.95 eV – 2.71 eV. However, the A_1' peak grows

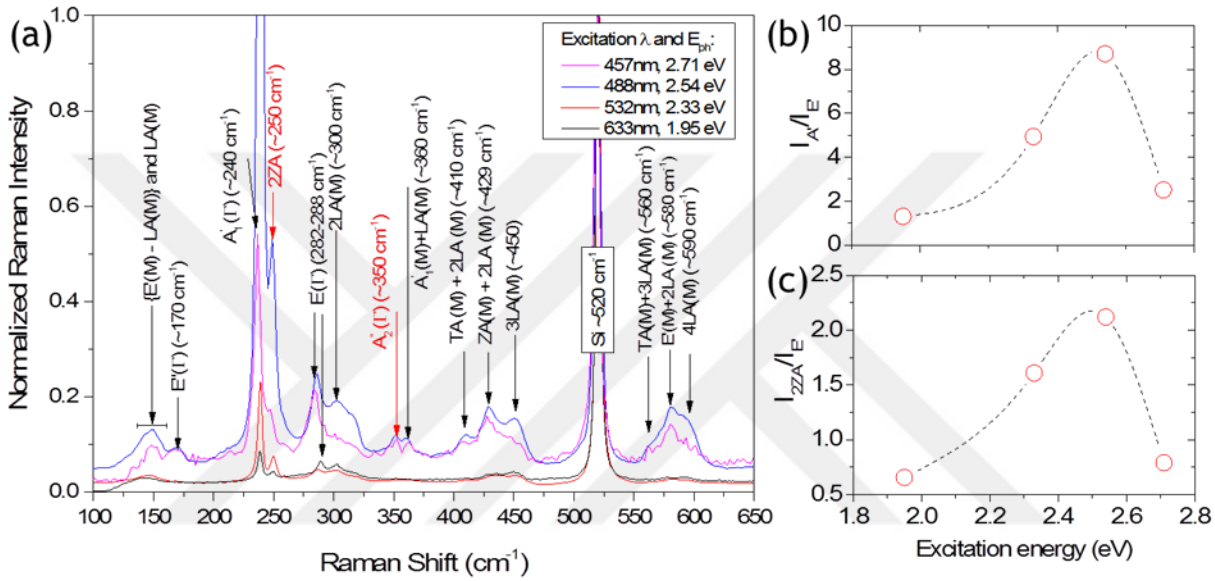

Figure 4.2: Raman spectra of VPD-grown monolayer $MoSe_2$ at different excitation energies: 1.95 eV, 2.33 eV, 2.54 eV and 2.71 eV. The peaks were normalized with respect to the intensity of the Si Peak at 520 cm^{-1}. The various peaks were labelled in terms of the nearest vibrational modes obtained in our theory calculations and matched with previous reports (see text). The peak features are observed to appear or grow more prominent as the excitation energy changes. The most noticeable ones being around 250 cm^{-1}, which we label as the 2ZA peak as discussed in the main text, and the $A_2''(\Gamma)$ peak around 350 cm^{-1}, which is expected to remain absent in monolayer samples. (b) Evolution of the peak intensity ratio of the A' and E' peaks (at ~240 cm^{-1} and ~285 cm^{-1}, respectively), which demonstrates a sharp resonance around energies close to the C-exciton of monolayer $MoSe_2$. (c) A similar resonant feature is observed in the excitation-energy dependence of the peak intensity ratio of the 2ZA and E' peaks (at ~250 cm^{-1} and ~285 cm^{-1}, respectively).

significantly more sharply compared to the E' peak, a feature which has been brought out clearly in Figure 4.2b, which shows the excitation-energy dependence of the intensity ratio of these two peaks. The ratio grows sharply with increasing excitation energy, and then falls dramatically beyond 2.6 eV, thereby demonstrating a resonance-like behavior. Interestingly, the resonance occurs away from the quasiparticle band gap, which is expected to be between 2.1-2.2 eV in monolayer $MoSe_2$, although it is extremely close to the C-exciton ground state of monolayer $MoSe_2$, which is expected to exist between 2.5-2.6 eV.[190,191] We therefore believe that the A' peak couples strongly to the C-excitons in monolayer $MoSe_2$, a fact that is consistent with recent experiments in mechanically-exfoliated samples. We further observe a broad peak centered around 150 cm^{-1}, which we attribute to the overlapping contribution from the longitudinal acoustic phonon mode LA(M) at ω=150 cm^{-1} and the multiphonon process E'–LA(M), around ω=135 cm^{-1}, as indicated in Figure 4.2a. In addition, at the two higher excitation energies, we clearly detect a peak at ω=170cm^{-1}, which we attribute to the E" peak at the Γ-point of the Brillouin zone. At higher vibrational frequencies, we observe the LA(M) overtones, *i.e.* the 2LA(M) peak at ω=303cm^{-1}, the 3LA(M) peak at ω=451cm^{-1}, and the 4LA(M) peak at ω=590cm^{-1}. And finally, we also clearly see peaks at ω=168 cm^{-1} (E''_{TO} (Γ)) and at ω=352 cm^{-1} (A''_2(Γ)). The absence of these peaks have been previously used to identify the presence of monolayer of $MoSe_2$ as they are expected to be forbidden in the backscattering geometry for monolayers.[166,172,175,192] . From Figure 4.2a, we find that these peaks are nearly absent or untraceable for the two lower energy values, whereas they are clearly present at the higher excitation energies. The rest of the peaks are labeled as a combination of optical and acoustical phonons from M point, which is consistent with recently published work on exfoliated $MoSe_2$ samples.[173] We believe that observation of these higher-order and multi-phonon peaks (which

are usually absent in CVD-grown samples) is a testament of the high sample quality obtained despite using a vapor-phase growth process.

In addition to these expected Raman peaks, we observe the clear appearance of a peak at ~250 cm^{-1}, whose origin has not been clearly established earlier. Interestingly, although this peak does not appear in Raman spectra of CVD-grown $MoSe_2$, it does show up in CVD-grown alloy-like and heterostructures of $MoSe_2$ with other 2D materials, giving rise to the conjecture that this peak is possibly related to the formation of $MoSe_2$-MoS_2 alloys.[183] However, we are able to observe a peak at this position very clearly in pure-phase $MoSe_2$, as have Soubelet *et al*. in their mechanically-exfoliated samples, establishing that this peak is intrinsic to $MoSe_2$. Inspection of the vibrational band structure (shown later) reveals no vibrational bands at this energy. However, it is very close to twice the energy of the ZA branch near the M point, and we believe this peak is as a second-order of the ZA, *i.e.* 2ZA, and we label it as accordingly in Figure 4.1a. Figure 4.2c shows the variation of the intensity ratio, $I_{2ZA}/I_{E'}$, as a function of E_{ex}. As with the A' and E' peaks, we find that although both 2ZA and E' peaks grow with E_{ex}, the ratio of their intensity grows sharply, peaks around E_{ex} ~ 2.5 eV, and then drops sharply again. In a manner similar to our observation with the A' peak, we believe that this energy-dependence is a reflection of a resonant behavior around 2.5 eV, suggesting that this peak is also strongly coupled to the C-exciton in $MoSe_2$.

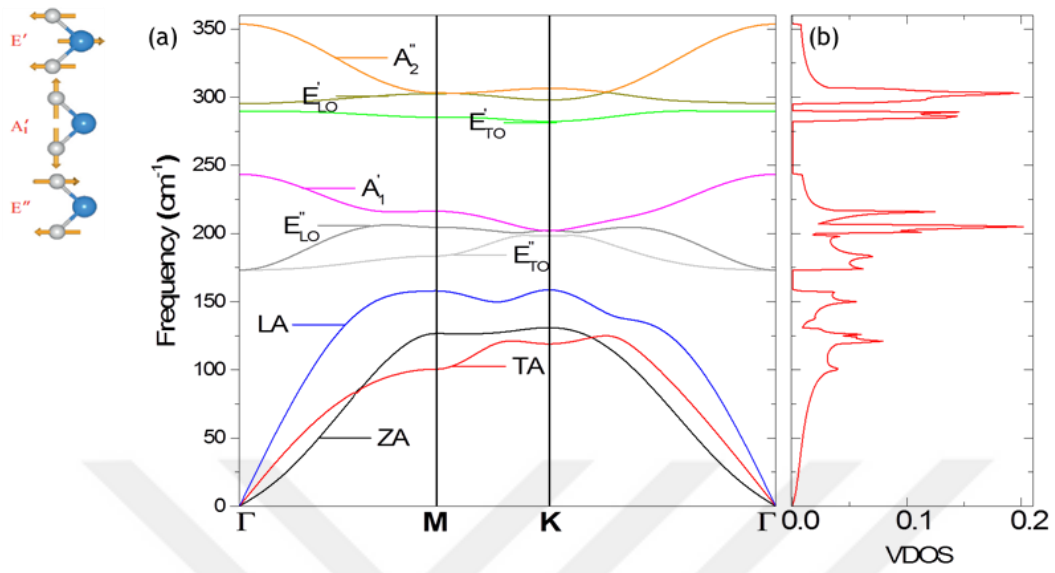

Figure 4.3: Phonon dispersion of monolayer $MoSe_2$ showing the various vibrational bands as labeled. The left inset shows Schematic representation of the principle vibrational modes (b) Calculated vibrational density of states (VDOS) for monolayer $MoSe_2$. (Data provided by Prof. Humberto Terrones/manuscript under preparation)

In order to have a better understanding of the experimental results and in particular for the Raman signal around 250 cm^{-1}, phonon dispersion curves and energy levels of the first excited band of $MoSe_2$ single layers were calculated (by our collaborators, Prof. Humberto Terrones' group at Rensselaer Polytechnic Institute). The phonon frequencies along the high-symmetry line Γ-M-K-Γ and the vibrational density of states (VDOS) were computed by diagonalizing the Interatomic Force Constant (IFC) matrix generated using a 4×4×1 **q**-grid in the Brillouin zone. These methods follow the prescription of the Density Functional Perturbation Theory (DFPT).[193] The electronic band structure and vibrational dispersion of monolayer $MoSe_2$, were obtained by first-principles Density functional theory (DFT)[194] calculations performed using the Quantum-espresso package[195]. We used the Local Density

Approximation[196] of the exchange-correlation functional and norm-conserving pseudopotentials following the Trouiller-Martins scheme[197] to model the interaction between core and valence electrons of Mo and Se atoms. The geometry of $MoSe_2$ was optimized using 9×9×1 Monkhorst-Pack grid[198] to sample the Brillouin Zone(BZ) and the equilibrium condition was imposed using a force threshold of 0.0025 eV/Å (10^{-4} Ry/bohr ~ 10^{-3}Ha/Å). These parameters have shown to yield satisfactory convergence of the total energy. The lattice parameter of the ground state of the monolayer $MoSe_2$ we obtained was a=3.28 Å and the out-of-plane dimension was set at c=24.65 Å. Energy convergence tests have also been carried out regarding c and the vacuum distance of 24.65 Å satisfactorily limit the inter-layer interaction. LDA is known to yield a lower band gap than experimentally observed; hence the electronic band structure was corrected using a rigid shift of the excited states with a scissor operator to the optical band-gap value of 1.61 eV[187].

Figure 4.3 shows the calculated vibrational band structure and density of states in monolayer $MoSe_2$. From Figure 4.3a it can be noted that there are no phonon modes crossing the 250 cm^{-1} at gamma, meaning that the 250 cm^{-1} peak is likely to be a second-order Raman mode, possibly resulting from a double resonance process involving the acoustic mode (ZA) ωZA(q)~125 cm^{-1}, at the M-point, K-point or at several q-points along the M-K line. The possible double scattering involving ω(q)and ω(-q) amounts to doubling the frequency ω(q). The vibrational density of states (Figure 4.3b) around 125 cm^{-1} confirms the presence of several phonons with frequencies 125 cm^{-1} that can play a role in the double resonance process.

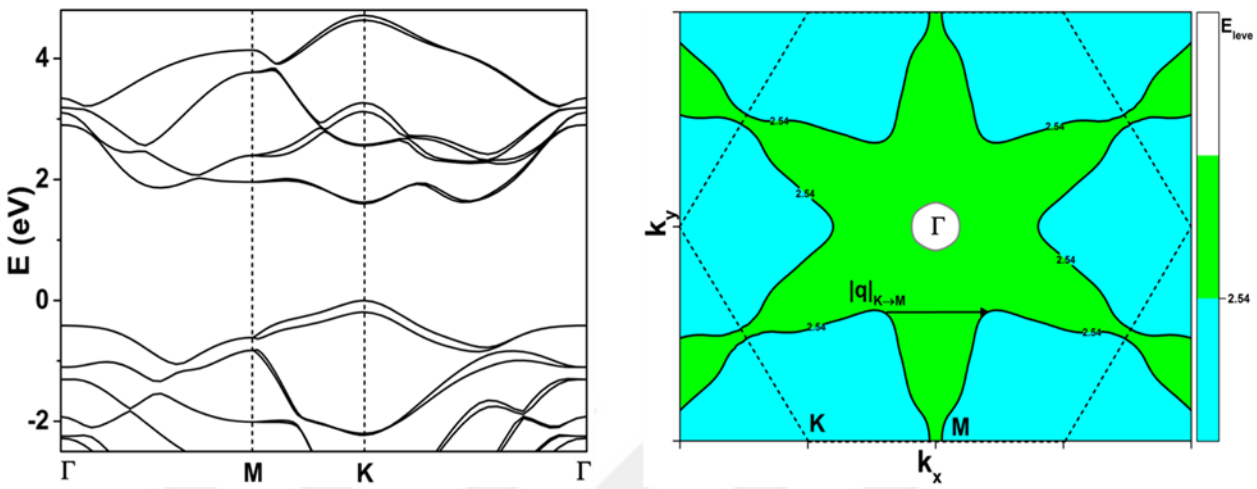

Figure 4.4: (a)Electronic band structure of monolayer calculated using ab-initio density functional theory. (b) Contour plot of the energy levels of the first excited band. The contour lines correspond to a region with the same energy in the first Brillouin zone (delimited by the dashed line). The black lines correspond to electron energy level of ~2.54 eV and the black arrow represent a wave-vectors of phonon that can scatter the electron to another isoenergy. ~2.54 eV (resp. 2.33 eV) contour line. (Data provided by Prof. Humberto Terrones/manuscript under preparation)

Figure 4.4a shows the electronic band structure of monolayer $MoSe_2$ along the high symmetry line Γ −M−K−Γ and Figure 7b shows the region of the Brillouin zone where the electronic energy level is the same. In the double resonance process, we can picture that the carriers, which were created after the initial excitation, are scattered by phonons $\omega_{\mathbf{q}}^{\nu}$ of wave vector **q**, irreducible representation υ, and can only transition to the black contour lines of Figure 4.4b (if symmetry permits) while conserving momentum $\Delta\mathbf{k} - \mathbf{q} = \mathbf{0}$. These carriers at the location **k+**q of the Brillouin zone can be brought back to **k** back by a phonon $\omega_{-\mathbf{q}}$.

Moreover, the isoenergy contour reveals that at the excitation excitation energies (2.54 eV) there are various q-vectors that can scatter the carriers from one valley to another ($\mathbf{q}_{K\to K'}$) or intravalley phonons with wave vector $\alpha\mathbf{q}_{K\to M}$, where $\alpha < 1$. The presence of such q-vectors means that phonons along the M-K line where the ZA branch is flat are likely involved in the process. These theoretical results are consistent with the experimental data obtained from Soubelet et. al..[173]

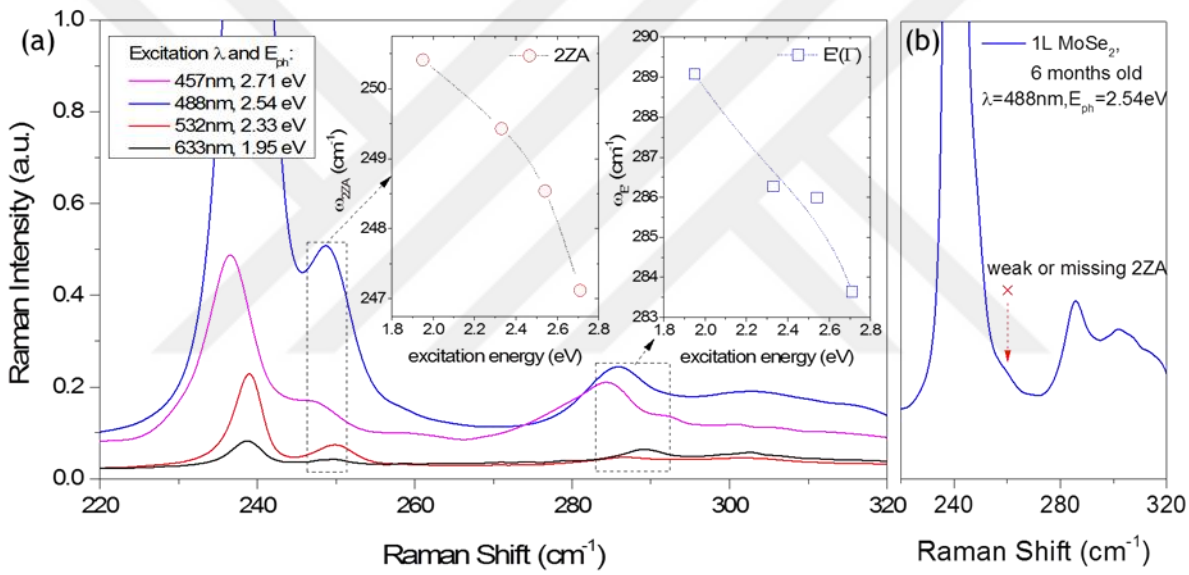

Figure 4.5: (a) Magnified Raman spectra of monolayer $MoSe_2$ to showing the evolution of the 2ZA and E' peaks with different excitation energies. Insets: highlight the variation of their positions as a function of excitation energies. (b) Raman spectrum of a sample measure after six months of synthesis, where the 2ZA peak seems to weaken or disappear completely.

It is expected that certain Raman-active phonon bands will have measurable dispersions in the ω–q plane of the band structure, which will show a variation of positions as a function of laser energy. In our case, the phonon modes were found to be quite stiff, and small but systematic variations could be found

in some of the modes. Figure 4.5a shows a magnified version of the Raman spectra between ω = 220 cm^{-1}–320 cm^{-1}, highlighting the excitation-energy-dependent evolution of the positions of the 2ZA and E' peaks. The insets of this figure show the evolution of the position 2ZA and E' peaks as a function of the energy excitation. It can be observed that both the 2ZA and E' peaks red-shifts to lower frequencies as the excitation energy increases. Very interestingly, the 2ZA peak becomes indiscernibly weak in samples which remain stored for some time. Figure 4.5b shows the Raman spectrum of a monolayer sample that was stored for six months. The arrow marks the region where the 2ZA-peak should appear, where only a very weak feature is seen, in comparison to that seen in Figure 4.5a, which was taken from a freshly-prepared sample. Since it is well-known that ageing has a distinctly deleterious impact on these 2D materials, one could argue that the 2ZA peak is a very sensitive signature of the sample quality. This can well be the reason why often the 2ZA peak is not seen in conventional CVD-grown samples.[180]

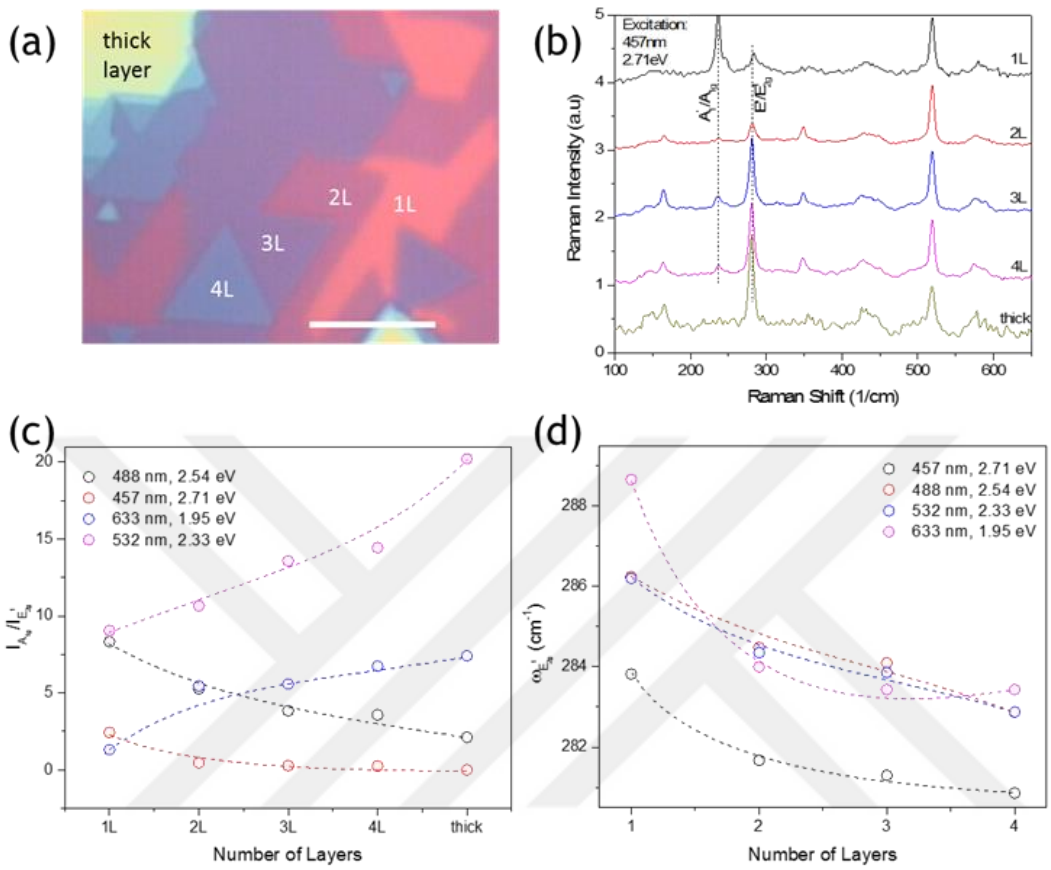

Figure 4.6: (a)Optical image of a typical $MoSe_2$ sample with multiple layers, in which layer-thickness dependent Raman (and photoluminescence, Figure 4.1f) spectra were investigated (scale bar = 10 µm). (b) Typical layer-thickness-dependendent Raman spectra of $MoSe_2$, shown here for an excitation energy of 2.71 eV. The spectra were normalized with respect to the silicon 520 cm^{-1} peak, and then shifted vertically for clarity. The relative intensity of the A' and E' peaks change with layer thickness, as does the position of the E' peak. (c) Variation of the intensity ratio between the A'_1/A_{1g} and the E'/E^1_{2g} peaks as a function of layer-thickness, shown for four different excitation energy values. (d) Variation of the E'/E^1_{2g} peak position as a function of layer thickness, shown for four different excitation energy values.

Finally, we present Raman spectroscopic data of our VPD-grown $MoSe_2$ as a function of sample layer-thickness. The determination of layer-thickness is vital in atomically-thin TMDs, as changing the number of layers from one to few, or from odd to even result in remarkable changes in electronic, optical, and spin-dependent properties. For example, as the layer-thickness is increased beyond 1, 2D-MoSe2 becomes an indirect band-gap system with strongly suppressed photoluminescence, as shown in Figure 4.1f. The crystallographic symmetry undergoes a systematic alternation between odd and even layers, as these layers alternate between centrosymmetric (even layers) to non-centrosymmetric (odd-layered) crystals. Recent work has shown that such symmetry-inversions play a strong role in determining the strength of valley-Hall effect in 2D transition metal dichalcogenides.[143,148] While the layer-thickness dependent studies have been performed extensively for 2D MoS_2, a similar investigation on the few-layered 2D-$MoSe_2$ system has been only recently reported, in mechanically exfoliated samples. Here, we present layer-thickness-dependent investigation of Raman spectra in our VPD-grown samples, and show that not only are the intricate Raman features retained in our high-quality samples, but also present previously un-reported approaches for discerning layer-thickness values of atomically-thin $MoSe_2$ samples. Figure 4.6a shows an optical image of a typical $MoSe_2$ sample where VPD growth leads to multi-layered regions within the same sample, with the layer-thickness values are identified as labeled. Raman spectra were measured using all four excitation energies as before on several areas within an identified layer-thickness region. Figure 4.6b shows the layer-thickness dependent Raman spectra measured using E_{ex} = 2.71 eV (λ_{ex} = 457 nm). The overall spectral intensities were found to vary substantially with layer thickness values, and hence, we normalized each spectrum with respect to the peak height of the Si 520 cm^{-1} peak, and then shifted them vertically to enhance visual clarity. The well-known A_1' and E' modes for monolayer $MoSe_2$ are observed at 240 cm^{-1} and 286 cm^{-1} respectively. (We

use E_g and A_{1g} notations for bilayer $MoSe_2$ since single, bilayer (even numbers) and bulks belong to different point groups D_{3h}, D_{3d}, D_{6h}). We find that there is the sharp decrease in the A_1'/A_{1g} peak intensity and increase in E'/E_{2g}^1 peak intensity as the layer-thickness grows. In addition, while the A_1'/A_{1g} peak demonstrated no change in position with increasing number of layers, the E'/E_{2g}^1 peak position decreases systematically as the numbers of layers increases. These two variations are clearly brought out in Figure 4.6c-d. Figure 4.6c presents the variation of the intensity ratio of the peaks A'/A_{1g} and E'/E_{2g}^1 with layer-thickness, shown for four different excitation energy values. For both excitations, the peak-intensity-ratio decreases with increasing layer-thickness values. Very interestingly, however, the change is substantially sharper for E_x=2.54 eV which resonates very closely with the C-exciton in $MoSe_2$.[190,191] We attribute this to the sharper resonance of the A' mode with the C-exciton in the monolayer sample compared to those present in the thicker layers. The variation of intensity ratios of signature peaks has often been used in the past for other 2D materials such as graphene, providing a way to correlate the number of layers. However, to the best of our knowledge, such a relationship as shown in Figure 4.6c has never been reported for 2D $MoSe_2$. Figure 6d shows the variation of E'/E_{2g}^1 peak position as a function of incident laser excitation. We find a clear red-shift of this peak to lower frequencies as the number of layers increases. This is possibly due to the sensitivity of the in-plane vibrational modes to the presence of additional layers, mediated through van der Waals interactions. This decrease in the E'/E_{2g}^1 peak position provides an additional method for discerning various layer-thicknesses in atomically-thin $MoSe_2$.

4.3 Conclusions

In summary, we have synthesized high crystal quality of $MoSe_2$ samples both on Si/SiO_2 and quartz substrate. Detailed study of Raman spectra in CVD grown mono and few layered $MoSe_2$ samples on different substrates has been presented. We theoretically, for the first time, show that the peak at 250 cm^{-1} for MoSe2 is related to double resonant process of acoustic mode (ZA). We have also shown that Raman spectra of monolayer $MoSe_2$ significantly changes with laser excitation energy.

Chapter 5: Heterostructures of 2D Materials-Synthesis and Properties

5.1 Semiconductor Heterostructures

Since its early days, some of the biggest scientific and engineering developments in the field of semiconductor physics have been enabled by the fabrication of composite structures of differently-doped or dissimilar semiconductors with well-defined, stable interfaces. Such composite systems, whose electronic and optical properties were often determined by the physics at and near the interface (the heterojunctions) are broadly classified as semiconductor heterostructures. Indeed, the physics of heterojunctions has led to an array of fundamental and applied sciences. Depending on the nature (direct or indirect) and size (the energy difference between the conduction band minimum and valence band maximum) of the band gaps, doping levels, position of the Fermi levels, and other factors, semiconductor junctions have been utilized successfully to develop an array of electronic systems such as diodes, bipolar junction transistors, field effect transistors, photodetectors, light emitting diodes, and photovoltaic cells, photocatalysis and photoelectrocatalysis. Generations of scientists have revealed mesoscopic physics and related effects in heterostructures quantum wells and other 2D electron and hole gases. The concept of junctions between dissimilar material have also been extended to other types of systems, such as metal-semiconductor junctions (e.g. Schottky barrier junctions), normal and superconducting metal junctions (e.g. Josephson junctions), junctions between ceramics and other materials, to name a few. Complex junction architectures are instrumental in developing advanced architecture such as the quantum cascade laser and Tunneling Field effect transistors, and an array of sensors, detectors and other advanced electronic and optoelectronic systems.

5.2 Heterostructures in 2D materials

Considering their atomically-thin structures, 2D materials are extremely attractive for the development of both in-plane and vertically-stacked heterostructures. In-plane heterojunctions can be considered to have a 1D interface (see Figure 5.1a), and while vertically stacked structures are expected to develop a 2D interface (see Figure 5.1b), and each of these interfaces are expected to provide an array of important new electronic and optical behaviors.

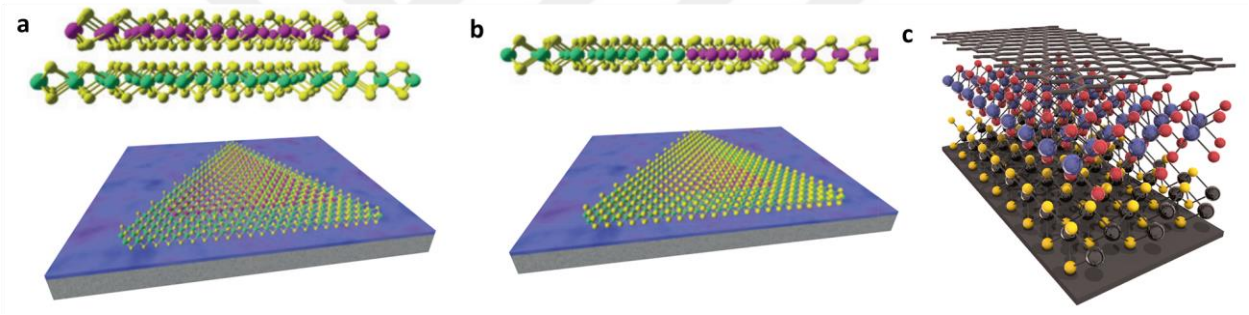

Figure 5.1: Schematic representation of (a) Vertically stacked and (b) In-plane architectures of 2D materials. (c) Schematic representation of a vertical stack of multiple 2D materials, constituting of what is known as a "van der Waals heterostructure".(Image a-b reproduced from ref.[199]; image c reproduced from ref.[200], Image credit: Gabriel Constantinescu)

In addition, the vertical stacking of dissimilar 2D materials can enable completely new 3D architecture-artificial solids that are formed by vertical stacking of 2D materials in any preferred order. These club-sandwich like stacked structures, which were initially conceived by step by step mechanical transfer

various layers top each other, are historically referred to as van der waals (vdW) heterostructures, due to the weak vdW coupling between each layers.

Vertical stacking is widely viewed as a promising approach for designing advanced functionalities using two-dimensional (2D) materials. Combining crystallographically commensurate materials in such 2D-stacks has been shown to result in rich new electronic structure, magnetotransport, and optical properties. Appropriate stacking of two such crystallographically similar or commensurate 2D layers has been shown to result in exotic charge and spin states due to lattice-matching, long-range inter-layer coupling, strain, or formation of Moiré bands. For example, vertically stacked rotationally twisted graphene enables the coexistence of massive and massless Dirac fermions[201], appearance of Moire bands[202], a novel strain-induced evolution of electronic band structures[203], and appearance of van Hove singularities[204]. Similarly, other groups have reported on the observation of Hofstadter butterfly, cloning of Dirac Fermions, and fractal quantum Hall effect in various heterostructures.[205-207] Others have shown that it is possible to obtain tunable direct band gaps in heterostructures of various metal sulfides and selenides[38], and other functional applications[65,66,208]. Recent progress in direct synthesis of various stacked layers of similar and dissimilar crystals with atomically-clean interfaces using chemical vapor deposition (CVD) growth[66-70,209-211] has opened up the possibility for exploring functional synergy in heterostructures of 2D-crystals pairs. Indeed, this field has taken off rapidly with a number of very high-impact reviews that have summarized the synthesis, physics, and potential applications of this field.[9,62-64,212]

5.3 Heterostructures Atomically-Thin MoS_2 and $MoSe_2$

Our newly-developed procedure for growing atomically-thin 2D materials using a vapor phase technique, we have been able to successfully synthesize in-plane and vertically-stacked heterostructures of two distinct TMDs – i.e. MoS_2 and $MoSe_2$.

We have synthesized high-quality heterostructures of the $MoS_2/MoSe_2$ system using a two-step VPD process. The heterostructure growth is based on a two-step CVD process similar to those of the individual 2D materials growth. Briefly, first MoS_2 crystals are grown using the same parameters described above, then as grown $MoS_2/SiO_2/Si$ substrate is transferred to another CVD set up dedicated $MoSe_2$ growth, here the MoS_2 crystals act as nucleation islands for $MoSe_2$ where the $MoSe_2$-MoS_2 junctions are formed (Figure 5.2 a and b). It is worth mentioning that the heterostructure formation can be also obtained in a reverse way by performing $MoSe_2$ growth first and then MoS_2, showing a great potential in the design of junctions using this methodology.

Figure 5.2 shows a typical two-dimensional heterostructures, where MoS_2 was first grown followed by $MoSe_2$. These samples were grown in SiO_2/Si substrates (oxide thickness of 300 nm). It should be noted that in the CVD furnace, the morphology of typical samples varied a lot, as the growth of these crystals was quite sensitive to the various CVD growth parameters. As a result, samples presented in this chapter reflect selected types for investigating specific heterostructures geometries. Figure 5.2a shows an optical image where the first growth resulted in triangular bilayer MoS_2 samples, with the 2-layered region being smaller in size. The growth of $MoSe_2$ in this case appeared to be preferred along the outer edge of the monolayer MoS_2 region. The three regions labelled appeared to reflect different colors under the

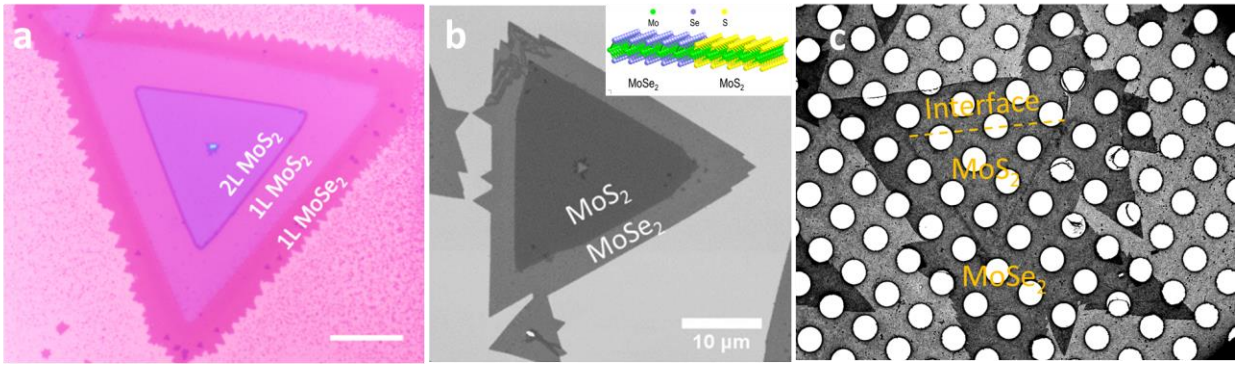

Figure 5.2: Synthesis of lateral hetero structure of $MoSe_2$-MoS_2. Optical (a) and SEM (b) images of CVD grown $MoSe_2$/MoS_2 heterostructure on Si/SiO_2 substrate. (Inset) schematic illustration of heterojunction between two different atomically thin materials ($MoSe_2$-MoS_2). (c) Low-resolution transmission electron microscope (TEM) image of a heterojunctions on a typical copper TEM grid with 2 microns holes. The brightness/contrast of this image has been significantly modified to enhance visibility of the crystals and the junction area. The inner triangular region is MoS_2, whereas the outer region is $MoSe_2$.

broadband illumination of our optical microscope, partially due to their differences in thickness, and also due to their different electronic properties. Although not shown here (but discussed in detail later on), Raman spectroscopy (and Raman mapping) can be used to determine the exact regions over which each type of material extends.

Figure 5.2b shows a scanning electron microscope (SEM) image of mostly monolayer MoS_2-$MoSe_2$ heterostructures. The two regions (MoS_2 and $MoSe_2$) can be distinguished by the different contrast of the secondary electrons they emit, which is once again related to the differences in their electronic properties. We also notice that the boundaries between and at the edges of each type of crystal is not perfectly straight. Detailed investigations with various samples with different growth time reveal that

the outer layer (in this case $MoSe_2$) can grow by partially sacrificing the inner layer, possibly because the edges are very reactive at the growth temperatures. As a result, the interface is not always smooth, and sometimes reveal partial overlaps as discussed later on. Figure 5.2c shows a low-resolution TEM image of a heterojunction sample mounted on a TEM grid. TEM investigations gave us an opportunity to obtain more information regarding the nature of these structure, and how their lattices are arranged.

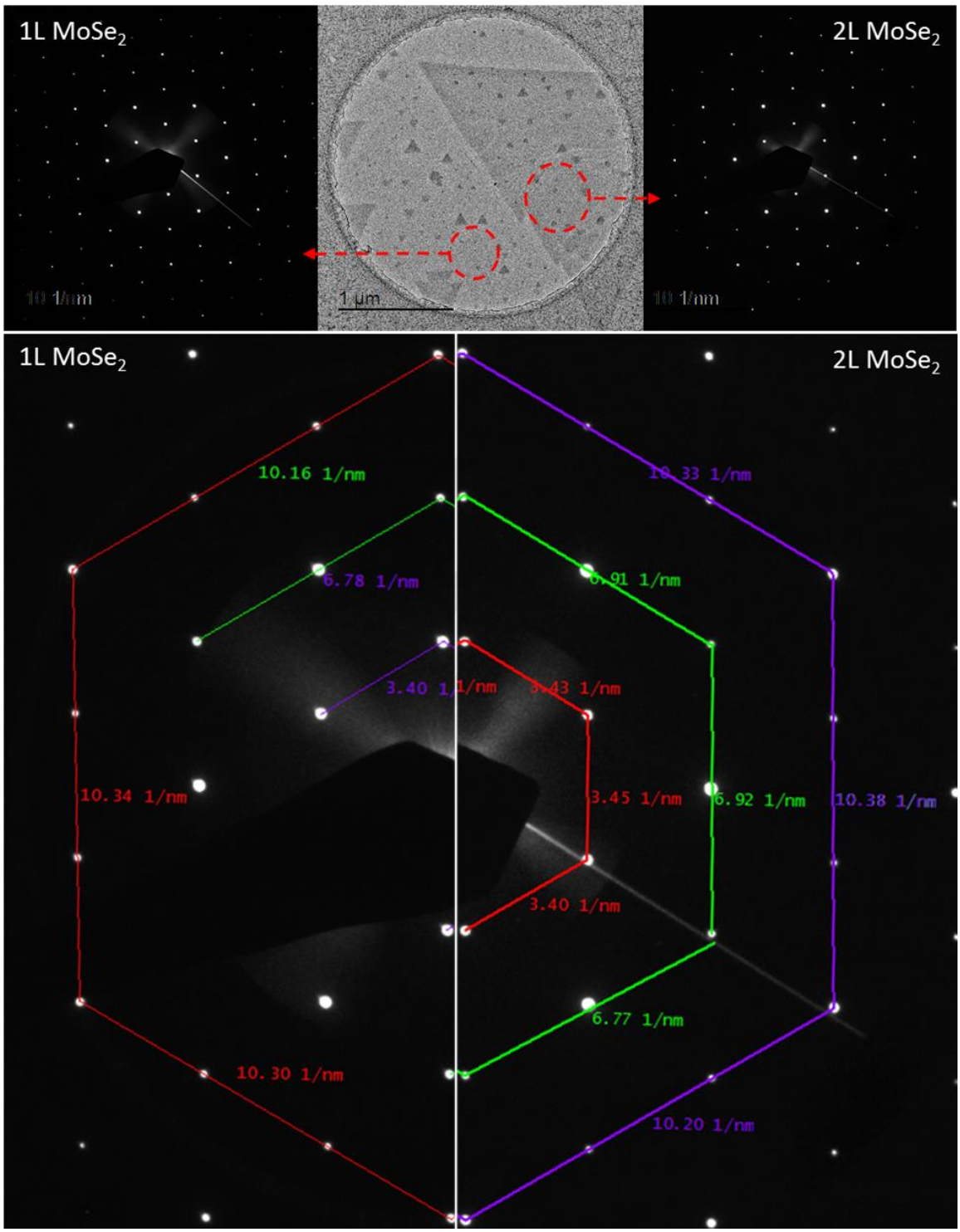

Figure 5.3: Comparative TEM SAED pattern of monolayer and bilayer $MoSe_2$.

Figure 5.3 outlines the result of selected area diffraction patterns obtained from pure $MoSe_2$ samples (both monolayer and bilayer regions) mounted in the TEM. Figure 5.3, middle image shows the close-up TEM image of a monolayer $MoSe_2$ sample that spans a hole in the TEM grid, with partial coverage of second-layer $MoSe_2$ growth in some regions. It is important to analyze these samples so as to clearly distinguish them from other regions of samples where the second layer could be the second 2D material, e.g. $MoSe_2$ crystals on MoS_2, as shown in Figure 5.4. Both the TEM image and diffraction patterns reveal relatively defect-free high-quality single-crystal growth of these samples using our vapor-phase chalcogenization technique. SAED patterns from both monolayer and bilayer regions show very distinct, sharply-focused diffraction spots, establishing the epitaxial growth of the second layer on the first. The lower panel of figure three shows the superposition of split-SAED diffraction patterns from the monolayer and bilayer regions, with the spot-to-spot distances annotated. There was no distinguishable difference in the pattern positions even at the third order diffraction spots, as outlined by the colored hexagons. This is highlighted in order to very clearly establish that the SAED pattern distances (and hence lattice parameters) in monolayer and bilayer samples are nearly indistinguishable, and we estimate that the $MoSe_2$ lattice spacing is 0.29 nanometers, with the primitive cell lattice parameter a = 0.335 nanometers.

In contrast, when the second layer grows as a heterostructures, the SAED diffraction patterns clearly reveal the individual crystals. Figure 5.4a shows the close-up TEM image of a heterostructures region, where the $MoSe_2$ was grown on top of the MoS_2 crystal. The diffraction patterns shown in figures 4 b and 4c corresponds to those taken from a pure MoS_2 and a heterostructures region, respectively. We

find the remarkable result that despite their different lattice parameters (as outlined by the clear separation of the diffraction spots arising from MoS_2 and $MoSe_2$, Figure 5.4c), these two crystals grow with perfect rotational alignment, similar to epitaxial growth. Figure 5.4d-f, which present other examples of heterostructures and their SAED diffraction spots, respectively, show that this occurs over the entire sample region tested, and is not an accidental event. Analysis of lattice parameters from such samples have been summarize in the included table, from which we conclude that the lattice parameter of $MoSe_2$ is over 3.5% larger than that of MoS_2. It was concluded that despite their large lattice-parameter difference, the two crystals could grow rotationally aligned through a van der Waals epitaxy process, a phenomenon that has been used earlier in conventional bulk semiconductors, but only very rarely shown to occur in atomically-thin materials.

Figure 5.5 shows analysis of the cross-sectional topology of in-plane heterostructures, in which MoS_2 was grown first and then followed by $MoSe_2$. Figure 5.5a shows an AFM topography image of the heterostructures, and the arrows (green, blue and red) denote cross-sectional step height being ascertained across three distinctly different topographical features. Coming in from the substrate, the sample shows a step-height of about 0.7 nm, which is approximately the height of monolayered TMDs when measured using an AFM. Going from inside (MoS_2) towards out ($MoSe_2$), the second cross-sectional line (blue arrow) shows a net drop of about 0.9 nm, as shown in the middle cross-sectional panel next to the AFM image. The third cross-section, taken from outside in but within the $MoSe_2$ – MoS_2 intersection region, shows a step jump of about 0.5 nm. This sample likely has a two-layered inner structure and a single-layered MoS_2 intermediate region, before the $MoSe_2$ crystal grows outward.

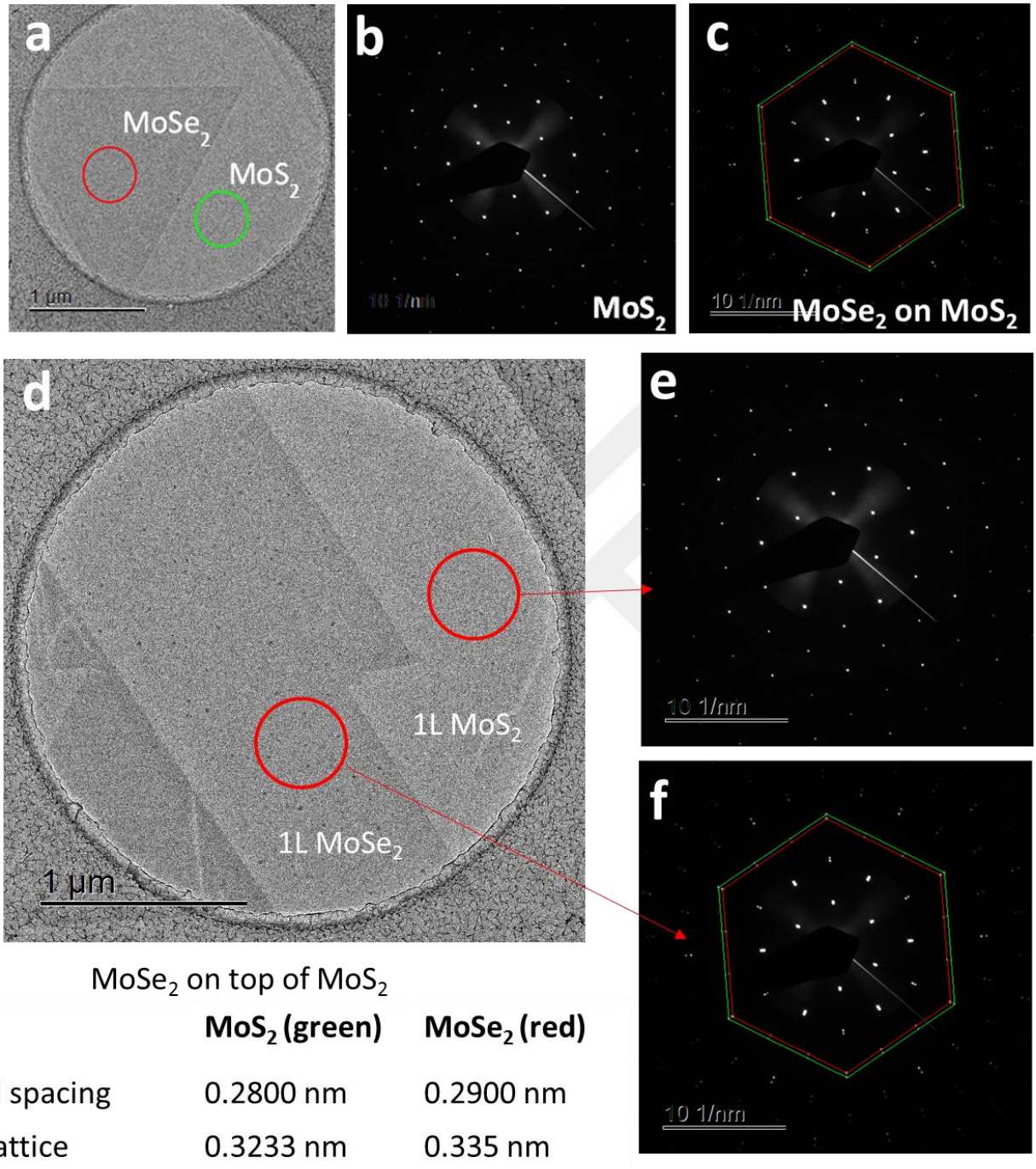

$MoSe_2$ on top of MoS_2

	MoS_2 (green)	**$MoSe_2$ (red)**
d spacing	0.2800 nm	0.2900 nm
lattice	0.3233 nm	0.335 nm

Figure 5.4: Comparative TEM SAED pattern of monolayer MoS_2 and MoS_2/$MoSe_2$ heterostructure regions.

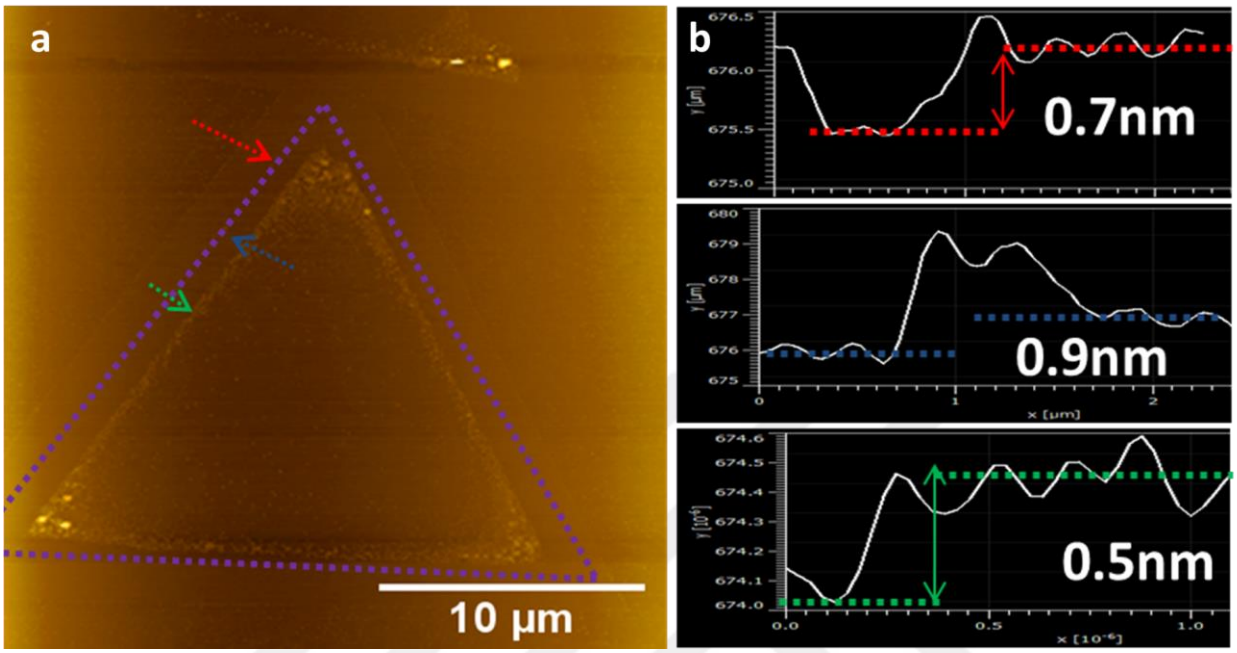

Figure 5.5: a) AFM image and height profile of CVD-grown $MoSe_2/MoS_2$ heterostructure. (b) Schematic representation of cross lines on afm image (red, blue and green lines). (Data is taken by Dr. Andres de Luna Bugallo)

5.4 Raman Spectroscopy of Vertically -Stacked Heterostructures.

As discussed in chapters 3 and 4, transition metal dichalcogenides, due to their crystal structure and symmetry, are characterized by a number of phonon active modes. The presence of these peaks provides an excellent method for determining the type of 2D material – for example, if a sample being probed is MoS_2, MSe_2, or a heterostructures of the two.

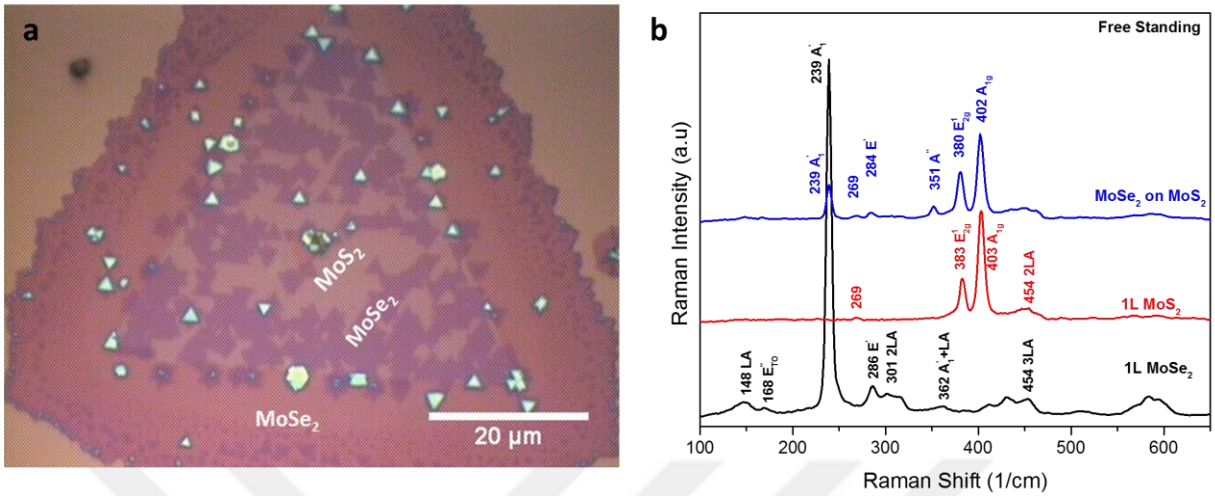

Figure 5.6 a) Optical image of a sample which has different sample morphologies in different locations. Such samples are used to elucidate the role of Raman spectroscopy in distinguishing the presence of pure crystalline regions from heterostructure regions. b) Raman spectra on suspended MoS_2-$MoSe_2$ heterostructure including individual and stacked layers.

Figure 6 shows an example of how Raman spectroscopy can be utilized as a tool to distinguish sample types and morphologies in a crystal that has multiple regions. Figure 5.6a shows the optical image of a sample which has pure MoS_2, pure $MoSe_2$, and heterostructures regions. Such samples were transferred onto holes on TEM grids to obtain a suspended configuration, in order to remove any influence of substrates on them. Figure 5.6b shows the Raman spectra (measured using an incident laser of energy 2.54 eV) from representative areas that are easily discernible by the spectral peaks, as labeled in the figure. It is very interesting to note that certain peaks that are clearly observable in the single-phase regions, get diminished in the heterostructures regions, whereas other peaks appear to or become stronger in the heterostructures. It was seen that the position of $MoSe_2$ Raman peaks does not change much when measured on free-standing 1L $MoSe_2$ as compared to the SiO_2/Si substrate. Interestingly,

the peak at 350 cm^{-1}, which is often used to identify monolayer $MoSe_2$, is found to completely disappear on the suspended $MoSe_2$ samples, while it clearly appears in the heterostructures region Raman spectra. In the free-standing MoS_2 regions, in addition to the most prominent peaks at 385 cm^{-1} and 403 cm^{-1}, a small peak was observed at 269 cm^{-1}, which has been earlier attributed to the formation of alloys. The frequency difference between the E and A peaks for single layer MoS_2 is 20 cm-1, which is consistent with previously reported monolayer MoS_2. Interestingly, the heterostructures regions, where 1L of the selenide grew on top of 1L of the sulfide, the frequency difference for MoS_2 peaks was found to increase. Overall, the peak features for MoS_2 were found to be stronger than those of $MoSe_2$.

5.5 Raman Spectroscopy of in-Plane Heterostructures

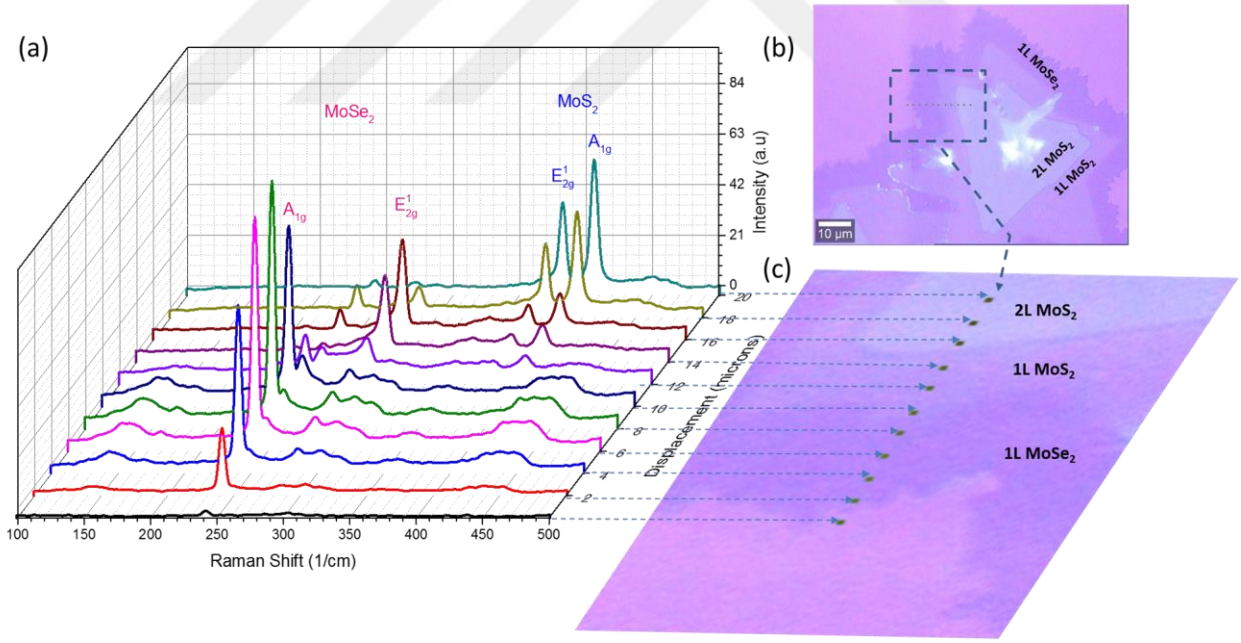

Figure 5.7: Raman characterization of $MoSe_2$-MoS_2 lateral heterostructures. (a)Waterfall Raman spectra of CVD grown $MoSe_2$- MoS_2 in plane hetero structure from the selected region shown in (b) optical

image. Separation of each scan is 2 microns and spectra is taken with 532 nm laser. (c) The enlarged region in the blue dotted frame.

The Raman spectra of in-plane (or lateral) heterostructures were also investigated in detail as well. Figure 5.7 outlines the details of this experiment. Figure 5.7 a shows a waterfall plot of Raman spectra obtained from different regions of a multilayered heterostructures, the optical image of which has been shown in Figure 5.7b. The rectangular dashed box in Figure 5.7b area has been magnified and its perspective rotated in 3D, and presented in Figure 5.7c in order to align the approximate position from which each of the spectra were obtained, as indicated by the blue dashed arrows. It can be seen that E_{2g}^{1}(285 cm-1) and 2ZA(251 cm-1) intensity peaks from $MoSe_2$ are weaker compared to the primary peak A_{1g} around 240 cm-1 in the $MoSe_2$-only region, while, at the junction of the heterostructure it is clear that the intensity of these two peaks become much stronger in the "overlap" regions. In addition, the A_{1g} peak Intesity at ~240 cm^{-1} is strongly suppressed in the overlapping areas. This is also seen in peaks at 142 and 170 cm^{-1}. The other peaks are found to appear at expected regions of the spectra, depending on the region the spectra have been obtained from.

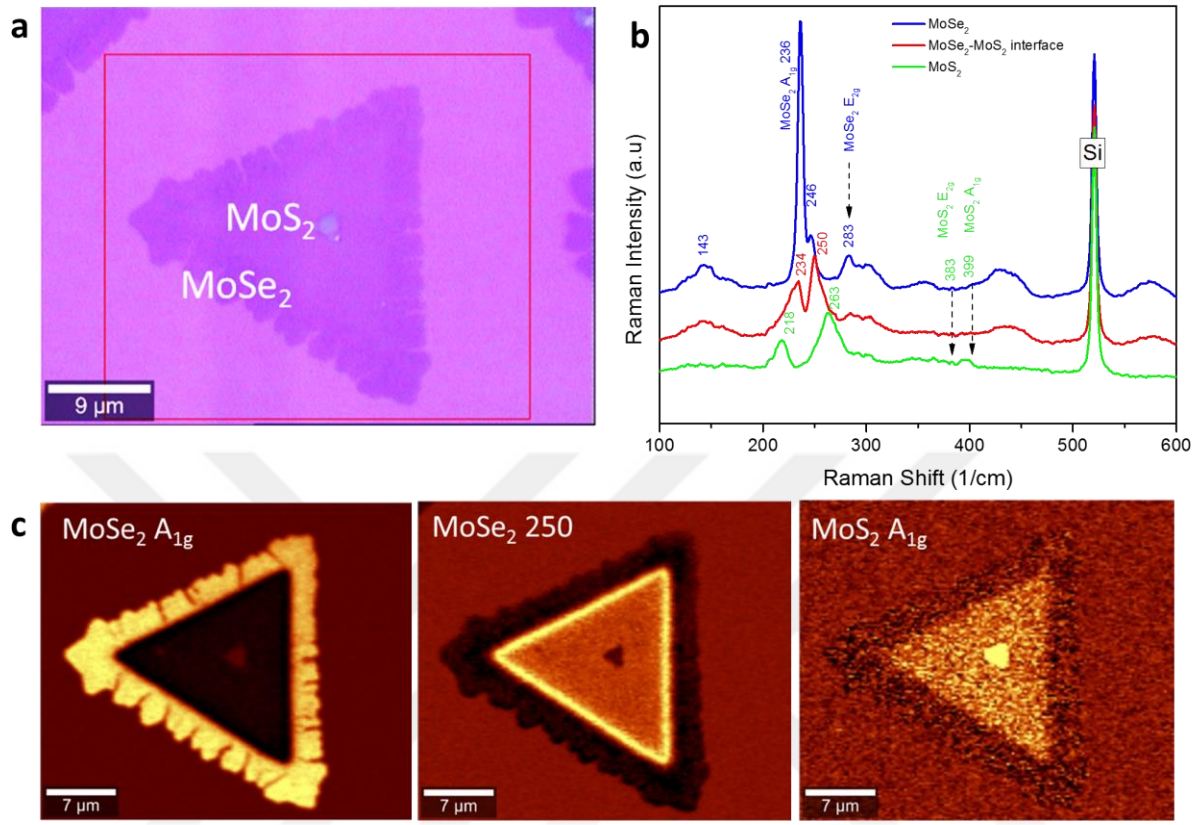

Figure 5.8: a) Optical image of in-plane MoS_2-$MoSe_2$ heterostructure. b) Single Raman spectrum taking the region of MoS_2, $MoSe_2$ and interfaces. c) Raman mapping of $MoSe_2$ peaks (A_{1g} at 236 cm^{-1} and 250 cm^{-1}) and MoS_2 A_{1g} peak at 400 cm^{-1}.

The evolution of the peak positions can be visualized in a very different manner by plotting Raman Spectral maps (for this work, the Raman excitation energy used was 2.33 eV). These maps are obtained by integrating the intensity of a specific peak from each spectrum, and then plotting a map of those integrated intensities as a function of position (The peak frequencies in region of interest are centered and integrated using wiTECH Four project software). In this way, it becomes clear which Raman peaks have a stronger presence in which region of the composite heterostructures sample. Figure 5.8a shows

the optical image of a heterostructure in which MoS_2 was first synthesized, followed by $MoSe_2$. The optical image shows a faint contrast close to the edge of the triangular-shaped crystal, suggesting that there is a separation of MoS_2-rich area and the $MoSe_2$-rich area. Figure 5.8b shows typical spectra plotted from the pure $MoSe_2$ (outer edge region, blue curve), junction area (corresponding the faint change in color in Figure 5.8a, red curve), and a region well into the heterostructures area (green curve). A striking observation in this sample is that the $MoSe_2$ A_{1g} and the 2ZA peaks, which in the bare sample appear around 236 cm-1 and 246 cm-1 respectively, appear to undergo red shift and blue shift, respectively, as the Raman probe moves further inward into the heterostructures.

Figure 5.8c shows the Raman map of the $MoSe_2$ A_{1g} peak, selected to be around 236 cm^{-1} corresponding to that seen in the blue curve of Figure 5.8b, representing pure-$MoSe_2$ region. The map shows a clear bright region in the outer edge and interface region of the triangular sample, and its intensity drops sharply in the heterostructures area, due to the large red shift of the peak, which is outside our integration bandwidth for this map. It shows very clearly that the A_{1g} peak undergoes a sharp transformation at the heterostructures area. Figure 5.8d shows the map of the integrated intensity around 250 cm^{-1}, which is found to be maximum in the interfacial region, relatively less intense in the heterocrystal area, and very weak in the outer boundary region, again due to the large shift in spectral position of the 2ZA peak at different regions of the sample. It is possible that this large shift seen in this sample is possibly due to inter-layer coupling between the two sub-crystals, as well as possible strain due to their large lattice mismatch. Figure 5.8e shows the MoS_2 A_{1g} map, which can only be seen in the innermost region, corresponding the to shape of the original MoS_2 crystal.

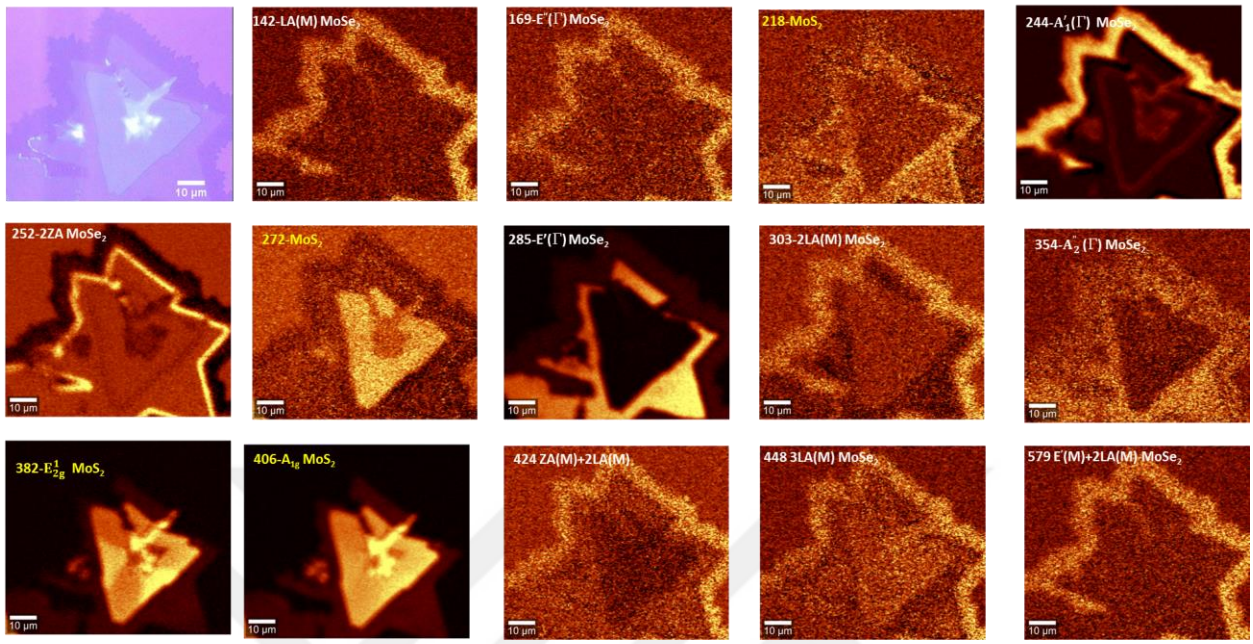

Figure 5.9: Raman mapping for CVD synthesized $MoSe_2$-MoS_2 heterostructures. Raman mapping is analyzed by using wiTECH software four project. Raman Frequencies(1/cm) are filtered and averaged to see peak intensities and positions on the flake. $MoSe_2$ Raman peaks are labeled with white color, and MoS_2 peaks are labeled yellow color.

Figure 5.9 outlines the detailed Raman maps for fourteen different spectral positions obtained from a composite heterostructure, whose optical image is shown in Figure 5.9a. The LA and multiphonon modes of MoSe2(labeled white color) can only be seen pure regions, and not observed in alloy and overlap regions. The quite interesting result is that the double resonance 2ZA peaks becomes more intense at the interface between monolayer MoS_2-$MoSe_2$. The A_{1g} of $MoSe_2$ at 244 cm^{-1} also is completely suppressed at alloy and overlap regions. The new peak at 272 cm^{-1} only appears on layer of MoS_2 region due to selenization. The 285 cm^{-1} can be seen both weakly on pure $MoSe_2$ and strong on some part of the monolayer MoS_2. This also proves that MoS_2 layer is slightly alloyed with selenide. The

characteristic E_{2g} and A_{1g} Raman modes of MoS_2 (labeled yellow color) are strongly observed around 382 cm^{-1} and 406 cm^{-1}.

5.6 Photoluminescence of MoS_2-$MoSe_2$ Heterostructures

Figure 5.10 outlines the photoluminescence of $MoSe_2$. PL is significantly quenched in heterobilayer MoS_2-$MoSe_2$ structure due to charge transfer , similar quenching of photoluminescence was observed on previous experiment by stacking mechanically exfoliated monolayer samples[213]. The PL peak of MoS_2 in the heterostructure is decreased than the individual MoS_2 by about 40 %.

In summary, we have developed a two-step CVD method to synthesize of MoS_2-$MoSe_2$ heterostructure. Moreover, we present a uniform Raman mapping as a tool to closely investigate the nature of heterostructure systems and compare their behavior within the "same" hetero-structure. Our work reveals a number of important observations in the nature of evolution of the Raman peaks in these systems and their junctions.

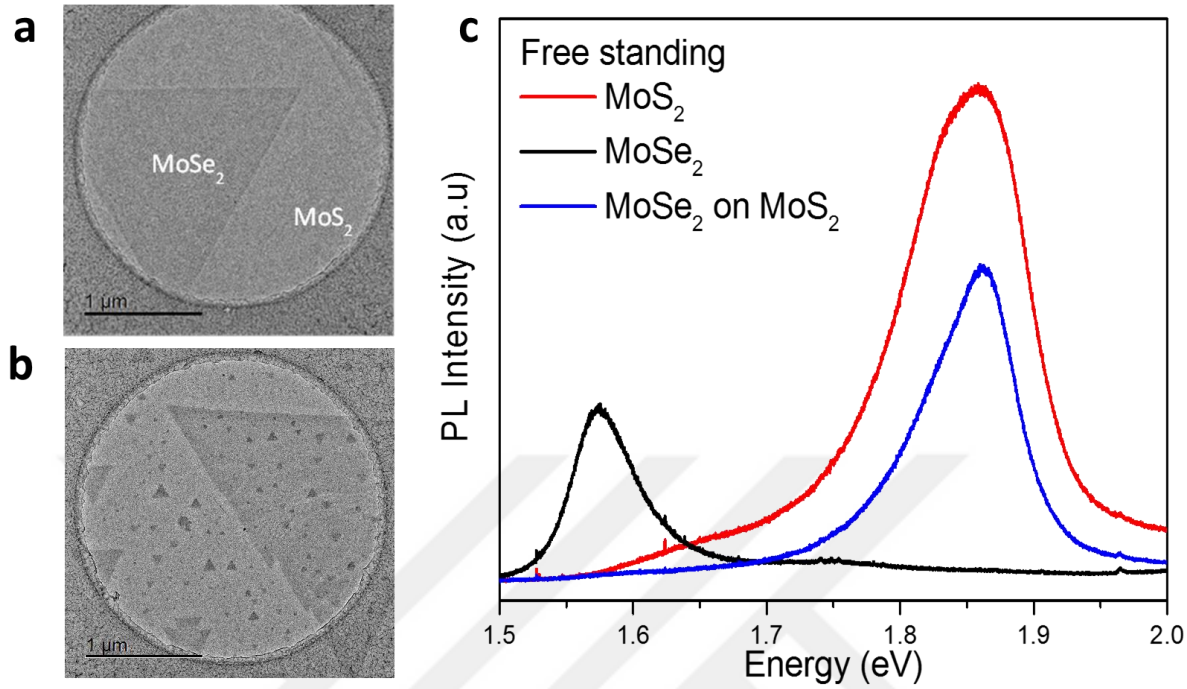

Figure 5.10: TEM images of typical suspended MoS_2-$MoSe_2$ heterostructure (a) and mono and bi layer $MoSe_2$ on samples on TEM grids. Photoluminescence spectra of suspended individual layers and stacked MoS_2 -$MoSe_2$ layer.

Chapter 6: Conclusion and Discussion

High quality, large-area single and few layered TMDS are grown on a variety of substrates by VPC method based on MoO_2 and WO_2 precursor. Because of their high quality, Raman spectroscopy on these samples reveal a range of multiphonon processes. We particularly investigate the layer thickness and substrate dependence of newly observed peak at 285 and 487 cm^{-1} for MoS_2 samples. We further investigate the origin a peak near 250 cm^{-1} for $MoSe_2$ and its heterostrucuture samples. We find that this peak arises from a possible double resonant Raman process involving the Z acoustic phonon along the M-K high symmetry line in the Brillouin zone and can be a signature of the monolayer. In addition, we studied Raman spectra of 1-4L $MoSe_2$ with four different excitation energy. We demonstrate that the peak intensity ratio of the A' and E' peaks (at ~240 cm^{-1} and ~285 cm^{-1}, respectively) are strongly enhanced and coupled with the C exciton in monolayer $MoSe_2$ at 2.54 eV.

The ultrahigh, optoelectronic -grade crystalline quality of these samples further established through photocurrent spectroscopy. For the first time, excitonic states of MoS_2 are clearly observed at room temperature. We more accurately calculate the band gap (between valance band maximum and conduction band minimum), large exciton binding energies, and spin orbit coupling energies using photocurrent spectrum.

We finally synthesized atomically sharp MoS_2-$MoSe_2$ lateral heterostructures. By combining Raman and TEM results, we have observed new alloy peaks at 269 cm^{-1} and 370 cm^{-1}. We have also grown rotationally aligned vertical MoS_2-$MoSe_2$ van der Waals heterostructures, which shows highly efficient charge transfer from $MoSe_2$ to MoS_2.

Dissemination

Journal Publications

1. **Ismail Bilgin**, Fangze Liu, Anthony Vargas, Andrew Winchester, Michael K.L. Man, Moneesh Upmanyu, Keshav Dani, Gautam Gupta, Saikat Talapatra, Aditya D. Mohite, Swastik Kar. Chemical Vapor Deposition Synthesized Atomically Thin Molybdenum Disulfide with Optoelectronic-Grade Crystalline Quality. *ACS Nano*, **2015**, *9* (9), pp 8822–8832.

2. Pradeep Waduge, **Ismail Bilgin**, Joseph Larkin, Robert Y Henley, Kenneth Goodfellow, Adam C Graham, David C Bell, Nick Vamivakas, Swastik Kar, Meni Wanunu. Direct and Scalable Deposition of Atomically Thin Low-Noise MoS_2 Membranes on Apertures. ACS Nano, 2015, 9 (7), pp 7352–7359.

3. Yung-Chen Lin, **Ismail Bilgin**, Towfiq Ahmed, Renjie Chen, Doug Pete, Swastik Kar, Aditya Mohite, Jianxin Zhu, and Jinkyoung Yoo. Charge Transfer in Crystalline Germanium/ Monolayer MoS_2 Heterostructures Prepared by Chemical Vapor Deposition. Nanoscale, 2016,8, 18675-18681

4. Kyung Jin Seo, Yi Qiang, **Ismail Bilgin**, Swastik Kar, Claudio Vinegoni, Ralph Weissleder, and Hui Fang. Transparent Electrophysiology Microelectrodes and Interconnects from Metal Nanomesh. (just accepted ACS Nano)

5. Anthony Vargas, Fangze Liu, Christopher Lane, Daniel Rubin, **Ismail Bilgin**, Zachariah Hennighausen, Matthew DeCapua, Arun Bansil, and Swastik Kar. Tunable and Laser-reconfigurable 2D heterocrystals obtained by epitaxial stacking of Bi_2Se_3 and MoS_2 atomic layers. (Under review in Science Advances)

6. Morgann Berg, Kunttal Keyshar, **Ismail Bilgin**, Fangze Liu, Hisato Yamaguchi, Robert Vajtai, Calvin Chan, Gautam Gupta, Swastik Kar, Pulickel Ajayan, Taisuke Ohta, Aditya D. Mohite. Layer-dependence of the electronic band alignment of few-layer MoS_2 on SiO_2 measured using photoemission electron microscopy. (ready to be submitted)

7. **Ismail Bilgin,** Aldo S. Raeliarijaona, Sebastian Cooper Hodge, Aditya Mohite, Andres de Luna Bugallo, Humberto Terrones, Swastik Kar. Investigations of Raman processes in high-quality vapor-phase-deposition grown atomically-thin molybdenum diselenide. (ready to be submitted)

PATENT

1. Pradeep Waduge, **Ismail Bilgin**, Joseph Larkin, Swastik Kar, Meni Wanunu. Low Noise Ultrathin Freestanding Membranes Composed of Atomically-Thin 2D Materials. WO 2016/133570 A1.

REFERENCES

1 Peierls, R. E. Quelques proprietes typiques des corpses solides. *Ann. I. H. Poincare* 5, **177-222**, (1935).

2 Landau, L. Zur Theorie der phasenumwandlungen II. *Phys. Z. Sowjetunion* 11, **26-35**, (1937).

3 Wallace, P. R. The Band Theory of Graphite. *Phys. Rev.* 71, **622-634**, (1947).

4 Novoselov, K. S., Geim, A. K., Morozov, S. V., Jiang, D., Zhang, Y., Dubonos, S. V., Grigorieva, I. V. & Firsov, A. A. Electric field effect in atomically thin carbon films. *Science* 306, **666-669**, (2004).

5 Novoselov, K., Jiang, D., Schedin, F., Booth, T., Khotkevich, V., Morozov, S. & Geim, A. Two-dimensional atomic crystals. *Proc. Natl. Acad. Sci. U.S.A.* 102, **10451-10453**, (2005).

6 Zhang, Y., Tan, Y.-W., Stormer, H. L. & Kim, P. Experimental observation of the quantum Hall effect and Berry's phase in graphene. *Nature* 438, **201-204**, (2005).

7 Novoselov, K. S., Geim, A. K., Morozov, S., Jiang, D., Katsnelson, M., Grigorieva, I., Dubonos, S. & Firsov, A. Two-dimensional gas of massless Dirac fermions in graphene. *Nature* 438, **197-200**, (2005).

8 Nair, R. R., Blake, P., Grigorenko, A. N., Novoselov, K. S., Booth, T. J., Stauber, T., Peres, N. M. & Geim, A. K. Fine structure constant defines visual transparency of graphene. *Science* 320, **1308-1308**, (2008).

9 Geim, A. K. & Grigorieva, I. V. Van der Waals heterostructures. *Nature* 499, **419-425**, (2013).

10 Dean, C. R. *et al.* Boron nitride substrates for high-quality graphene electronics. *Nature nanotechnology* 5, **722-726**, (2010).

11 Lee, K. H., Shin, H.-J., Lee, J., Lee, I.-y., Kim, G.-H., Choi, J.-Y. & Kim, S.-W. Large-scale synthesis of high-quality hexagonal boron nitride nanosheets for large-area graphene electronics. *Nano letters* 12, **714-718**, (2012).

12 Kim, K. K., Hsu, A., Jia, X., Kim, S. M., Shi, Y., Dresselhaus, M., Palacios, T. & Kong, J. Synthesis and characterization of hexagonal boron nitride film as a dielectric layer for graphene devices. *ACS nano* 6, **8583-8590**, (2012).

13 Radisavljevic, B., Radenovic, A., Brivio, J., Giacometti, V. & Kis, A. Single-layer MoS_2 transistors. *Nat. Nanotechnol.* 6, **147-150**, (2011).

14 Fuhrer, M. S. & Hone, J. Measurement of mobility in dual-gated MoS_2 transistors. *Nat. Nanotechnol.* 8, **146-147**, (2013).

15 Liu, B., Fathi, M., Chen, L., Abbas, A., Ma, Y. & Zhou, C. Chemical vapor deposition growth of monolayer WSe2 with tunable device characteristics and growth mechanism study. *ACS nano* 9, **6119-6127**, (2015).

16 Fang, H., Chuang, S., Chang, T. C., Takei, K., Takahashi, T. & Javey, A. High-performance single layered WSe2 p-FETs with chemically doped contacts. *Nano Lett.* 12, **3788-3792**, (2012).

17 Osada, M. & Sasaki, T. Two‐Dimensional Dielectric Nanosheets: Novel Nanoelectronics From Nanocrystal Building Blocks. *Adv. Mater.* 24, **210-228**, (2012).

18 Osada, M. & Sasaki, T. Exfoliated oxide nanosheets: new solution to nanoelectronics. *J. Mater. Chem.* 19, **2503-2511**, (2009).

19 Ma, R. & Sasaki, T. Two-Dimensional Oxide and Hydroxide Nanosheets: Controllable High-Quality Exfoliation, Molecular Assembly, and Exploration of Functionality. *Acc. Chem. Res.* 48, **136-143**, (2015).

20 Mak, K. F. & Shan, J. Photonics and optoelectronics of 2D semiconductor transition metal dichalcogenides. *Nat. Photon* 10, **216-226**, (2016).

21 Ling, X., Wang, H., Huang, S., Xia, F. & Dresselhaus, M. S. The renaissance of black phosphorus. *Proceedings of the National Academy of Sciences* 112, **4523-4530**, (2015).

22 Mak, K. F., He, K. L., Lee, C., Lee, G. H., Hone, J., Heinz, T. F. & Shan, J. Tightly bound trions in monolayer MoS_2. *Nature Materials* 12, **207-211**, (2013).

23 Ye, Z. L., Cao, T., O'Brien, K., Zhu, H. Y., Yin, X. B., Wang, Y., Louie, S. G. & Zhang, X. Probing excitonic dark states in single-layer tungsten disulphide. *Nature* 513, **214-218**, (2014).

24 Lin, Y., Ling, X., Yu, L., Huang, S., Hsu, A. L., Lee, Y.-H., Kong, J., Dresselhaus, M. S. & Palacios, T. Dielectric Screening of Excitons and Trions in Single-Layer MoS2. *Nano Lett.* 14, **5569-5576**, (2014).

25 He, K., Kumar, N., Zhao, L., Wang, Z., Mak, K. F., Zhao, H. & Shan, J. Tightly Bound Excitons in Monolayer WSe_2. *Phys. Rev. Lett.* 113, **026803**, (2014).

26 Jones, A. M. *et al.* Optical generation of excitonic valley coherence in monolayer WSe2. *Nat Nano* 8, **634-638**, (2013).

27 Xia, F., Wang, H., Xiao, D., Dubey, M. & Ramasubramaniam, A. Two-dimensional material nanophotonics. *Nat Photon* 8, **899-907**, (2014).

28 Kappera, R., Voiry, D., Yalcin, S. E., Branch, B., Gupta, G., Mohite, A. D. & Chhowalla, M. Phase-engineered low-resistance contacts for ultrathin MoS2 transistors. *Nat. Mater.* 13, **1128-1134**, (2014).

29 Cheng, Y., Nie, A., Zhang, Q., Gan, L.-Y., Shahbazian-Yassar, R. & Schwingenschlogl, U. Origin of the phase transition in lithiated molybdenum disulfide. *ACS nano* 8, **11447-11453**, (2014).

30 Py, M. & Haering, R. Structural destabilization induced by lithium intercalation in MoS2 and related compounds. *Can. J. Phys.* 61, **76-84**, (1983).

31 Wang, X., Shen, X., Wang, Z., Yu, R. & Chen, L. Atomic-scale clarification of structural transition of MoS2 upon sodium intercalation. *ACS nano* 8, **11394-11400**, (2014).

32 Gao, P., Wang, L., Zhang, Y., Huang, Y. & Liu, K. Atomic-scale probing of the dynamics of sodium transport and intercalation-induced phase transformations in MoS2. *ACS nano* 9, **11296-11301**, (2015).

33 Lin, Y.-C., Dumcenco, D. O., Huang, Y.-S. & Suenaga, K. Atomic mechanism of the semiconducting-to-metallic phase transition in single-layered MoS2. *Nat. Nanotechnol.* 9, **391-396**, (2014).

34 Zeng, H. & Cui, X. An optical spectroscopic study on two-dimensional group-VI transition metal dichalcogenides. *Chem. Soc. Rev.* 44, **2629-2642**, (2015).

35 Splendiani, A., Sun, L., Zhang, Y., Li, T., Kim, J., Chim, C.-Y., Galli, G. & Wang, F. Emerging photoluminescence in monolayer MoS_2. *Nano Lett.* 10, **1271-1275**, (2010).

36 Kuc, A., Zibouche, N. & Heine, T. Influence of quantum confinement on the electronic structure of the transition metal sulfide TS_2. *Phys. Rev. B* 83, **245213**, (2011).

37 Zhang, Y. *et al.* Direct observation of the transition from indirect to direct bandgap in atomically thin epitaxial $MoSe_2$. *Nat. Nanotechnol.* 9, **111-115**, (2014).

38 Terrones, H., López-Urías, F. & Terrones, M. Novel hetero-layered materials with tunable direct band gaps by sandwiching different metal disulfides and diselenides. *Sci. Rep.* 3, **1549**, (2013).

39 Eda, G., Yamaguchi, H., Voiry, D., Fujita, T., Chen, M. & Chhowalla, M. Photoluminescence from chemically exfoliated MoS2. *Nano letters* 11, **5111-5116**, (2011).

40 Mak, K. F., Lee, C., Hone, J., Shan, J. & Heinz, T. F. Atomically thin MoS 2: a new direct-gap semiconductor. *Phys. Rev. Lett.* 105, **136805**, (2010).

41 Klots, A. R. *et al.* Probing excitonic states in suspended two-dimensional semiconductors by photocurrent spectroscopy. *Scientific Reports* 4, **6608**, (2014).

42 Dhakal, K. P., Duong, D. L., Lee, J., Nam, H., Kim, M., Kan, M., Lee, Y. H. & Kim, J. Confocal absorption spectral imaging of MoS 2: optical transitions depending on the atomic thickness of intrinsic and chemically doped MoS 2. *Nanoscale* 6, **13028-13035**, (2014).

43 Rivera, P., Seyler, K. L., Yu, H., Schaibley, J. R., Yan, J., Mandrus, D. G., Yao, W. & Xu, X. Valley-polarized exciton dynamics in a 2D semiconductor heterostructure. *Science* 351, **688-691**, (2016).

44 Zeng, H. L., Dai, J. F., Yao, W., Xiao, D. & Cui, X. D. Valley polarization in MoS_2 monolayers by optical pumping. *Nature Nanotechnology* 7, **490-493**, (2012).

45 Mak, K. F., He, K., Shan, J. & Heinz, T. F. Control of valley polarization in monolayer MoS_2 by optical helicity. *Nat. Nanotechnol.* 7, **494-498**, (2012).

46 Ye, Y. *et al.* Electrical generation and control of the valley carriers in a monolayer transition metal dichalcogenide. *Nat Nano* 11, **598-602**, (2016).

47 Qin, S., Lei, W., Liu, D. & Chen, Y. In-situ and tunable nitrogen-doping of MoS2 nanosheets. *Sci. Rep.* 4, (2014).

48 Buscema, M., Steele, G. A., van der Zant, H. S. & Castellanos-Gomez, A. The effect of the substrate on the Raman and photoluminescence emission of single-layer MoS_2. *Nano Res.* 7, **561-571**, (2014).

49 Castellanos-Gomez, A., Roldán, R., Cappelluti, E., Buscema, M., Guinea, F., van der Zant, H. S. & Steele, G. A. Local strain engineering in atomically thin MoS2. *Nano Lett.* 13, **5361-5366**, (2013).

50 Schaibley, J. R., Yu, H., Clark, G., Rivera, P., Ross, J. S., Seyler, K. L., Yao, W. & Xu, X. Valleytronics in 2D materials. *Nature Reviews Materials* 1, **16055**, (2016).

51 Liu, G.-B., Xiao, D., Yao, Y., Xu, X. & Yao, W. Electronic structures and theoretical modelling of two-dimensional group-VIB transition metal dichalcogenides. *Chem. Soc. Rev.* 44, **2643-2663**, (2015).

52 Wang, H. *et al.* Integrated circuits based on bilayer MoS2 transistors. *Nano Lett.* 12, **4674-4680**, (2012).

53 Bertolazzi, S., Brivio, J. & Kis, A. Stretching and breaking of ultrathin MoS2. *ACS nano* 5, **9703-9709**, (2011).

54 Cheng, R., Jiang, S., Chen, Y., Liu, Y., Weiss, N., Cheng, H.-C., Wu, H., Huang, Y. & Duan, X. Few-layer molybdenum disulfide transistors and circuits for high-speed flexible electronics. *Nat. Commun.* 5, (2014).

55 Bernardi, M., Palummo, M. & Grossman, J. C. Extraordinary Sunlight Absorption and One Nanometer Thick Photovoltaics Using Two-Dimensional Monolayer Materials. *Nano Lett.* 13, **3664-3670**, (2013).

56 Shanmugam, M., Durcan, C. A. & Yu, B. Layered semiconductor molybdenum disulfide nanomembrane based Schottky-barrier solar cells. *Nanoscale* 4, **7399-7405**, (2012).

57 Britnell, L. *et al.* Strong light-matter interactions in heterostructures of atomically thin films. *Science* 340, **1311-1314**, (2013).

58 Sarkar, D., Liu, W., Xie, X., Anselmo, A. C., Mitragotri, S. & Banerjee, K. MoS2 field-effect transistor for next-generation label-free biosensors. *ACS nano* 8, **3992-4003**, (2014).

59 Liu, T. *et al.* Iron Oxide Decorated MoS2 Nanosheets with Double PEGylation for Chelator-Free Radiolabeling and Multimodal Imaging Guided Photothermal Therapy. *ACS Nano* 9, **950-960**, (2015).

60 Loo, A. H., Bonanni, A., Ambrosi, A. & Pumera, M. Molybdenum disulfide (MoS 2) nanoflakes as inherently electroactive labels for DNA hybridization detection. *Nanoscale* 6, **11971-11975**, (2014).

61 Liu, T., Wang, C., Gu, X., Gong, H., Cheng, L., Shi, X., Feng, L., Sun, B. & Liu, Z. Drug Delivery with PEGylated MoS2 Nano‐sheets for Combined Photothermal and Chemotherapy of Cancer. *Adv. Mater.* 26, **3433-3440**, (2014).

62 Robinson, J. A. Growing Vertical in the Flatland. *ACS Nano* 10, **42-45**, (2016).

63 Lotsch, B. V. Vertical 2D heterostructures. *Annual Review of Materials Research* 45, **85-109**, (2015).

64 Wang, H., Liu, F., Fu, W., Fang, Z., Zhou, W. & Liu, Z. Two-dimensional heterostructures: fabrication, characterization, and application. *Nanoscale* 6, **12250-12272**, (2014).

65 Lee, C.-H. *et al.* Atomically thin p–n junctions with van der Waals heterointerfaces. *Nat Nano* 9, **676-681**, (2014).

66 Gong, Y. *et al.* Vertical and in-plane heterostructures from WS2/MoS2 monolayers. *Nat Mater* 13, **1135-1142**, (2014).

67 Liu, X., Balla, I., Bergeron, H., Campbell, G. P., Bedzyk, M. J. & Hersam, M. C. Rotationally Commensurate Growth of MoS2 on Epitaxial Graphene. *ACS Nano* 10, **1067-1075**, (2016).

68 Yang, W. *et al.* Epitaxial growth of single-domain graphene on hexagonal boron nitride. *Nat Mater* 12, **792-797**, (2013).

69 Ruzmetov, D. *et al.* Vertical 2D/3D Semiconductor Heterostructures Based on Epitaxial Molybdenum Disulfide and Gallium Nitride. *ACS Nano* 10, **3580-3588**, (2016).

70 Shi, Y. *et al.* van der Waals Epitaxy of MoS2 Layers Using Graphene As Growth Templates. *Nano Lett.* 12, **2784-2791**, (2012).

71 Tan, H., Fan, Y., Zhou, Y., Chen, Q., Xu, W. & Warner, J. H. Ultrathin 2D Photodetectors Utilizing Chemical Vapor Deposition Grown WS2 With Graphene Electrodes. *ACS nano* 10, **7866-7873**, (2016).

72 Yoon, J. *et al.* Highly flexible and transparent multilayer MoS2 transistors with graphene electrodes. *Small* 9, **3295-3300**, (2013).

73 Shi, S.-F. & Wang, F. Two-dimensional materials: Atomically thin pn junctions. *Nature nanotechnology* 9, **664-665**, (2014).

74 Lee, C.-H. *et al.* Atomically thin p–n junctions with van der Waals heterointerfaces. *Nature nanotechnology* 9, **676-681**, (2014).

75 Li, M.-Y. *et al.* Epitaxial growth of a monolayer WSe_2-MoS_2 lateral pn junction with an atomically sharp interface. *Science* 349, **524-528**, (2015).

76 Zhan, Y. J., Liu, Z., Najmaei, S., Ajayan, P. M. & Lou, J. Large-Area Vapor-Phase Growth and Characterization of MoS_2 Atomic Layers on a SiO_2 Substrate. *Small* 8, **966-971**, (2012).

77 Lee, Y. H. *et al.* Synthesis of Large-Area MoS_2 Atomic Layers with Chemical Vapor Deposition. *Adv. Mater.* 24, **2320-2325**, (2012).

78 van der Zande, A. M. *et al.* Grains and grain boundaries in highly crystalline monolayer molybdenum disulphide. *Nat. Mat.* 12, **554-561**, (2013).

79 Najmaei, S. *et al.* Vapour phase growth and grain boundary structure of molybdenum disulphide atomic layers. *Nat. Mat.* 12, **754-759**, (2013).

80 Lin, Y. C., Zhang, W. J., Huang, J. K., Liu, K. K., Lee, Y. H., Liang, C. T., Chu, C. W. & Li, L. J. Wafer-scale MoS_2 thin layers prepared by MoO_3 sulfurization. *Nanoscale* 4, **6637-6641**, (2012).

81 Li, X. L. & Li, Y. D. Formation of MoS_2 inorganic fullerenes (IFs) by the reaction of MoO_3 nanobelts and S. *Chem. Eur. J.* 9, **2726-2731**, (2003).

82 Wang, X. S., Feng, H. B., Wu, Y. M. & Jiao, L. Y. Controlled Synthesis of Highly Crystalline MoS_2 Flakes by Chemical Vapor Deposition. *J. Am. Chem. Soc.* 135, **5304-5307**, (2013).

83 Lince, J. R., Hilton, M. R. & Bommannavar, A. S. Oxygen substitution in sputter-deposited MoS_2 films studied by extended X-ray absorption fine structure, X-ray photoelectron spectroscopy and X-ray diffraction. *Surf. Coat. Technol.* 43, **640-651**, (1990).

84 Chow, W. L., Luo, X., Quek, S. Q. & Tay, B. K. Evolution of Raman Scattering and Electronic Structure of Ultrathin Molybdenum Disulfide by Oxygen Chemisorption *Adv. Electron. Mater.* 1, **1400037**, (2015).

85 Hao, Y. *et al.* The Role of Surface Oxygen in the Growth of Large Single-Crystal Graphene on Copper. *Science* 342, **720-723**, (2013).

86 Ionescu, R. *et al.* Oxygen etching of thick MoS_2 films. *Chem. Commun.* 50, **11226-11229**, (2014).

87 Park, W., Park, J., Jang, J., Lee, H., Jeong, H., Cho, K., Hong, S. & Lee, T. Oxygen environmental and passivation effects on molybdenum disulfide field effect transistors. *Nanotechnology* 24, **095202**, (2013).

88 Qiu, H., Pan, L., Yao, Z., Li, J., Shi, Y. & Wang, X. Electrical characterization of back-gated bi-layer MoS_2 field-effect transistors and the effect of ambient on their performances. *Appl. Phys. Lett.* 100, **123104**, (2012).

89 https://hubpages.com/education/OCR-Biology-Cells-Exchange-and-Transport.

90 Hudson, S., Tanner, D., Redington, W., Magner, E., Hodnett, K. & Nakahara, S. Quantitative TEM analysis of a hexagonal mesoporous silicate structure. *PCCP* 8, **3467-3474**, (2006).

91 https://commons.wikimedia.org/wiki/File:Raman_energy_levels.svg.

92 Scheuschner, N., Gillen, R., Staiger, M. & Maultzsch, J. Interlayer resonant Raman modes in few-layer MoS_2. *Phys. Rev. B* 91, **235409**, (2015).

93 Tauc, J. Optical properties and electronic structure of amorphous Ge and Si. *Mater. Res. Bull.* 3, **37-46**, (1968).

94 Anthony Vargas, F. L., Christopher Lane, Daniel Rubin, Ismail Bilgin, Zachariah Hennighausen, Matthew DeCapua, Arun Bansil, Swastik Kar. Tunable and Laser-reconfigurable 2D heterocrystals obtained by epitaxial stacking of crystallographically incommensurate Bi_2Se_3 and MoS_2 atomic layers. *Under Review*, (2017).

95 Gupta, P., Dongare, P. D., Grover, S., Dubey, S., Mamgain, H., Bhattacharya, A. & Deshmukh, M. M. A facile process for soak-and-peel delamination of CVD graphene from substrates using water. *Sci. Rep.* 4, (2014).

96 Miro, P., Audiffred, M. & Heine, T. An Atlas of Two-Dimensional Materials. *Chem. Soc. Rev.* 43, **6537-6554**, (2014).

97 Splendiani, A., Sun, L., Zhang, Y. B., Li, T. S., Kim, J., Chim, C. Y., Galli, G. & Wang, F. Emerging Photoluminescence in Monolayer MoS_2. *Nano Lett.* 10, **1271-1275**, (2010).

98 Lee, C., Yan, H., Brus, L. E., Heinz, T. F., Hone, J. & Ryu, S. Anomalous Lattice Vibrations of Single- and Few-Layer MoS_2. *ACS Nano* 4, **2695-2700**, (2010).

99 Mak, K. F., He, K. L., Shan, J. & Heinz, T. F. Control of valley polarization in monolayer MoS_2 by optical helicity. *Nat. Nanotechnol.* 7, **494-498**, (2012).

100 Britnell, L. *et al.* Strong Light-Matter Interactions in Heterostructures of Atomically Thin Films. *Science* 340, **1311-1314**, (2013).

101 Lopez-Sanchez, O., Lembke, D., Kayci, M., Radenovic, A. & Kis, A. Ultrasensitive photodetectors based on monolayer MoS_2. *Nat. Nanotechnol.* 8, **497-501**, (2013).

102 Xiang, Q. J., Yu, J. G. & Jaroniec, M. Synergetic Effect of MoS_2 and Graphene as Cocatalysts for Enhanced Photocatalytic H_2 Production Activity of TiO_2 Nanoparticles. *J. Am. Chem. Soc.* 134, **6575-6578**, (2012).

103 Chang, H. Y., Yang, S. X., Lee, J. H., Tao, L., Hwang, W. S., Jena, D., Lu, N. S. & Akinwande, D. High-Performance, Highly Bendable MoS_2 Transistors with High-K Dielectrics for Flexible Low-Power Systems. *ACS Nano* 7, **5446-5452**, (2013).

104 Das, S., Gulotty, R., Sumant, A. V. & Roelofs, A. All Two-Dimensional, Flexible, Transparent, and Thinnest Thin Film Transistor. *Nano Lett.* 14, **2861-2866**, (2014).

105 Novoselov, K. S., Jiang, D., Schedin, F., Booth, T. J., Khotkevich, V. V., Morozov, S. V. & Geim, A. K. Two-dimensional atomic crystals. *Proc. Natl. Acad. Sci. USA* 102, **10451-10453**, (2005).

106 Baugher, B. W. H., Churchill, H. O. H., Yang, Y. F. & Jarillo-Herrero, P. Optoelectronic devices based on electrically tunable p-n diodes in a monolayer dichalcogenide. *Nat. Nanotechnol.* 9, **262-267**, (2014).

107 Ross, J. S. *et al.* Electrically tunable excitonic light-emitting diodes based on monolayer WSe_2 p-n junctions. *Nat. Nanotechnol.* 9, **268-272**, (2014).

108 Pospischil, A., Furchi, M. M. & Mueller, T. Solar-energy conversion and light emission in an atomic monolayer p-n diode. *Nat. Nanotechnol.* 9, **257-261**, (2014).

109 Yin, Z. Y. *et al.* Single-Layer MoS_2 Phototransistors. *ACS Nano* 6, **74-80**, (2012).

110 Mak, K. F., Lee, C., Hone, J., Shan, J. & Heinz, T. F. Atomically Thin MoS_2: A New Direct-Gap Semiconductor. *Phys. Rev. Lett.* 105, (2010).

111 Nair, R. R., Blake, P., Grigorenko, A. N., Novoselov, K. S., Booth, T. J., Stauber, T., Peres, N. M. R. & Geim, A. K. Fine structure constant defines visual transparency of graphene. *Science* 320, **1308-1308**, (2008).

112 George, P. A., Strait, J., Dawlaty, J., Shivaraman, S., Chandrashekhar, M., Rana, F. & Spencer, M. G. Ultrafast optical-pump terahertz-probe spectroscopy of the carrier relaxation and recombination dynamics in epitaxial graphene. *Nano Lett.* 8, **4248-4251**, (2008).

113 Wu, C.-C., Jariwala, D., Sangwan, V. K., Marks, T. J., Hersam, M. C. & Lauhon, L. J. Elucidating the photoresponse of ultrathin MoS_2 field-effect transistors by scanning photocurrent microscopy. *J. Phys. Chem. Lett.* 4, **2508-2513**, (2013).

114 Golasa, K., Grzeszczyk, M., Leszczynski, P., Faugeras, C., Nicolet, A. A. L., Wysmolek, A., Potemski, M. & Babinski, A. Multiphonon resonant Raman scattering in MoS_2. *Appl. Phys. Lett.* 104, (2014).

115 Li, H., Zhang, Q., Yap, C. C. R., Tay, B. K., Edwin, T. H. T., Olivier, A. & Baillargeat, D. From Bulk to Monolayer MoS_2: Evolution of Raman Scattering. *Adv. Funct. Mater.* 22, **1385-1390**, (2012).

116 Chakraborty, B., Matte, H. S. S. R., Sood, A. K. & Rao, C. N. R. Layer-dependent resonant Raman scattering of a few layer MoS_2. *J. Raman Spectrosc.* 44, **92-96**, (2013).

117 Utama, M. I. B., Lu, X., Yuan, Y. & Xiong, Q. Detrimental influence of catalyst seeding on the device properties of CVD-grown 2D layered materials: A case study on $MoSe_2$. *Appl. Phys. Lett.* 105, **253102**, (2014).

118 Waduge, P. *et al.* Direct and Scalable Deposition of Atomically Thin Low-Noise MoS_2 Membranes on Apertures. *ACS Nano*, **10.1021/acsnano.1025b02369**, (2015).

119 Clauss, F. J. *Solid lubricants and self-lubricating solids*. (Elsevier, 2012).

120 Liu, K. *et al.* Evolution of interlayer coupling in twisted molybdenum disulfide bilayers. *Nat. Commun.* 5, **4966**, (2014).

121 Hao, Y. *et al.* The role of surface oxygen in the growth of large single-crystal graphene on copper. *Science* 342, **720-723**, (2013).

122 Wang, Y., Cong, C., Qiu, C. & Yu, T. Raman spectroscopy study of lattice vibration and crystallographic orientation of monolayer MoS_2 under uniaxial strain. *Small* 9, **2857-2861**, (2013).

123 Liu, K. K. *et al.* Growth of Large-Area and Highly Crystalline MoS_2 Thin Layers on Insulating Substrates. *Nano Lett.* 12, **1538-1544**, (2012).

124 Livneh, T. S., Jonathen E. A Comprehensive Spectral Analysis of Multiphonon Resenont Raman Scattering in 2H-MoS_2. *ArXiv:1408.6748*, (2014).

125 Luo, X., Zhao, Y., Zhang, J., Toh, M., Kloc, C., Xiong, Q. & Quek, S. Y. Effects of lower symmetry and dimensionality on Raman spectra in two-dimensional WSe_2. *Phys. Rev. B* 88, **195313**, (2013).

126 Li, H. *et al.* Fabrication of Single- and Multilayer MoS_2 Film-Based Field-Effect Transistors for Sensing NO at Room Temperature. *Small* 8, **63-67**, (2012).

127 Schmidt, H. *et al.* Transport properties of monolayer MoS_2 grown by chemical vapor deposition. *Nano Lett.* 14, **1909-1913**, (2014).

128 Dumcenco, D. *et al.* Large-Area Epitaxial Monolayer MoS_2. *ACS nano* 9, **4611-4620**, (2015).

129 Furchi, M. M., Polyushkin, D. K., Pospischil, A. & Mueller, T. Mechanisms of Photoconductivity in Atomically Thin MoS_2. *Nano Lett.* 14, **6165-6170**, (2014).

130 Lembke, D. & Kis, A. Breakdown of High-Performance Monolayer MoS_2 Transistors. *ACS Nano* 6, **10070-10075**, (2012).

131 Mertens, J., Shi, Y. M., Molina-Sanchez, A., Wirtz, L., Yang, H. Y. & Baumberg, J. J. Excitons in a mirror: Formation of "optical bilayers" using MoS_2 monolayers on gold substrates. *Appl. Phys. Lett.* 104, **191105**, (2014).

132 Zhu, Z. Y., Cheng, Y. C. & Schwingenschlogl, U. Giant spin-orbit-induced spin splitting in two-dimensional transition-metal dichalcogenide semiconductors. *Phys. Rev. B* 84, **153402**, (2011).

133 Mak, K. F., Lee, C., Hone, J., Shan, J. & Heinz, T. F. Atomically Thin MoS_2: A New Direct-Gap Semiconductor. *Phys. Rev. Lett.* 105, **136805**, (2010).

134 Eda, G., Yamaguchi, H., Voiry, D., Fujita, T., Chen, M. W. & Chhowalla, M. Photoluminescence from Chemically Exfoliated MoS_2. *Nano Lett.* 12, **526-526**, (2012).

135 Huang, Y. L. *et al.* Bandgap tunability at single-layer molybdenum disulphide grain boundaries. *Nat. Commun.* 6, **6298**, (2015).

136 Miró, P., Audiffred, M. & Heine, T. An atlas of two-dimensional materials. *Chem. Soc. Rev.* 43, **6537-6554**, (2014).

137 Kim, J. *et al.* Observation of tunable band gap and anisotropic Dirac semimetal state in black phosphorus. *Science* 349, **723-726**, (2015).

138 Pöllmann, C. *et al.* Resonant internal quantum transitions and femtosecond radiative decay of excitons in monolayer WSe_2. *Nat. Mater.* 14, **889-893**, (2015).

139 Costanzo, D., Jo, S., Berger, H. & Morpurgo, A. F. Gate-induced superconductivity in atomically thin MoS_2 crystals. *Nat. Nanotechnol.* 11, **339-344**, (2016).

140 Yan, J., Zhang, Y., Kim, P. & Pinczuk, A. Electric field effect tuning of electron-phonon coupling in graphene. *Phys. Rev. Lett.* 98, **166802**, (2007).

141 Chen, J. *et al.* Optical nano-imaging of gate-tunable graphene plasmons. *Nature* 487, **77-81**, (2012).

142 Emani, N. K., Chung, T.-F., Ni, X., Kildishev, A. V., Chen, Y. P. & Boltasseva, A. Electrically tunable damping of plasmonic resonances with graphene. *Nano Lett.* 12, **5202-5206**, (2012).

143 Lee, J., Mak, K. F. & Shan, J. Electrical control of the valley Hall effect in bilayer MoS_2 transistors. *Nat. Nanotechnol.* 11, **421–425**, (2016).

144 Wu, S. *et al.* Electrical tuning of valley magnetic moment through symmetry control in bilayer MoS_2. *Nature Phys.* 9, **149-153**, (2013).

145 Berkelbach, T. C., Hybertsen, M. S. & Reichman, D. R. Theory of neutral and charged excitons in monolayer transition metal dichalcogenides. *Phys. Rev. B* 88, **045318**, (2013).

146 Shang, J., Shen, X., Cong, C., Peimyoo, N., Cao, B., Eginligil, M. & Yu, T. Observation of excitonic fine structure in a 2D transition-metal dichalcogenide semiconductor. *ACS Nano* 9, **647-655**, (2015).

147 Qian, X., Liu, J., Fu, L. & Li, J. Quantum spin Hall effect in two-dimensional transition metal dichalcogenides. *Science* 346, **1344-1347**, (2014).

148 Mak, K. F., McGill, K. L., Park, J. & McEuen, P. L. The valley Hall effect in MoS_2 transistors. *Science* 344, **1489-1492**, (2014).

149 Li, L., O'Farrell, E., Loh, K., Eda, G., Özyilmaz, B. & Neto, A. C. Controlling many-body states by the electric-field effect in a two-dimensional material. *Nature* 529, **185–189**, (2015).

150 Lee, I. *et al.* Gate‐Tunable Hole and Electron Carrier Transport in Atomically Thin Dual‐Channel WSe_2/MoS_2 Heterostructure for Ambipolar Field‐Effect Transistors. *Adv. Mater.* 28, **9519-9525**, (2016).

151 Mas-Balleste, R., Gomez-Navarro, C., Gomez-Herrero, J. & Zamora, F. 2D materials: to graphene and beyond. *Nanoscale* 3, **20-30**, (2011).

152 Venkata Subbaiah, Y., Saji, K. & Tiwari, A. Atomically thin MoS_2: A versatile nongraphene 2D material. *Adv. Funct. Mater.* 26, **2046-2069**, (2016).

153 Schwierz, F. Graphene transistors. *Nat. Nanotechnol.* 5, **487-496**, (2010).

154 Liu, M., Yin, X., Ulin-Avila, E., Geng, B., Zentgraf, T., Ju, L., Wang, F. & Zhang, X. A graphene-based broadband optical modulator. *Nature* 474, **64-67**, (2011).

155 Sarkar, D., Xie, X., Liu, W., Cao, W., Kang, J., Gong, Y., Kraemer, S., Ajayan, P. M. & Banerjee, K. A subthermionic tunnel field-effect transistor with an atomically thin channel. *Nature* 526, **91-95**, (2015).

156 Yu, W. J., Liu, Y., Zhou, H., Yin, A., Li, Z., Huang, Y. & Duan, X. Highly efficient gate-tunable photocurrent generation in vertical heterostructures of layered materials. *Nat. Nanotechnol.* 8, **952-958**, (2013).

157 Choi, M. S., Lee, G.-H., Yu, Y.-J., Lee, D.-Y., Lee, S. H., Kim, P., Hone, J. & Yoo, W. J. Controlled charge trapping by molybdenum disulphide and graphene in ultrathin heterostructured memory devices. *Nat. Commun.* 4, **1624**, (2013).

158 Bonaccorso, F., Colombo, L., Yu, G., Stoller, M., Tozzini, V., Ferrari, A. C., Ruoff, R. S. & Pellegrini, V. Graphene, related two-dimensional crystals, and hybrid systems for energy conversion and storage. *Science* 347, **1246501**, (2015).

159 Hong, J. *et al.* Exploring atomic defects in molybdenum disulphide monolayers. *Nat. Commun.* 6, **6293**, (2015).

160 Van Der Zande, A. M. *et al.* Grains and grain boundaries in highly crystalline monolayer molybdenum disulphide. *Nat. Mater.* 12, **554-561**, (2013).

161 Lin, Y. C., Dumcenco, D. O., Komsa, H. P., Niimi, Y., Krasheninnikov, A. V., Huang, Y. S. & Suenaga, K. Properties of Individual Dopant Atoms in Single‐Layer MoS_2: Atomic Structure, Migration, and Enhanced Reactivity. *Adv. Mater.* 26, **2857-2861**, (2014).

162 Vancsó, P., Magda, G. Z., Pető, J., Noh, J.-Y., Kim, Y.-S., Hwang, C., Biró, L. P. & Tapasztó, L. The intrinsic defect structure of exfoliated MoS_2 single layers revealed by Scanning Tunneling Microscopy. *Sci. Rep.* 6, **29726** (2016).

163 Qiu, H. *et al.* Hopping transport through defect-induced localized states in molybdenum disulphide. *Nat. Commun.* 4, **2642**, (2013).

164 McDonnell, S., Addou, R., Buie, C., Wallace, R. M. & Hinkle, C. L. Defect-dominated doping and contact resistance in MoS_2. *ACS Nano* 8, **2880-2888**, (2014).

165 Ma, N. & Jena, D. Charge scattering and mobility in atomically thin semiconductors. *Phys. Rev. X* 4, **011043**, (2014).

166 O'Brien, M., McEvoy, N., Hanlon, D., Hallam, T., Coleman, J. N. & Duesberg, G. S. Mapping of low-frequency Raman modes in CVD-grown transition metal dichalcogenides: layer number, stacking orientation and resonant effects. *Sci. Rep.* 6, **19476** (2016).

167 Rice, C., Young, R., Zan, R., Bangert, U., Wolverson, D., Georgiou, T., Jalil, R. & Novoselov, K. Raman-scattering measurements and first-principles calculations of strain-induced phonon shifts in monolayer MoS_2. *Phys. Rev. B* 87, **081307**, (2013).

168 Ferrari, A. C. & Basko, D. M. Raman spectroscopy as a versatile tool for studying the properties of graphene. *Nat. Nanotechnol.* 8, **235-246**, (2013).

169 Gouadec, G. & Colomban, P. Raman spectroscopy of nanomaterials: how spectra relate to disorder, particle size and mechanical properties. *Prog. Cryst. Growth Charact. Mater.* 53, **1-56**, (2007).

170 Lin, Z., Carvalho, B. R., Kahn, E., Lv, R., Rao, R., Terrones, H., Pimenta, M. A. & Terrones, M. Defect engineering of two-dimensional transition metal dichalcogenides. *2D Mater.* 3, **022002**, (2016).

171 Lee, C., Yan, H., Brus, L. E., Heinz, T. F., Hone, J. & Ryu, S. Anomalous lattice vibrations of single- and few-layer MoS_2. *ACS nano* 4, **2695-2700**, (2010).

172 Nam, D., Lee, J.-U. & Cheong, H. Excitation energy dependent Raman spectrum of $MoSe_2$. *Sci. Rep.* 5, **17113** (2015).

173 Soubelet, P., Bruchhausen, A., Fainstein, A., Nogajewski, K. & Faugeras, C. Resonance effects in the Raman scattering of monolayer and few-layer $MoSe_2$. *Phys. Rev. B* 93, **155407**, (2016).

174 Chen, S.-Y., Zheng, C., Fuhrer, M. S. & Yan, J. Helicity-resolved Raman scattering of MoS_2, $MoSe_2$, WS_2, and WSe_2 atomic layers. *Nano Lett.* 15, **2526-2532**, (2015).

175 Kioseoglou, G., Hanbicki, A. T., Currie, M., Friedman, A. L. & Jonker, B. T. Optical polarization and intervalley scattering in single layers of MoS_2 and $MoSe_2$. *Sci. Rep.* 6, **25041** (2016).

176 O'Brien, M., McEvoy, N., Hanlon, D., Lee, K., Gatensby, R., Coleman, J. N. & Duesberg, G. S. Low wavenumber Raman spectroscopy of highly crystalline $MoSe_2$ grown by chemical vapor deposition. *Phys. Status Solidi (b)* 252, **2385-2389**, (2015).

177 Lu, X. *et al.* Rapid and Nondestructive Identification of Polytypism and Stacking Sequences in Few‐Layer Molybdenum Diselenide by Raman Spectroscopy. *Adv. Mater.* 27, **4502-4508**, (2015).

178 Xia, J. *et al.* CVD synthesis of large-area, highly crystalline $MoSe_2$ atomic layers on diverse substrates and application to photodetectors. *Nanoscale* 6, **8949-8955**, (2014).

179 Su, S.-H. *et al.* Controllable synthesis of band-gap-tunable and monolayer transition-metal dichalcogenide alloys. *Front. Energy Res.* 2, **27**, (2014).

180 Wang, X. *et al.* Chemical vapor deposition growth of crystalline monolayer $MoSe_2$. *ACS Nano* 8, **5125-5131**, (2014).

181 Shaw, J. C., Zhou, H., Chen, Y., Weiss, N. O., Liu, Y., Huang, Y. & Duan, X. Chemical vapor deposition growth of monolayer $MoSe_2$ nanosheets. *Nano Res.* 7, **511-517**, (2014).

182 Suryawanshi, S. R., Pawbake, A. S., Pawar, M. S., Jadkar, S. R., More, M. A. & Late, D. J. Enhanced field emission behavior of layered $MoSe_2$. *Mater. Res. Express* 3, **035003**, (2016).

183 Duan, X. *et al.* Lateral epitaxial growth of two-dimensional layered semiconductor heterojunctions. *Nat. Nanotechnol.* 9, **1024-1030**, (2014).

184 Bilgin, I. *et al.* Chemical vapor deposition synthesized atomically thin molybdenum disulfide with optoelectronic-grade crystalline quality. *ACS Nano* 9, **8822-8832**, (2015).

185 Chen, J. *et al.* Chemical Vapor Deposition of Large‐Sized Hexagonal WSe_2 Crystals on Dielectric Substrates. *Adv. Mater.* 27, **6722-6727**, (2015).

186 Tongay, S., Zhou, J., Ataca, C., Lo, K., Matthews, T. S., Li, J., Grossman, J. C. & Wu, J. Thermally driven crossover from indirect toward direct bandgap in 2D semiconductors: $MoSe_2$ versus MoS_2. *Nano Lett.* 12, **5576-5580**, (2012).

187 Ugeda, M. M. *et al.* Giant bandgap renormalization and excitonic effects in a monolayer transition metal dichalcogenide semiconductor. *Nat. Mater.* 13, **1091-1095**, (2014).

188 Wang, Y., Zhang, S., Huang, D., Cheng, J., Li, Y. & Wu, S. Screening effect of graphite and bilayer graphene on excitons in $MoSe_2$ monolayer. *2D Mater.* 4, **015021**, (2016).

189 Zhang, C., Chen, Y., Johnson, A., Li, M.-Y., Li, L.-J., Mende, P. C., Feenstra, R. M. & Shih, C.-K. Probing Critical Point Energies of Transition Metal Dichalcogenides: Surprising Indirect Gap of Single Layer WSe_2. *Nano Lett.* 15, **6494-6500**, (2015).

190 Kozawa, D. *et al.* Photocarrier relaxation pathway in two-dimensional semiconducting transition metal dichalcogenides. *Nat. Commun.* 5, **4543**, (2014).

191 Li, Y. *et al.* Measurement of the optical dielectric function of monolayer transition-metal dichalcogenides: MoS_2, $MoSe_2$, WS_2, and WSe_2. *Phys. Rev. B* 90, **205422**, (2014).

192 Tonndorf, P. *et al.* Photoluminescence emission and Raman response of monolayer MoS_2, $MoSe_2$, and WSe_2. *Opt. Express* 21, **4908-4916**, (2013).

193 Baroni, S., de Gironcoli, S., Dal Corso, A. & Giannozzi, P. Phonons and related crystal properties from density-functional perturbation theory. *Rev. Mod. Phys.* 73, **515-562**, (2001).

194 Hohenberg, P. & Kohn, W. Inhomogeneous Electron Gas. *Phys. Rev.* 136, **B864-B871**, (1964).

195 Giannozzi, P. *et al.* QUANTUM ESPRESSO: a modular and open-source software project for quantum simulations of materials. *J. Phys.: Condens. Matter* 21, **395502**, (2009).

196 Kohn, W. & Sham, L. J. Self-Consistent Equations Including Exchange and Correlation Effects. *Phys. Rev.* 140, **A1133-A1138**, (1965).

197 Troullier, N. & Martins, J. L. Efficient pseudopotentials for plane-wave calculations. *Phys. Rev. B* 43, **1993-2006**, (1991).

198 Monkhorst, H. J. & Pack, J. D. Special points for Brillouin-zone integrations. *Phys. Rev. B* 13, **5188-5192**, (1976).

199 Duesberg, G. S. Heterojunctions in 2D semiconductors: A perfect match. *Nat Mater* 13, **1075-1076**, (2014).

200 Wilson, N. R. *et al.* Determination of band offsets, hybridization, and exciton binding in 2D semiconductor heterostructures. *Science Advances* 3, (2017).

201 Kim, K. S., Walter, A. L., Moreschini, L., Seyller, T., Horn, K., Rotenberg, E. & Bostwick, A. Coexisting massive and massless Dirac fermions in symmetry-broken bilayer graphene. *Nat Mater* 12, **887-892**, (2013).

202 Bistritzer, R. & MacDonald, A. H. Moiré bands in twisted double-layer graphene. *Proceedings of the National Academy of Sciences* 108, **12233-12237**, (2011).

203 Yan, W. *et al.* Strain and curvature induced evolution of electronic band structures in twisted graphene bilayer. *Nat. Commun.* 4, **2159**, (2013).

204 Li, G., Luican, A., Lopes dos Santos, J. M. B., Castro Neto, A. H., Reina, A., Kong, J. & Andrei, E. Y. Observation of Van Hove singularities in twisted graphene layers. *Nat Phys* 6, **109-113**, (2010).

205 Hunt, B. *et al.* Massive Dirac fermions and Hofstadter butterfly in a van der Waals heterostructure. *Science* 340, **1427-1430**, (2013).

206 Ponomarenko, L. A. *et al.* Cloning of Dirac fermions in graphene superlattices. *Nature* 497, **594-597**, (2013).

207 Dean, C. R. *et al.* Hofstadter/'s butterfly and the fractal quantum Hall effect in moire superlattices. *Nature* 497, **598-602**, (2013).

208 Cui, X. *et al.* Multi-terminal transport measurements of MoS2 using a van der Waals heterostructure device platform. *Nat Nano* 10, **534-540**, (2015).

209 Kitaura, R., Miyata, Y., Xiang, R., Hone, J., Kong, J., Ruoff, R. S. & Maruyama, S. Chemical vapor deposition growth of graphene and related materials. *J. Phys. Soc. Jpn.* 84, **121013**, (2015).

210 Tang, S. *et al.* Precisely aligned graphene grown on hexagonal boron nitride by catalyst free chemical vapor deposition. *Sci. Rep.* 3, **2666**, (2013).

211 Miwa, J. A., Dendzik, M., Grønborg, S. S., Bianchi, M., Lauritsen, J. V., Hofmann, P. & Ulstrup, S. Van der Waals Epitaxy of Two-Dimensional MoS2–Graphene Heterostructures in Ultrahigh Vacuum. *ACS Nano* 9, **6502-6510**, (2015).

212 Morpurgo, A. F. Ten years of Nature Physics: The ABC of 2D materials. *Nat Phys* 11, **625-626**, (2015).

213 Ceballos, F., Bellus, M. Z., Chiu, H.-Y. & Zhao, H. Ultrafast Charge Separation and Indirect Exciton Formation in a MoS2–MoSe2 van der Waals Heterostructure. *ACS Nano* 8, **12717-12724**, (2014).